

University of Mississippi

eGrove

Electronic Theses and Dissertations

Graduate School

12-1993

Development of stereoscopic particle tracking velocimetry for turbulent flow field diagnostics

Veera P. Rajendran

Follow this and additional works at: <https://egrove.olemiss.edu/etd>



Part of the [Engineering Commons](#)

Recommended Citation

Rajendran, Veera P., "Development of stereoscopic particle tracking velocimetry for turbulent flow field diagnostics" (1993). *Electronic Theses and Dissertations*. 2184.

<https://egrove.olemiss.edu/etd/2184>

This Thesis is brought to you for free and open access by the Graduate School at eGrove. It has been accepted for inclusion in Electronic Theses and Dissertations by an authorized administrator of eGrove. For more information, please contact egrove@olemiss.edu.

DEVELOPMENT OF STEREOSCOPIC PARTICLE TRACKING VELOCIMETRY
FOR TURBULENT FLOW FIELD DIAGNOSTICS

BY

VEERA P. RAJENDRAN

B.E., Bharathiar University, INDIA, 1987

A Thesis
Submitted to the Faculty of
The University of Mississippi
in Partial Fulfillment of the Requirements
for the Degree of Master of Science
in the Department of Mechanical Engineering

The University of Mississippi

December, 1993

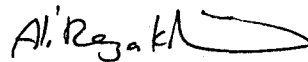
DEVELOPMENT OF STEREOSCOPIC PARTICLE TRACKING VELOCIMETRY
FOR TURBULENT FLOW FIELD DIAGNOSTICS

BY

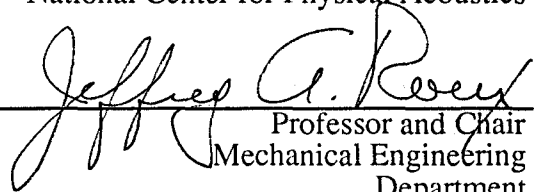
VEERA P. RAJENDRAN



Assistant Professor
Mechanical Engineering
Department



Research Assistant Professor
of Engineering and
Research Scientist
National Center for Physical Acoustics



Professor and Chair
Mechanical Engineering
Department



Dean
Graduate School

LD
3211.82
R155
1993

ABSTRACT

DEVELOPMENT OF STEREOSCOPIC PARTICLE TRACKING VELOCIMETRY FOR TURBULENT FLOW FIELD DIAGNOSTICS

RAJENDRAN, P. VEERA. B.E., Bharathiar University, INDIA, 1987. M.S., University of Mississippi, 1993. Thesis directed by Dr. Sumon K. Sinha and Dr. Ali R. Kolaini.

Stereoscopic particle tracking velocimetry (SPTV) was used to analyze a turbulent submerged jet of Reynolds number (based on the diameter of the nozzle) 8000. SPTV involves tracking the motion of tracer particles over time in a flow in three dimensions. The first part of this work consisted of developing a stereoscopic particle tracking technique using two high-speed video cameras. This included calibration of the cameras with "known" points, and developing an algorithm to automatically match and track particles. The second part was to apply the same to a submerged water jet in order to measure velocities. The velocities were subsequently used to calculate the components of the Reynolds stress tensor, vorticities and other useful turbulent parameters in all three directions at two locations along the axis of the jet.

The cameras were calibrated using a set of "known" grid points which were imaged by both cameras. Data reduction equations, that relate the world coordinates (X, Y, Z positions in space) of the object (grid) points to their image coordinates in left and right cameras, were solved to obtain a set of "modified" camera parameters. The uncertainties in determining the X, Y and Z positions of the grid points, after correcting for the bias errors due to refraction and lens distortion, were found to be 6.81×10^{-5} mm,

5.84×10^{-5} mm and 1.73×10^{-4} mm respectively in a $19\text{mm} \times 27\text{mm} \times 19\text{mm}$ measurement volume.

Calibration and measurements were performed at two downstream locations along the axis of the jet. The corresponding measurement volumes were centered at ten and twenty nozzle diameters from the nozzle exit ($x/d \cong 10$ and 20). Polystyrene particles of $250 \mu\text{m}$ size were used to visualize the flow. A matching and tracking algorithm was developed to automatically find corresponding particles in the two views, and to track them into the next time step. Image coordinates of the particles in the stereo views were used to calculate the world coordinates of the particle. Velocities were calculated knowing the particle displacements and the elapsed time. Particle data for 100 time steps (total duration of 50 ms at $x/d \cong 10$; and 100 ms at $x/d \cong 20$) were pooled. The mean and fluctuating components of velocities were found and all components of the Reynolds stress tensor ($\overline{u'^2}$, $\overline{v'^2}$, $\overline{w'^2}$, $\overline{u'v'}$, $\overline{v'w'}$, $\overline{w'u'}$) were calculated. The vorticity field in the vertical (X-Y) plane of the jet was calculated. Integral scales were also calculated across the jet. Turbulent microscales in longitudinal and lateral directions were estimated based on the velocity fluctuations and their gradients. The mean velocity profile at $x/d=22$ was found to be in good agreement with the Görtler type analytical solution for the submerged round jet. A possible mechanism by which bubbles injected into the turbulent flow field undergo deformation, which may result in oscillations, was suggested. The main causes of errors in the measurement and in the particle data analysis were discussed. Possible remedies were suggested.

ACKNOWLEDGMENTS

The author wishes to gratefully thank Dr. Sumon Kumar Sinha and Dr. Ali Reza Kolaini for their constant support, skillful guidance and enormous patience throughout the research work especially at times of crises which were many. Dr. Kolaini has been instrumental in initiating and managing the project.

The research work was funded by the Office of Naval Research and was carried out at the facilities of the National Center for Physical Acoustics.

The author wishes to thank the National Center for Physical Acoustics for providing a research assistantship.

The author also thanks Dr. Jeffrey A. Roux and the Department of Mechanical Engineering for providing a graduate assistantship and the Graduate School for providing a graduate fellowship.

Thanks to Mr. Paul Dakin for doing excellent machining job and offering helpful suggestions during the setting up of the experiment.

Thanks to my friends and colleagues in National Center for Physical Acoustics who have offered their cooperation many times during the research.

Above all, I wish to thank my mother, father, and brothers for their emotional support and constant encouragement throughout my graduate study.

TABLE OF CONTENTS

	Page
Abstract.....	iii
Acknowledgments.....	v
Table of Contents	vi
List of Tables	ix
List of Figures	x
Chapter	
1. INTRODUCTION AND OBJECTIVES	1
1.1. Introduction	1
1.2 Survey of 3-D Measurement of Fluid Flows	3
1.3 The Problem and Challenges	4
1.4 Objectives	5
2. EXPERIMENTAL FACILITY AND TECHNIQUES.....	6
2.1 Experimental Facility	6
2.2 Camera Calibration and Data Reduction Equations	12
2.2.1 Check for Camera Parameters	18
2.3 Image Processing	19
3. AUTOMATIC MATCHING AND TRACKING OF PARTICLES	23
3.1 Introduction	23
3.2 Motivation for This Work	23

3.3	Basic Approach	24
3.4	Formulation of the Problem	29
3.4.1	Basic Criteria	29
3.4.2	Additional Conditions	35
3.4.3	Testing of the Algorithm	39
4.	OVERVIEW OF TURBULENCE IN A SUBMERGED JET	42
4.1	Introduction.....	42
4.2	Submerged Jet	42
4.2.1	Turbulence in Submerged Jet Flow	45
5.	CALIBRATION.....	47
6.	RESULTS AND DISCUSSIONS	52
6.1	Introduction	52
6.2	Velocities and Turbulent Parameters	52
6.2.1	Mean Velocities	53
6.2.2	Fluctuating Velocity Components	57
6.2.3	Reynolds Stresses.....	63
6.3	Vorticity	64
6.4	Estimation of Turbulent Scales	82
7.	CONCLUSIONS AND RECOMMENDATIONS	90
7.1	Introduction.....	90
7.2	Measurement Errors.....	90
7.2.1	Errors in Finding Depth Positions.....	91
7.2.2	Errors in Matching and Tracking of Particles.....	92
7.2.3	Errors in Finding the Centroids of Particle Images.....	92

7.3	Conclusions	93
7.4	Recommendations	95
LIST OF ABBREVIATIONS		97
REFERENCES.....		99
APPENDIX A: Derivation of Data Reduction Equations		103
BIOGRAPHICAL SKETCH OF THE AUTHOR.....		111

LIST OF TABLES

Table		page
5.1	Reference Grid Points Used for Calibration	47
5.2	Initial Guess and Converged ("Modified") Camera Parameters for Camera A.....	48
5.3	Initial Guess and Converged ("Modified") Camera Parameters for Camera B	49
5.4	RMS Errors in Calibration	50
6.1	Mean Spacing Between Vortex centers Measured From the Contour Plots.....	83
6.2	Turbulent Microscales.....	83
6.3	Kolmogorov Microscales.....	84

LIST OF FIGURES

Figures	Page
2.1 Experimental Facility.....	8
2.2 Schematic of the Experimental Facility.....	9
2.3 Turbulent Jet Created for the Study.....	11
2.4 Coordinate System Used for Stereo-Viewing.....	15
2.5 Collinearity Condition in Central Projection.....	16
2.6 Ratios of Similar Triangles as a Measure of Magnification.....	16
2.7 Salient Steps in Image Processing.....	21
2.8 Salient Steps in Data Processing.....	22
3.1 Single Camera View.....	25
3.2 Two Camera Stereo View.....	25
3.3 Vertical Height Comparison Between the Object and its Image.....	26
3.4a Particle Movement in X-Axis as Seen by the Camera.....	26
3.4b Particle Movement in Y-Axis as Seen by the Camera.....	27
3.4c Particle Movement in Z-Axis as Seen by the Camera.....	28
3.5 Typical Image of Particles in the Jet.....	30
3.6 Matching of Particles Between Image A and Image B in Time Step 1.....	32
3.7 Tracking Particles from One Time Step to the Next.....	32
3.8 Multiple Correspondences in Matching and Tracking.....	36
3.9 Comparison of Particle Movement in Stereo View.....	37

3.10	One-to-one Correspondence in Particles	37
4.1	Sketch of a Turbulent Jet	43
6.1	Coordinate System and the Jet	54
6.2	Control Volume for Velocity Vector Averaging	54
6.3	Plot of Mean Velocities at $x/d=12$	58
6.4	Plot of Mean Velocities at $x/d=22$	59
6.5	Plot of Fluctuating Velocities at $x/d=12$	60
6.6	Plot of Velocity Data Distribution Across the Jet at $x/d=12$	61
6.7	Plot of Fluctuating Velocities at $x/d=22$	62
6.8	Plot of Turbulent Shear Stresses at $x/d=12$	65
6.9	Plot of Turbulent Shear Stresses at $x/d=22$	66
6.10	3-D Plot of Axial Velocity at $x/d=22$	67
6.11	3-D Plot of Tangential Fluctuating Velocity at $x/d=22$	68
6.12	3-D Plot of Shear Stress in the X-Y Plane at $x/d=22$	69
6.13	Contour Plot of Vorticities in X-Direction at $x/d\cong 10$	72
6.14	Contour Plot of Vorticities in Y-Direction at $x/d\cong 10$	73
6.15	Contour Plot of Vorticities in Z-Direction at $x/d\cong 10$	74
6.16a	Contour Plot of Vorticities in Z-Direction in Levels $-750s^{-1}$, $-500s^{-1}$, $-250s^{-1}$, $0s^{-1}$ at $x/d\cong 10$	75
6.16b	Contour Plot of Vorticities in Z-Direction in Levels $250s^{-1}$, $500s^{-1}$, $750s^{-1}$, $1000s^{-1}$ at $x/d\cong 10$	76
6.17	Contour Plot of Vorticities in X-Direction at $x/d\cong 20$	77
6.18	Contour Plot of Vorticities in Y-Direction at $x/d\cong 20$	78
6.19	Contour Plot of Vorticities in Z-Direction at $x/d\cong 20$	79

6.20a	Contour Plot of Vorticities in Z-Direction in Levels -750s^{-1} , -500s^{-1} , -250s^{-1} , 0s^{-1} at $x/d \cong 20$	80
6.20b	Contour Plot of Vorticities in Z-Direction in Levels 250s^{-1} , 500s^{-1} , 750s^{-1} , 1000s^{-1} at $x/d \cong 20$	81
6.21	Plot of 'Average Eddy Scale' Across the Jet	87
6.22	Instantaneous Velocity Vector Plot for the Duration of 50 ms at $x/d \cong 10$	88
6.23	Instantaneous Velocity Vector Plot for the Duration of 100 ms at $x/d \cong 20$	89

Chapter 1

INTRODUCTION AND OBJECTIVES

1.1 INTRODUCTION

In turbulent flow, measurements of various flow parameters are of fundamental importance. These parameters are needed in order to understand the flow, to know the mechanisms that are involved, and eventually to control or manipulate them so as to achieve the desired end results.

Optical techniques are often used to study velocity, temperature, and density fields. Velocity measurements are done using single-point measuring techniques such as laser Doppler velocimetry (LDV) and two-spot laser velocimetry. These methods preclude measurement of rapidly fluctuating flow structures as a function of time. Therefore multi-point measurement of the flow becomes necessary. Such information is much needed to understand the physics of turbulence. This need has been further accentuated by the growing realization that instantaneous values of fluctuating quantities are often entirely different from the time and space averaged values.

To fulfill the primary objective of studying instantaneous, unaveraged flow structures, several multi-point imaging techniques have been employed in recent times. Recent advancements in image acquisition and processing technology have provided sufficient means to permit quantitative fluid flow measurements by imaging techniques. These multi-point techniques being inherently non-intrusive, have an added

advantage over intrusive single-point probes (e.g. hot-wire sensors), in that, they can be successfully employed in multi-phase flow environments.

One such technique is particle tracking velocimetry (PTV). It is accomplished by observing and photographically recording the motion of tracer particles within the flow. If a tracer particle can be identified in successive time steps, then the velocities can be estimated from the displacements. This kind of photographic viewing of the flow field typically yields the two-dimensional velocity field. Since 'depth' perception is not available with a single view, three-dimensional measurements are not possible. Measurements of the positions of the tracer particles in space requires at least two views of the test volume, taken from two different angles. Similar techniques are routinely applied in photogrammetric aerial surveys of geological features of landscapes.

Most common photogrammetric methods are based on either stereoscopic (views separated by an arbitrary angle) or orthogonal (separated by an angle of 90°) viewing. Stereoscopic photogrammetry relies on the change in parallax between two views taken from adjacent vantage points to reconstruct the 'depth' of scene features. These can be easily understood by the fact that one does not perceive the depth of an object (more so at close range) when viewing with one eye; whereas one does perceive the depth when viewing with both eyes. The basis of reconstruction of a three-dimensional object in space from a pair of stereoscopic views is the same for human eyes and photogrammetry. Reconstruction of depth by stereoscopic viewing has found wide ranging applications in diverse fields such as medical tomography, mapping of geological features (mountains etc.) by aerial photographing and computer vision.

1.2 SURVEY OF 3-D MEASUREMENT OF FLUID FLOWS

Some of the earliest measurements using stereoscopic cinematography were reported by Praturi and Brodkey (1978), Tatterson et al. (1980) and Jacobi (1980). These works were of a qualitative nature in observing and describing the turbulent flow patterns. Sheu et al. (1982) made the technique more quantitative by performing manual tracking and digitization of particle images in stereo frames recorded on film. Some other researchers adopted orthogonal viewing (Adamczyk and Rimai, 1988; Racca and Dewey, 1988) to measure three-dimensional velocity field. Sinha (1988) suggested parallel viewing with a lateral displacement between the camera axes. A survey of these techniques was reported by Adrian (1986).

The task of identifying individual tracer particles and associating the corresponding images in the stereo pairs (matching) were usually done manually. The tediousness of the task tended to accentuate the errors due to human fatigue and has therefore proved to be a major stumbling block. As observed by Adrian (1986) in his review paper, a major problem in this approach is determining which pairs of images belong to the same marker. Following the same marker to the next and subsequent time steps (tracking) is even more difficult, especially when the flow is turbulent and seeded densely. Additionally, if the matching and tracking of the markers are done manually, the time required is prohibitively long.

Several researchers (Racca and Dewey, 1988; Adamczyk and Rimai, 1988; Nishino et al., 1989; Maas et al., 1991) have developed algorithms to automatically match the stereo image pairs of the tracer particles and track them over several time steps. Though automatic matching and tracking is inherently desirable, the methods proposed

by these researchers can at best be described as the first step. The algorithms have not been evaluated in a truly turbulent flow situation. Simulations have usually indicated less than satisfactory performance.

1.3 THE PROBLEM AND CHALLENGES

The accuracy of particle tracking velocimetry depends largely upon the quality of the image. Distinct particle positions have to be inferred from stereo pair of images to reliably match and track them through the next and subsequent time steps. Ideally, the flow should be seeded densely to enable an accurate depiction of small scale features in a turbulent flow field. However increasing the seeding density also makes the matching and tracking of particles more difficult; thus compromises have to be made. The clarity and resolution of the image determines the initial level of accuracy. Errors from this stage will propagate to the subsequent stages. Reconstruction of 3-D positions from stereo pairs introduce additional uncertainties. Finally, the velocities are found at randomly occurring particle positions. Therefore reconstruction of the velocity field requires some kind of interpolation scheme (Sinha and Kuhlman, 1992). The errors associated in the interpolation process can often be prohibitively large, especially if the data density is low. Since all the above mentioned constraints have to be satisfied simultaneously, most applications of PTV have met with limited success. A 2-D or planar version of PTV which has been reasonably successful is PIV (particle image velocimetry). Such a system is commercially available, for example, PIV Analysis System™ by TSI Inc., St. Paul. MN. Since matching of stereo views is not needed in PIV, extremely high seeding densities can be used. However, if the flow is 3-D, the depth movement will be misinterpreted as an in-plane movement. Since all turbulent

flows have 3-D fluctuations by definition (Tennekes and Lumley, 1972) there is a clear need for a reliable full-field 3-D velocity measuring technique. Any improvements in PTV are therefore a contribution towards this goal.

1.4 OBJECTIVES

The objectives of this research were to develop an automated stereoscopic particle tracking velocimetry technique (SPTV) and to apply this technique to measure velocity fluctuations and other related flow parameters in a submerged turbulent jet.

The objectives of the first part of the program were to improve the techniques for data reduction, camera calibration, and develop a method for automatic matching/tracking. The objective of the second part was to create a submerged jet and measure instantaneous velocities spatially and temporally, using the techniques developed in the first part. These were used to calculate the components of the Reynolds stress tensor components and vorticities. The ultimate objective was to estimate various turbulent scales in the flow. The motivation for this work was to provide a well-documented test flow to study the interaction of bubbles with turbulence. Hence the scales estimated were those pertinent to this interaction.

Chapter 2

EXPERIMENTAL FACILITY AND TECHNIQUES

2.1 EXPERIMENTAL FACILITY

This section describes the experimental facility used in this investigation. The photograph of the experimental facility is shown in Fig. 2.1 and a schematic drawing is shown in Fig. 2.2.

The facility consisted of two high-speed Kodak Ekta-Pro™ video cameras, a video digitizer, and a stage light as a source of illumination. Image acquisition and processing were done using a 486 based personal computer, an IBM 3084 VMXA mainframe computer and a Sun OS 390 workstation.

A Cole-Parmer MasterFlex™ positive displacement pump was used to pump water at a controlled flow rate into a plenum chamber, 33cm high, 48.5 cm long and 31cm wide. The plenum chamber contained the nozzle through which the jet was discharged. The whole set-up was housed in a tank 61cm high, 63cm wide and 3.3m long and filled with water. The large water body in the tank minimized disturbances and recirculation in the ambient still fluid into which the jet issued, thus closely approximating an ideal axisymmetric submerged jet. The plenum chamber was designed to damp out non-uniformities due to the pump pulsations. The plenum was sealed, vented off, and completely filled with water. Therefore the exact amount of water pumped into the plenum was discharged as a jet through the nozzle. The nozzles were of replaceable type whose diameters ranged from 3.183 mm to 12.383 mm. However, for the present

study, only the nozzle of 3.183 mm diameter was used. The tank walls were made of glass, and the plenum chamber and nozzles were made of Plexiglas® to facilitate photographing.

The tracer particles used in the experiment were made of polystyrene divinylbenzene (specific gravity 1.04) and were 250 μm in size; they were uniform in size to within 100 μm and were near spherical in shape. Also, under back lighting the particles were found to have good light scattering properties. The particles were supplied by Bangs Laboratories, Carmel, IN. A laboratory syringe pump (Sage Instruments, Model 341B) was used to introduce the mixture of tracer particles and water into the nozzle. The injection speeds were adjustable depending upon the jet speed so that optimal seeding of the flow with particles could be achieved. The syringe was placed on top of the plenum vertically above the nozzle. Therefore the particles were sucked into the nozzle and discharged with the jet. This particle injection arrangement was found to impart minimal disturbances to the actual flow. A solution (Kodak Photo-Flo 200) was added to the mixture of particles and water to reduce the surface tension of water. This eliminated the problem of particle coalescence and hence the formation of blobs. Particle occlusion or coalescence causes large errors in finding the particle centroid positions. These errors directly translate into errors in velocity.

All the optical components were connected and fixed rigidly on to an optical table after leveling. The Ekta-Pro motion analyzer (high-speed video cameras and the digitizer) was used to record images onto magnetic tapes. A real-time image grabber (Digital Vision Inc.) was used to grab images sequentially from the magnetic tapes into a PC 486 personal computer for further processing. The two high-speed video cameras were synchronized using a stroboscope. This ensured that they photographed the objects

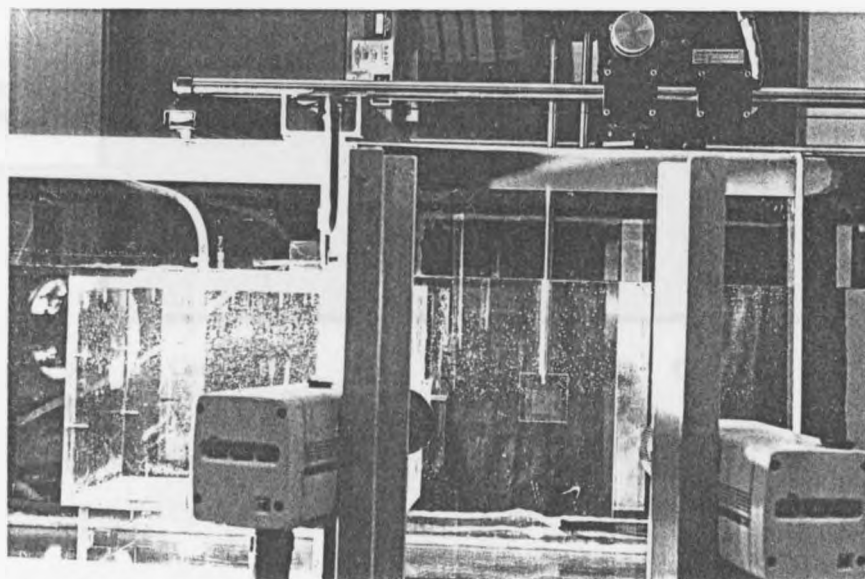


Fig. 2.1. Experimental facility.

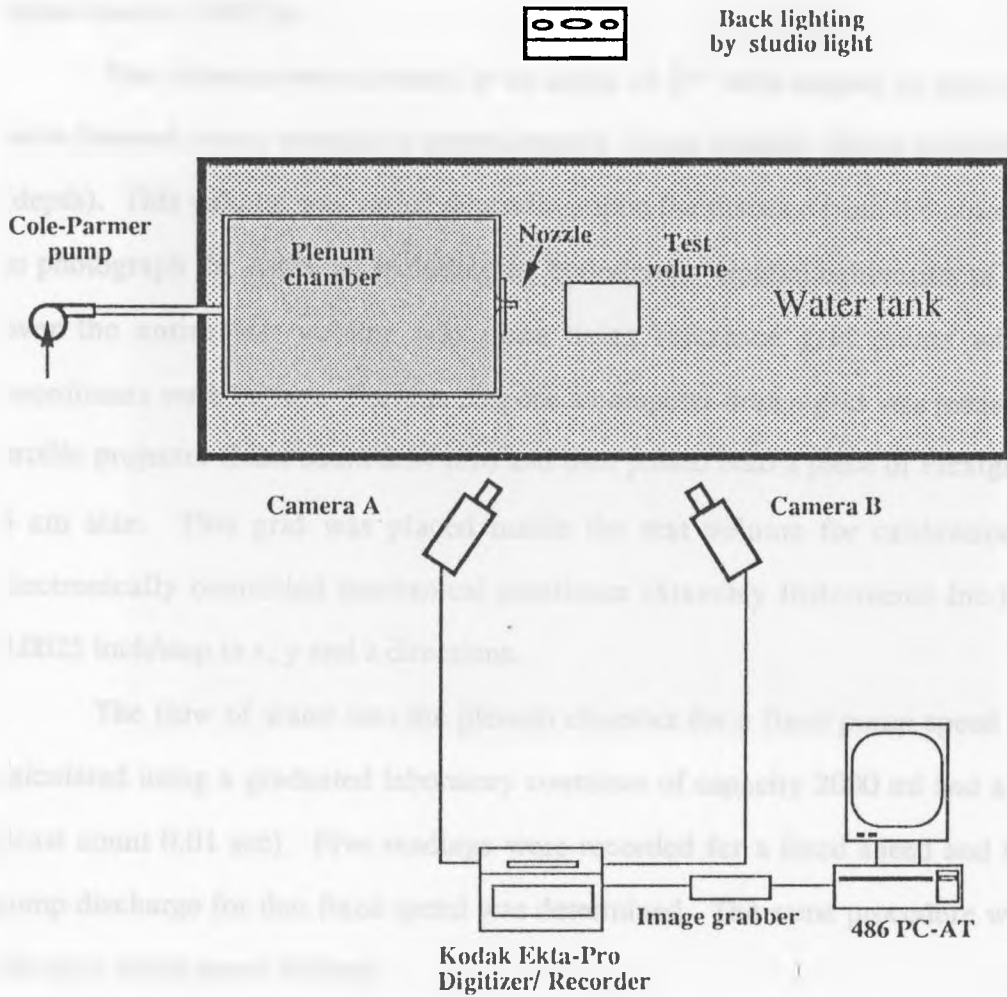


Fig. 2.2. Schematic of the experimental facility.

simultaneously. The cameras were capable of acquiring upto 6000 frames per second (fps). However, for the present study, images were captured at a rate of 2000 fps, and in some cases at 1000 fps.

The cameras were situated at an angle of 35° with respect to each other. They were focused onto a volume of approximately 15mm (width), 30mm (height) and 20mm (depth). This volume was varied depending upon the distance from the nozzle exit, so as to photograph the entire jet including its boundaries. Spatial calibration of the cameras over the entire test volume was done using reference grid points whose spatial coordinates were known. For this purpose a computer drawn grid was measured using a profile projector (least count $2.54 \mu\text{m}$) and then pasted onto a piece of Plexiglas[®] 5 cm x 5 cm size. This grid was placed inside the test volume for calibration, using an electronically controlled mechanical positioner (Staveley Instruments Inc.) capable of 0.0025 inch/step in x, y and z directions.

The flow of water into the plenum chamber for a fixed pump speed setting was calculated using a graduated laboratory container of capacity 2000 ml and a stop watch (least count 0.01 sec). Five readings were recorded for a fixed speed and the average pump discharge for that fixed speed was determined. The same procedure was repeated for other pump speed settings.

Figure 2.3 shows the photograph of the jet. The pump speed was set at 300 rpm; equivalent to 2.504 m/sec as calibrated earlier. The stage light used for the back lighting did not provide a uniform sheet of light and therefore adjustments had to be made to get reasonably uniform lighting. Since the particles were of relatively large size ($250 \mu\text{m}$), they proved to be large light-scattering sites even under lower light intensities. This made taking clear photographs of the particles possible.

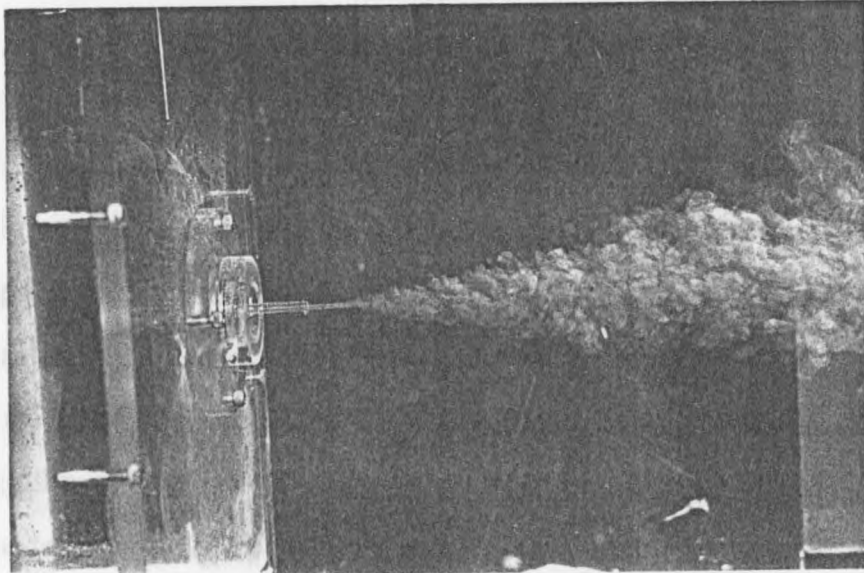


Fig. 2.3. Turbulent jet created for the study.

2.2 CAMERA CALIBRATION AND DATA REDUCTION EQUATIONS

Camera calibration implies determining the relationship between the points in space and their images in the two stereo photographs. These relationships can be established through the collinearity condition. This means that the object point, camera lens center and the image of the object point lie on the same straight line (light ray), provided all three are in the same optical medium. This is shown schematically in Fig. 2.5. The actual media in which these three entities lie, determine whether the light ray joining the three is broken or straight. In particle tracking velocimetry, often the tracer particles flow with the fluid and the cameras are kept in the air with a transparent wall made of glass or Plexiglas® separating them. Because of this multimedia environment the light ray joining the object and the image is broken several times.

If the effect of refraction can be ignored, the modeling of this situation is simple and straightforward and an elementary knowledge in geometry suffices. The analytic camera model relating the 3-D coordinates of the points in object space to the 2-D coordinates of their images has been very well understood; this is described below.

The object is said to be in the "world coordinate" (space) frame and the image is defined with respect to the "image coordinate" frame. Figure 2.4 shows the coordinate system used for the present viewing configuration. A simple model can be derived by treating a picture as a central projection of the object. See Fig. 2.5 for an example of central projection where the image is formed in front of the lens. Point O_A (X_{OA} , Y_{OA} , Z_{OA}) is the camera lens center location with respect to the origin of the world coordinate frame. The parameters ω_A , ϕ_A , ψ_A are the angles of rotation of the world coordinate system with respect to its own axes, so that the world coordinate system and the image coordinate system are aligned. Angle ω_A is the angle of rotation of world coordinate

system with respect to its X axis. Angle ϕ_A is the angle of rotation of the resulting coordinate frame with respect to its Y axis. Angle ψ_A is the angle of rotation of the coordinate frame resulting from the previous two rotations with respect to its Z axis. The parameters X_{OA} , Y_{OA} , Z_{OA} are the distances through which the world coordinate origin is translated, so that it coincides with the origin of the image coordinate frame. These six parameters (rotations and translations) for each camera are known as the camera external parameters. The principal point is the point in the image coordinate frame where the origin of the world coordinate frame forms an image. The distance between the principal point and the camera lens center is known as the principal distance f (see Fig. 2.5). The coordinates of the principal point in the image plane are denoted as x_{app} and y_{app} . The parameters f , x_{app} and y_{app} are called camera internal parameters.

Once the origins of both coordinate frames are coincident after translations and rotations, the image and the object can be visualized to reside on the same side in front of the camera lens center in central projection. Therefore a straight line equation can be applied to the three points: namely, object point in space, camera lens center and the image point formed in between these two (Fu et. al., 1987). The ratios of similar triangles thus constructed are measures of the magnification of the photograph (see Fig. 2.6). The similar triangles in vertical direction are $OP'Q'$ and OPQ . The ratio between PQ (object) and $P'Q'$ (image) is the magnification in the vertical direction. Similarly the ratio between PR and $P'R'$ is the magnification in the horizontal direction. Thus any point $P (X, Y, Z)$ in the world coordinate frame is related to its image coordinates x_a, y_a in the image plane of camera A and image coordinates x_b, y_b in the image plane of Camera B, by the following equations

$$x_a = f_a \left(\frac{a_{11}(X-X_{OA}) + a_{12}(Y-Y_{OA}) + a_{13}(Z-Z_{OA})}{a_{31}(X-X_{OA}) + a_{32}(Y-Y_{OA}) + a_{33}(Z-Z_{OA})} \right) + x_{app}, \quad (2.1)$$

$$y_a = f_a \left(\frac{a_{21}(X-X_{OA}) + a_{22}(Y-Y_{OA}) + a_{23}(Z-Z_{OA})}{a_{31}(X-X_{OA}) + a_{32}(Y-Y_{OA}) + a_{33}(Z-Z_{OA})} \right) + y_{app}, \quad (2.2)$$

$$x_b = f_b \left(\frac{b_{11}(X-X_{OB}) + b_{12}(Y-Y_{OB}) + b_{13}(Z-Z_{OB})}{b_{31}(X-X_{OB}) + b_{32}(Y-Y_{OB}) + b_{33}(Z-Z_{OB})} \right) + x_{b_{pp}}, \quad (2.3)$$

$$y_b = f_b \left(\frac{b_{21}(X-X_{OB}) + b_{22}(Y-Y_{OB}) + b_{23}(Z-Z_{OB})}{b_{31}(X-X_{OB}) + b_{32}(Y-Y_{OB}) + b_{33}(Z-Z_{OB})} \right) + y_{b_{pp}}. \quad (2.4)$$

The detailed derivation of Eqs. (2.1)-(2.4) is given in Appendix A.

The world coordinate origin was selected to be in the center of the calibration grid that was seen by the cameras. This made the measurements of X, Y, and Z coordinates of the grid points with respect to the world coordinate origin simple. The grid was positioned at several depth (Z) planes in the test volume and its images were recorded. This is equivalent to imaging a solid 3-D grid made up of the reference points.

From these images, the image coordinates of the grid points were measured in pixels. A suitable magnification can be selected during this procedure. In the present case it was selected to be 0.5 (50%). Thus the ratio of pixels on the computer screen to the image size (mm) is known. Using this, the image coordinates of the grid points were calculated in mm. The distance of the camera lens centers (O_A (X_{OA} , Y_{OA} , Z_{OA}) for camera A and O_B (X_{OB} , Y_{OB} , Z_{OB}) for camera B) from the world coordinate origin were measured. Since locating the lens centers of the camera compound lens could not be done exactly, these measurements were approximate. The rotation angles were also measured approximately.

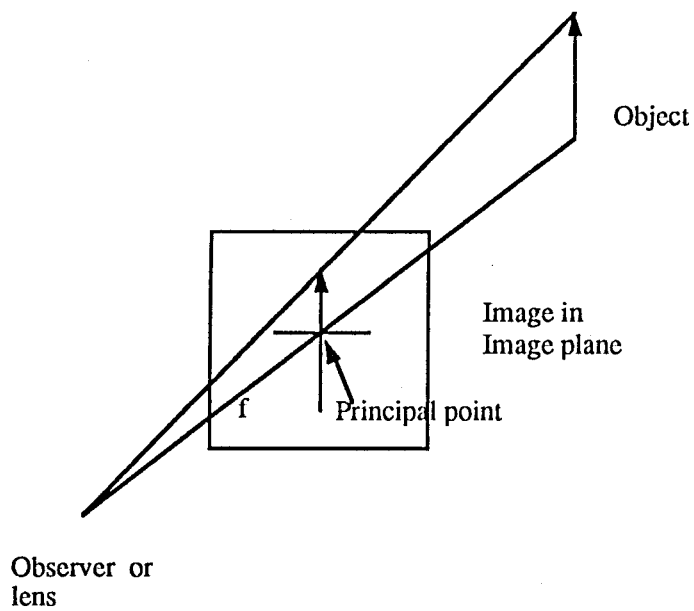


Fig. 2.5. Collinearity condition in central projection.

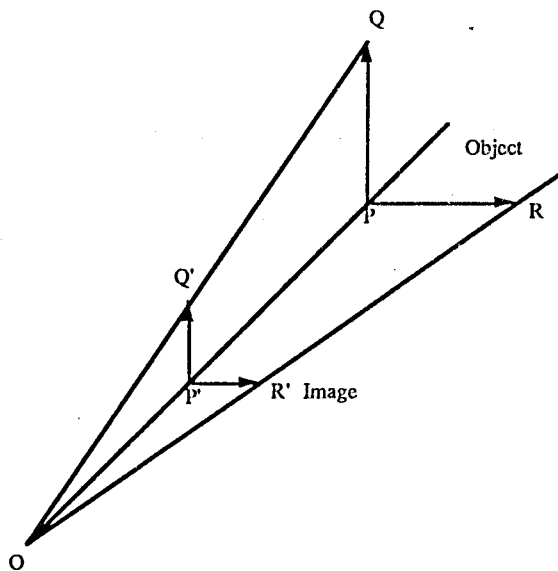


Fig. 2.6. Ratio of similar triangles as a measure of magnification.

At this point the world coordinates of the grid points (X, Y, Z), their image coordinates (x_a, y_a) and (x_b, y_b), and the approximate camera parameters were known. The approximate camera parameters were used as the initial guess. There are nine of them for each camera, for example $X_{OA}, Y_{OA}, Z_{OA}, \omega_A, \phi_A, \psi_A, f_a, x_{app}, y_{app}$ for camera A. The last three parameters (camera internal parameters) could not be measured directly and had to be estimated. Since the magnification was selected to be 0.5, it meant that the image was formed midway between the object and the lens center in the central projection. Therefore f_a could be taken approximately as one half of the distance between the object and the lens center. As far as measurements of x_{app}, y_{app} were concerned, the point where the world coordinate origin formed an image, was chosen as the origin of the camera coordinate frame. Thus x_{app} and y_{app} became zero. The relationships depicted in Eqs. (2.1) to (2.4) are non-linear. The camera parameters can be calculated more accurately if many of the non-linear terms can be made to zero. Setting x_{app} and y_{app} to zero was therefore done with this in mind.

This linearization process was further assisted by the selection of the world and the image coordinate frames, such that a small angle rotation in only one direction was sufficient to make them aligned; thus making several of the non-linear terms in the data reduction equations go to zero. The data reduction equations were solved using a non-linear least-squares optimization procedure (IMSL subroutine DUNLSJ) (Mangla, 1992). The least-squares adjusted camera parameters thus obtained were known as "modified camera parameters", since the effect of multi-media refraction was ignored in this procedure.

2.2.1 Check for Camera Parameters

The correct camera parameters should be able to reproduce the world coordinates of any point within the test volume from its image coordinates. However the omission of multi-media refraction physics from the governing Eqs. (2.1)-(2.4) will result in camera parameters that cannot reproduce the world coordinates exactly. The resulting errors are however systematic (i.e. bias), and include effects of "unknown" distortions (due to the lenses, container walls, etc.). In order to estimate the bias errors, alternate grid points (or "check points") which were dispersed throughout the test volume, were used. Their image coordinates in camera A and camera B were used in conjunction with the "modified" camera parameters (obtained by solving the Eqs. (2.1)-(2.4)) to predict their world coordinates. These predicted world coordinates were compared with the actual (measured) world coordinates. The differences of these two yielded the bias errors. The bias errors varied from point to point and with the coordinate (i.e. X, Y, or Z) in question. The maximum bias was found to be within 1/20th of a mm for X coordinates, 1/100th of a mm for Y and 1/2 of a mm in Z (depth) within the test volume.

The "check points" with their predicted X, Y, Z positions, along with their bias errors in those locations were stored as an "error file". When processing actual particle image data, the modified camera parameters were combined with the image coordinates of corresponding particle images, (corresponding meaning the images created in camera A and camera B by a single point in space) and their predicted X, Y, Z positions were calculated using Eqs. (2.1)-(2.4). These X, Y, Z positions were then corrected for the bias errors to obtain their actual positions in space. Since the particle positions were randomly distributed, the bias errors from the grid points ("error file") had to be interpolated on to the particle positions to correct for refraction and other effects. A cubic spline

interpolation scheme using the Akima algorithm (IMSL subroutine DCSAKM) was used for this purpose.

The ability of the interpolator was tested as follows. Data from the alternate grid points with associated (known) bias errors were used to interpolate onto the predicted X, Y and Z positions of the other grid points, whose bias errors were not known. Once the bias errors at these grid points were found by means of the interpolation, they were subtracted from their predicted positions so as to obtain their actual positions (X_p , Y_p , Z_p) in the world coordinate frame. These positions (X_p , Y_p , Z_p) were readily compared with their measured world coordinates. The difference between the two yielded the uncertainty associated with determining the positions in X, Y and Z directions. The RMS of the uncertainties were found to be 6.81×10^{-5} mm in X, 5.84×10^{-5} mm in Y, and 1.73×10^{-4} mm in Z (depth) directions.

The uncertainties in finding the centroids of the moving particle images can be expected to be much higher than those for finding the centroid positions of the stationary grid points used in the calibration stage. However, this negative effect was offset by the fact that correction for refraction for the particles was done using every single grid point as a check point. This denser bias error data file reduced interpolation errors.

2.3 IMAGE PROCESSING

Image processing was done to determine the positions of the centroids of the images of the grid points and particles. This involved the following steps:

- (i) Enhancing the images and setting a two-level intensity threshold level.
- (ii) Identifying the pixel blocks of distinct light intensity values as compared to their background.

(iii) Finding the centroids of the above mentioned pixel blocks.

These were easily achieved in the present case. The images of the grid points and those of the particles were quite distinct compared to their background. Since very little noise was observed in the images, simple thresholding was found to be sufficient. The centroid positions of these features (grid points and particle images) were found to within sub-pixel accuracy. A better segmenter (Sobel, 1974) would have been necessary had the images contained more noise. Finally a size threshold (empirically found) was set to eliminate the images where one or more particles hide each other or coalesce and form bigger blobs compared to a single particle image. Figure 2.7 shows the steps involved during image processing. Figure 2.8 shows the salient steps in the subsequent data processing so as to calculate the particle positions in space.

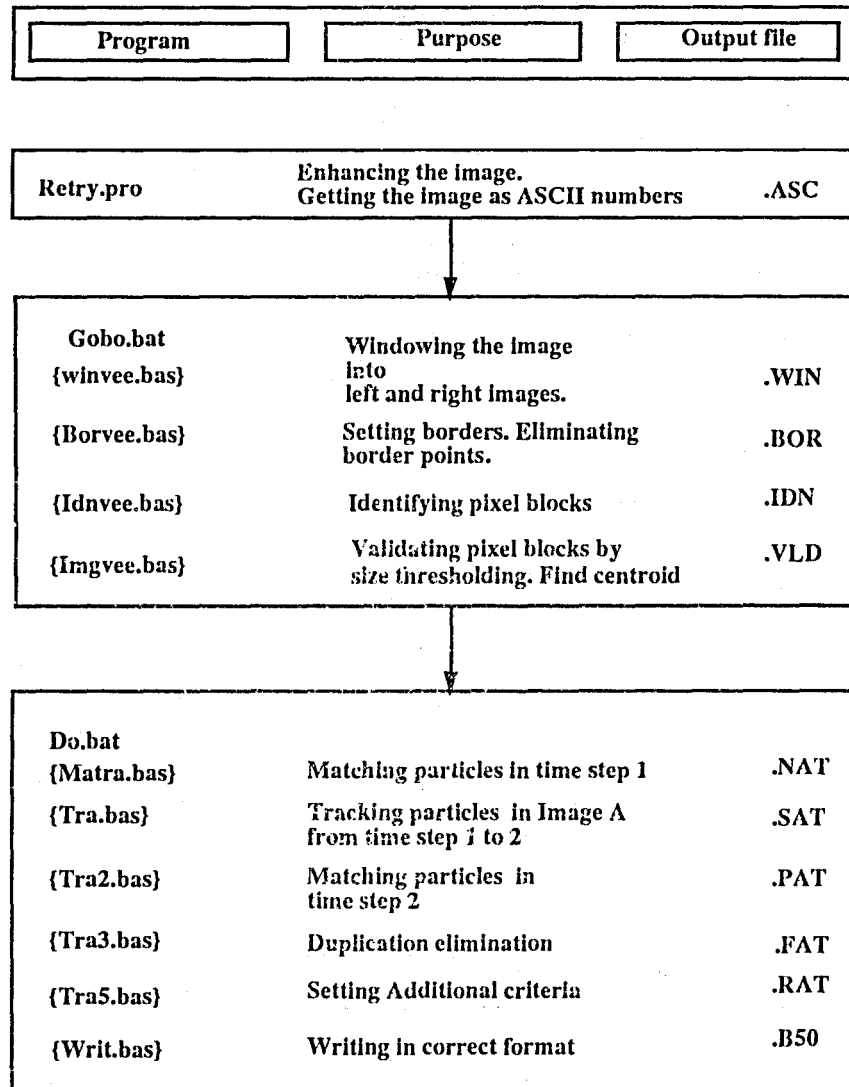


Fig. 2.7. Salient steps in image processing.

Chapter 3

AUTOMATIC MATCHING AND TRACKING OF PARTICLES

3.1 INTRODUCTION

As was stated earlier, one of the problems in particle tracking velocimetry is to identify the corresponding images of the same particle in the stereo images and track them through the next and subsequent time steps. The algorithm development to match and track the particles is of considerable importance. This chapter describes the development of such an automatic matching and tracking algorithm.

3.2 MOTIVATION FOR THIS WORK

Automatic perception of 3-D objects (in our case particles in space) is of significant interest in a variety of fields. Obtaining good quality images and analyzing the image data for longer duration are two important requirements in particle tracking velocimetry. Due to recent advancements in imaging techniques, good quality pictures of the particles in the flow can be readily obtained. Finding correct correspondences of particles in both views, and tracking them over several time steps is necessary to obtain meaningful data from unsteady and turbulent flow fields. Here the basic approach is described, and some of the conditions needed to arrive at the most probable match and track are also explained. A "match" is referred to a corresponding image in the other view at the same time step. A "track" is referred to a corresponding image in the same view at the next time step.

3.3 BASIC APPROACH

Given one view of a point in space, and the camera location, one can construct a ray of light connecting the image point, camera center and the object point (see Fig. 3.1). As seen from the figure, all object points lying on the ray of light will form images at the same point in the image plane irrespective of their different depth positions in space. To resolve this ambiguity and to find the depth locations of each point, a second camera image is absolutely necessary (see Fig. 3.2).

Moreover, it can be seen that the points falling on the light ray constructed from the left camera image can only be situated on a horizontal line in the right camera image provided the principal axes of both cameras lie on the same horizontal plane (i.e. the cameras are located on the same horizontal plane). Because of measurement errors, and uncertainties associated with identifying the correct ray, the point will form images within a horizontal band in the right camera image. As seen in Fig. 3.3, a triangle can be formed with points O_A , O_B and P with $O_A O_B$ forming the base of the triangle. Here P is the base of an extended object. As long as camera centers O_A and O_B are in the same horizontal plane as P , and the magnifications of both cameras are equal, the images formed in both the cameras are of equal heights (i.e. $h_a = h_b = mh$, where h_a is the height of the image formed in camera A; h_b is the height of the image formed in camera B; h is the actual height of the object; m is the magnification factor). O_A , O_B and P may be imagined to be on a table top, and a common coordinate system called the "table top coordinate" system can be used to establish that the images are equal in height (Ganapathy, 1975). The arrow PQ is called the vertex. In 3-D solids, as in a cube, this could be one of the edges.

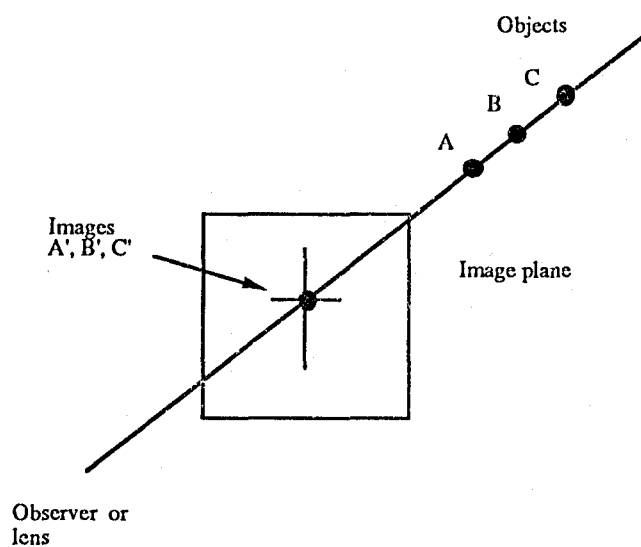


Fig. 3.1. Single camera view.

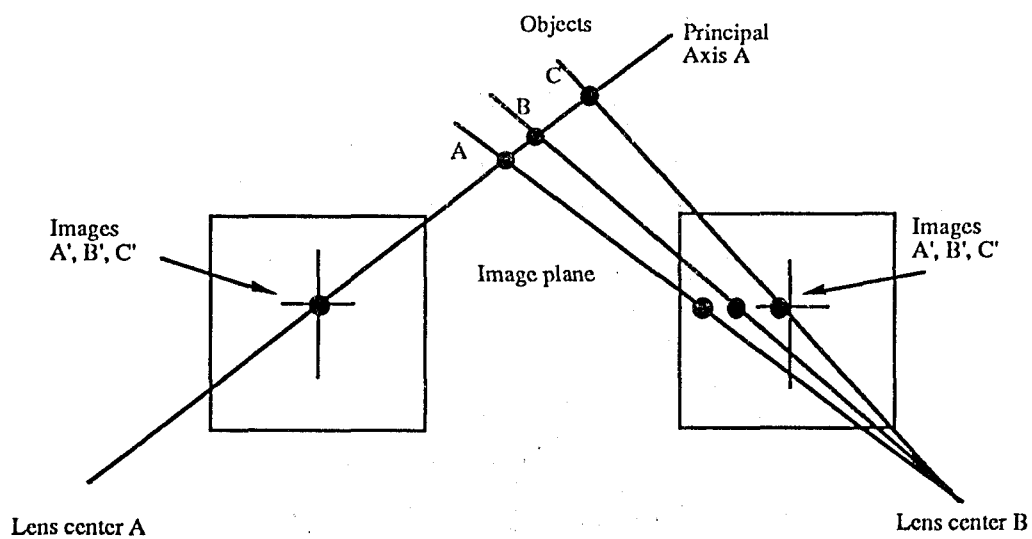


Fig. 3.2. Two camera stereo view.

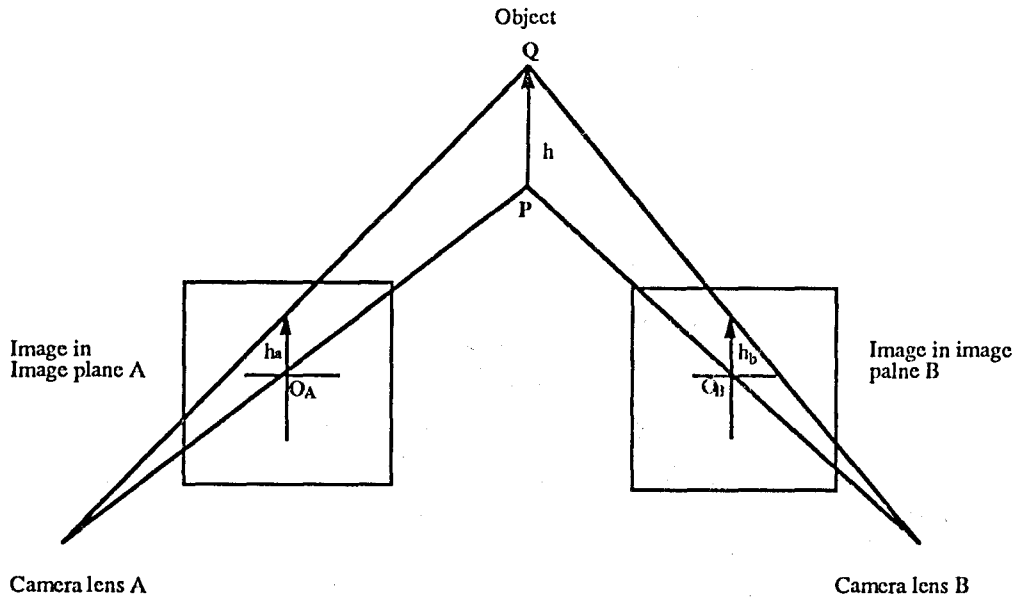


Fig. 3.3. Vertical height comparison between the object and its image.

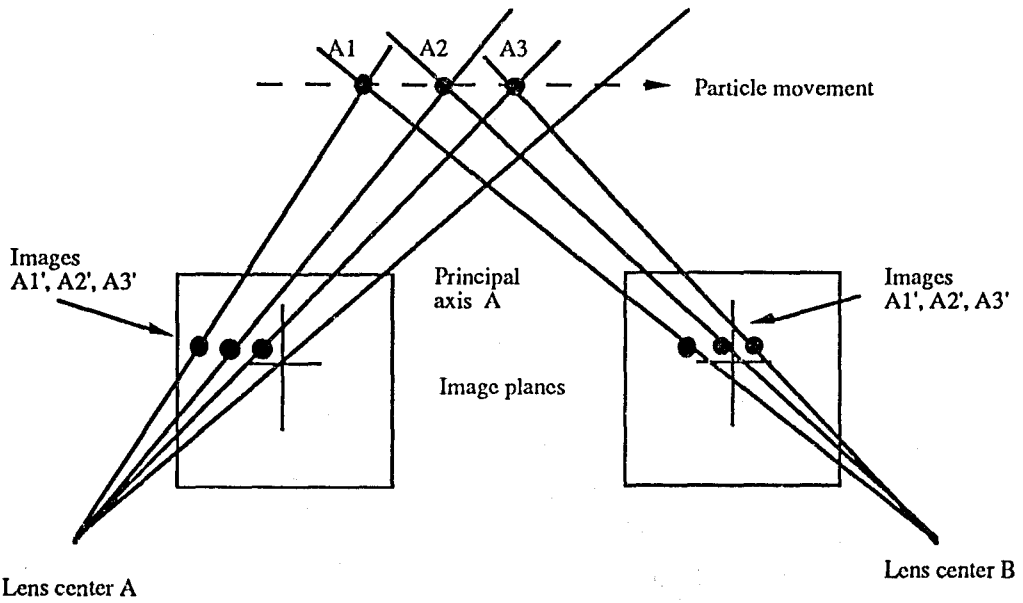


Fig. 3.4a. Particle movement in X-axis as seen by the camera.

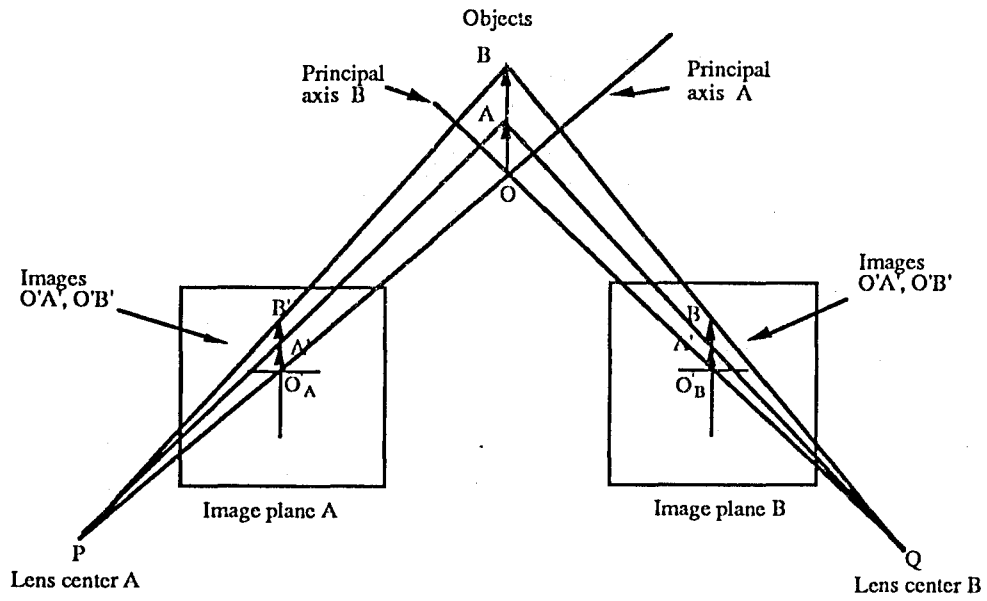


Fig. 3.4b. Particle movement in Y-axis as seen by the camera.

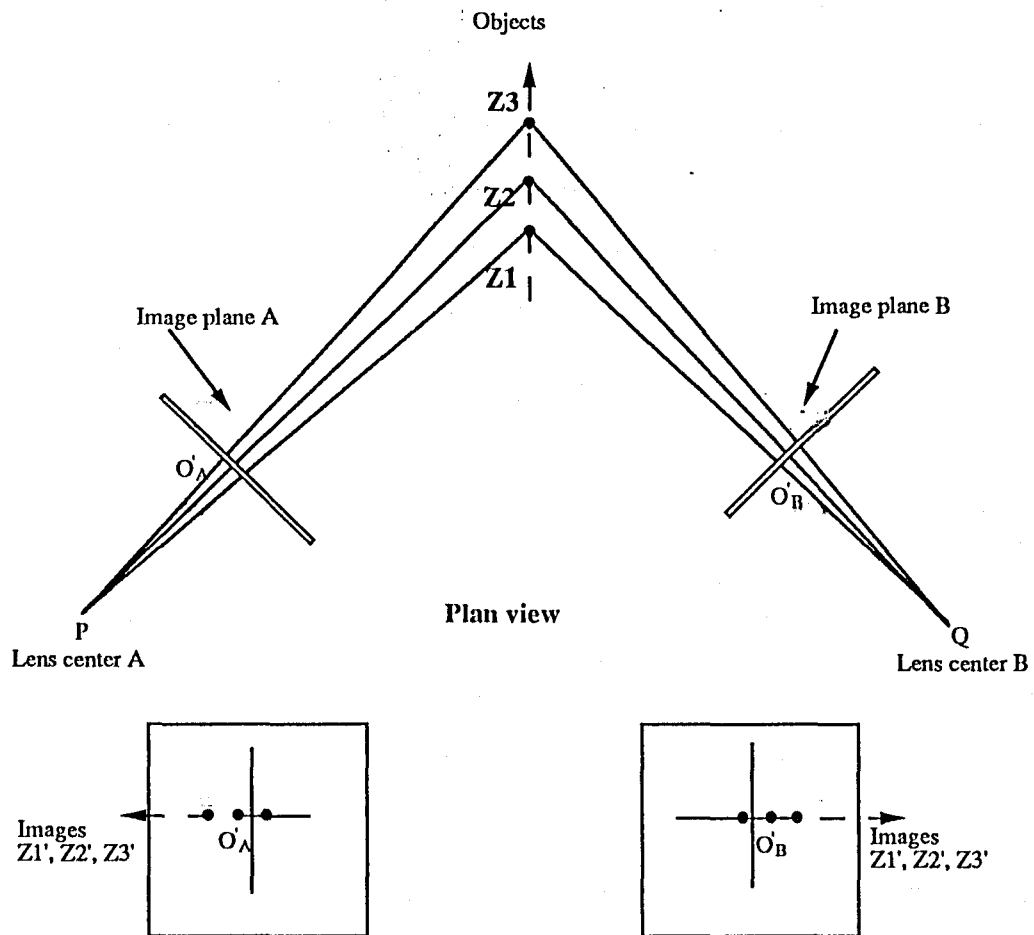


Fig. 3.4c. Particle movement in Z-axis as seen by the camera.

3.4 FORMULATION OF THE PROBLEM

The problem is matching the particles in the left and right camera images on a one-to-one basis. However all points in the left image may not have unique matches in the right image. The regions viewed by the left and right cameras will not be exactly same. Because of this reason, particles entering and leaving the view may not form images in both cameras. As a result of viewing from two different directions, the spacing between the particle images in the left camera may often be different from those in the right camera. Due to the different spacing between the particles in the left and right images, two distinctly visible particle images in the left camera may form two overlapping particle images (or a single spot) in the right camera. The converse is also true. Therefore particles in the left image may have non-unique matches in the right image. Additional pieces of information are needed to resolve these ambiguities.

3.4.1 Basic Criteria

Figures 3.4a, 3.4b and 3.4c show the movement of the particle in X, Y and Z directions respectively as seen by the cameras. Figure 3.5 shows the typical image taken by the cameras where the right half is the image formed by the right camera and the left half is due to the left camera. In the images A and B (which are two-dimensional) particle movements consist of combinations of vertical and horizontal movements. Vertical movement of the particle between one to the next time step is recorded as equal displacements (see Fig. 3.4b) in both cameras and horizontal movement is recorded as comparable displacements (see Fig. 3.4a) in camera A and camera B. Therefore to identify a particle in one time step and to detect its movement to the next time step, vertical displacements as recorded in the images A and B are used as the primary

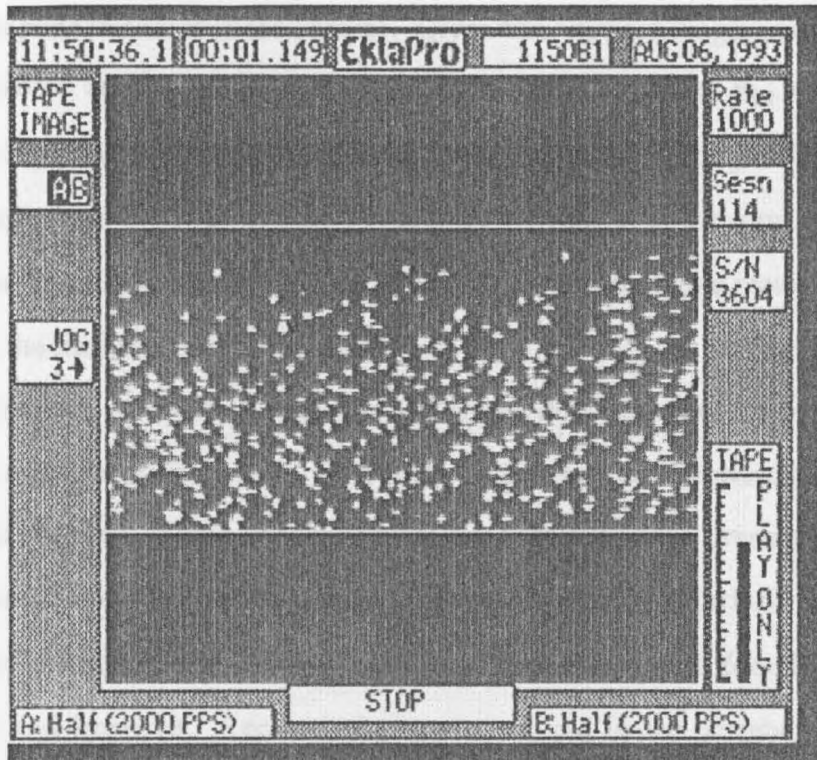


Fig. 3.5. Typical image of particles in the jet.

criterion. Horizontal movements as recorded in the images are used as the secondary criterion.

The process of matching starts from the left image. Thus every particle image in the left image may or may not have a match in the right image. The left and right images consist of a set of vertical heights say V_L and V_R respectively, measured from a common base as explained earlier in the chapter. Given two views, a single point in the left image has n possible number of matches in the right image such that $V_{Li} = V_{Rj}$, where $j = 1, 2, \dots, n$; see Fig. 3.6 for matching criterion. This has reduced the possible matches in the right image from $j = 1, 2, \dots, N$ to $j = 1, 2, \dots, n$ where N is the total number of particle images in the right image and $N \gg n$. To find the most probable match from the possible matches, the tracking criterion is used.

Tracking of a particle is simply to find out the position of the particle image in the next and subsequent time steps. To track the particle, some knowledge of the flow being studied is required. Some problems were encountered in the present study to track the same particle over several time steps. Since the flow was turbulent ($Re = 8000$) the motion of the particles from one time step to the next was found to be completely unsteady and irregular. Recirculation was observed in the periphery of the jet. The boundaries were wavy. Some of the other features observed are ejection to and entrainment from the boundaries, non-uniform spatial distribution of the particles and migratory movement of the particles across the jet. To add to the complexity of the situation some of the out-of-focus particles were also photographed by the cameras. Therefore specifying a criterion for the particle movement over several time steps was found to be difficult and prone to misinterpretation. Therefore, an empirical search volume was specified based on the average of the actual movements of the particles in

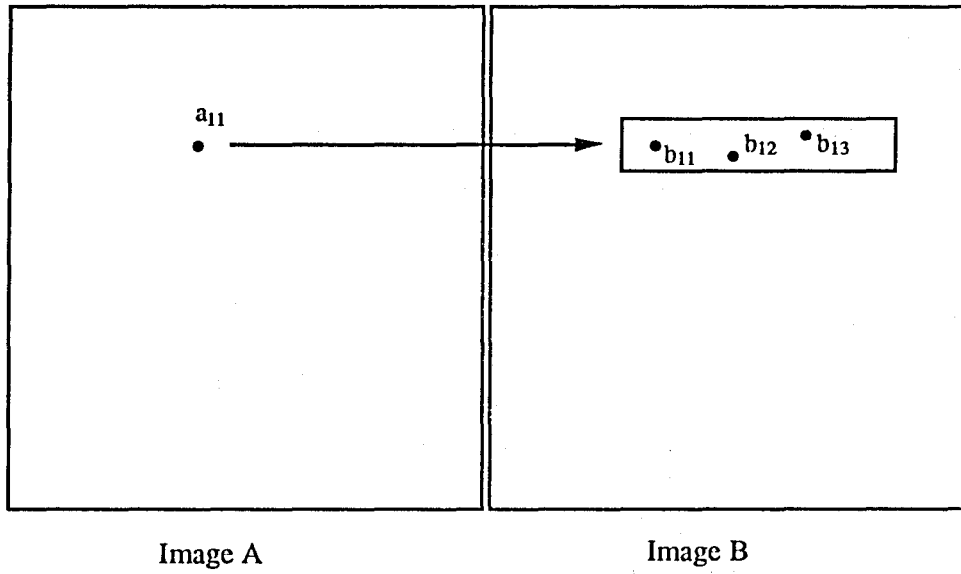


Fig. 3.6. Matching of particles between image A and image B in time step 1.

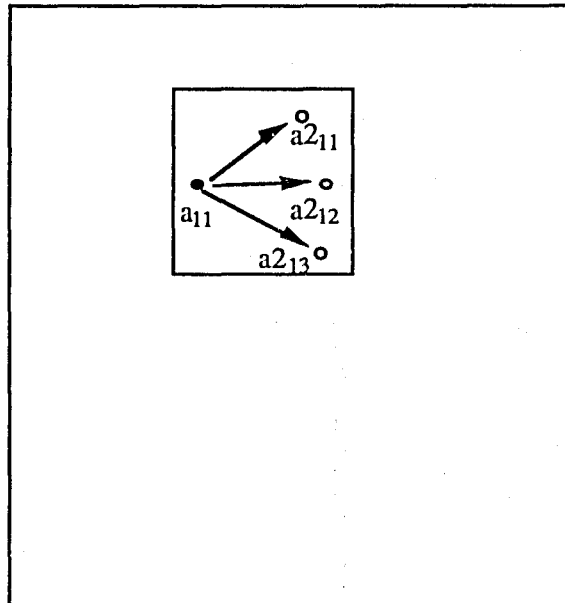


Fig. 3.7. Tracking particles from one time step to the next.

pixels/time step as seen in the video images between two time steps. See Fig. 3.7 for the search window to find the particle image in the next time step. Hereafter the left camera is denoted as camera A and right as camera B. The following notations are used:

"a" is the particle in image A at time step 1 and $x_a(i)$, $y_a(i)$ are its coordinates, where $i = 1, 2, \dots, N$,

"b" are the particles which are possible matches in image B at time step 1 for the particle "a" and $x_b(i, k)$, $y_b(i, k)$ are their coordinates, where $i = 1, 2, \dots, n$,

"a2" are the particles which are possible tracks in image A at time step 2 for the particle "a" and $x_{a2}(i, j)$, $y_{a2}(i, j)$ are their coordinates, where $j = 1, 2, \dots, m$,

"b2" are particles which are possible matches in image B at time step 2 and $x_{b2}(i, j, l)$, $y_{b2}(i, j, l)$ are their coordinates, where $l = 1, 2, \dots, p$.

The following steps explain the matching and tracking processes:

Step 1: $a(i)[x_a(i), y_a(i)]$ has possible matches $b(i, k)[x_b(i, k), y_b(i, k)]$ at time step 1 where $k = 1, 2, \dots, n$ (i.e. particle $a(i)$ in image A has k number of matches in image B. See Fig. 3.6 where k is 3),

Step 2: $a(i)[x_a(i), y_a(i)]$ has possible tracks $a2(i, j)[x_{a2}(i, j), y_{a2}(i, j)]$ at time step 2 where $j = 1, 2, \dots, m$ (i.e. particle $a(i)$ in image A has j number of tracks in image A at the next time step. See Fig. 3.7 where j is 3),

Step 3: $a2(i, j)[x_{a2}(i, j), y_{a2}(i, j)]$ have possible matches $b2(i, j, l)[x_{b2}(i, j, l), y_{b2}(i, j, l)]$ at time step 2 where $l = 1 \dots p$ (i.e. particles j which were found in the previous step have l number of matches in image B. See Fig. 3.8 where l is 3 (CAND 1 etc.))

Now, for a single particle in image A in time step 1 (one), there are many possible matches in image B at time step 1, and many possible tracks in image A at time step 2, for which there are a number of possible matches in image B at time step 2 (see

Fig. 3.8). The task is to eliminate inaccurate and improbable matches and tracks from the multiple choices. This was done as follows:

The notation $\overline{A.B}$ denotes the magnitude of the distance vector joining points A and B. Here the notation is used to denote the displacement (in X and Y directions) of the particle from one time step to the next. Since, as a result of above operations, many possible matches and tracks are found for a single particle, a comparison of displacements of the particle is done (i.e. the displacement of a particle in image A is compared with that of image B) to find the most probable match and track. Here displacement means the particle image movement from one to the next time step. As explained earlier, the vertical displacement is used as the primary criterion and the horizontal movement as the secondary criterion for the comparison. The comparison is performed for every single set of possible candidates found in matching and tracking steps. This is described below. If indeed the particle $a_2(i, j)[x_{a2}(i, j), y_{a2}(i, j)]$, (where j is a fixed number say, 2) is the actual track for particle a(i), it should have a possible match in the set containing $b_2(i, j, l)[x_{b2}(i, j, l), y_{b2}(i, j, l)]$ where $l = 1, 2, \dots, p$ such that $\overline{y_{a(i)}.y_{a2}(i, j)}}$ is equal to $\overline{y_{b(i, k)}.y_{b2}(i, j, l)}}$. Additionally, since the particles move in the direction of the jet, $\overline{x_{a(i)}.x_{a2}(i, j)}}$ should be in the same direction as and comparable to $\overline{x_{b(i, k)}.x_{b2}(i, j, l)}}$. Allowing for measurement errors and uncertainties, a tolerance of ± 0.75 pixels in the Y direction (ytolerance) and ± 2 pixels in the X direction (xtolerance) were given. Therefore the criteria were modified as

$$\{\overline{y_{b(i, k)}.y_{b2}(i, j, l)} - ytolerance\} \leq \overline{y_{a(i)}.y_{a2}(i, j)} \leq \{\overline{y_{b(i, k)}.y_{b2}(i, j, l)} + ytolerance\}$$

$$\{\overline{x_{b(i, k)}.x_{b2}(i, j, l)} - xtolerance\} \leq \overline{x_{a(i)}.x_{a2}(i, j)} \leq \{\overline{x_{b(i, k)}.x_{b2}(i, j, l)} + xtolerance\}$$

The result is sets of four positions for each particle in space, namely:

- (i) position of the particle image in image A at time step 1,
- (ii) position of the particle image in image B at time step 1,
- (iii) position of the particle image in image A at time step 2, and
- (iv) position of the particle image in image B at time step 2.

Figure 3.8 shows three possible tracks in image A and each track has three possible matches in image B at time step 2. Of the nine possible tracks in image B, the most probable tracks are shown in Fig. 3.9. This assumes that at the point in question the jet flows from left to right, and backward movement (i.e. right to left) is not possible. Thus some knowledge about the flow is needed for this to work.

The resultant of the above operations may not always yield a unique match and track for a particle in time step 1 and 2. To elaborate, $x_a(i)$, $y_a(i)$ may have more than one set of matches and tracks. At this point additional conditions are required to resolve the ambiguities.

3.4.2 Additional Conditions

The additional conditions are as follows.

- (i) A particle in image A at time step 1 has one and only one match in image B at time step 1.
- (ii) A particle in image A at time step 1 has one and only one track in image A at time step 2.
- (iii) A particle in image A at time step 2 has one and only one match in image B at time step 2.

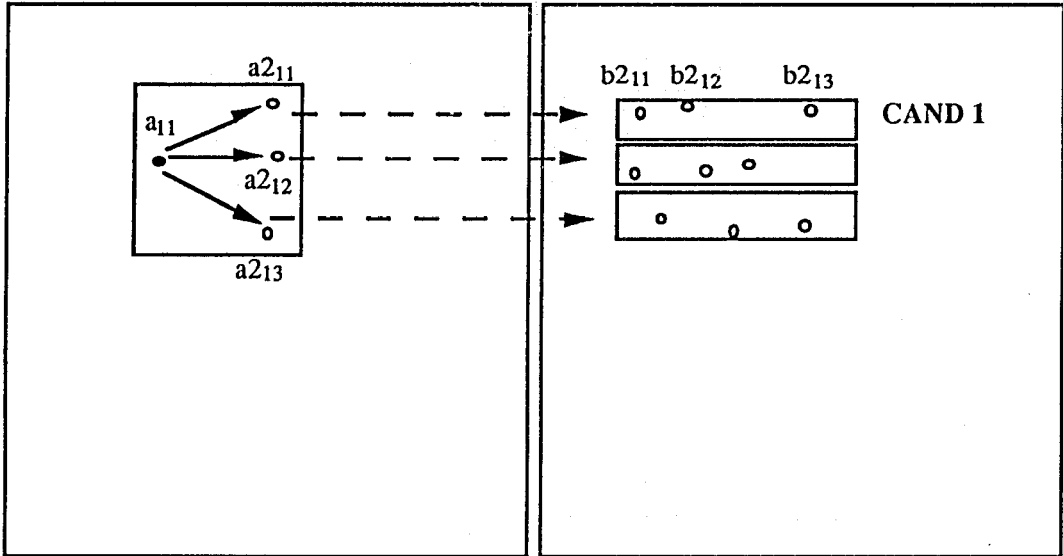


Image A time step 1 super imposed on Image A time step 2

Image B time step 2

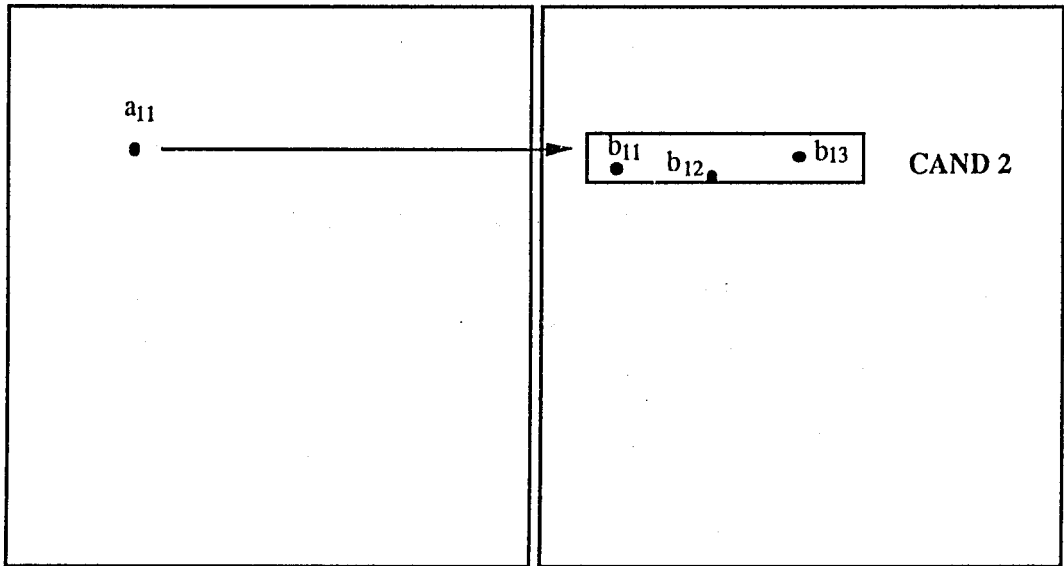


Image A time step 1

Image B time step 2

Fig. 3.8. Multiple correspondences in matching and tracking.

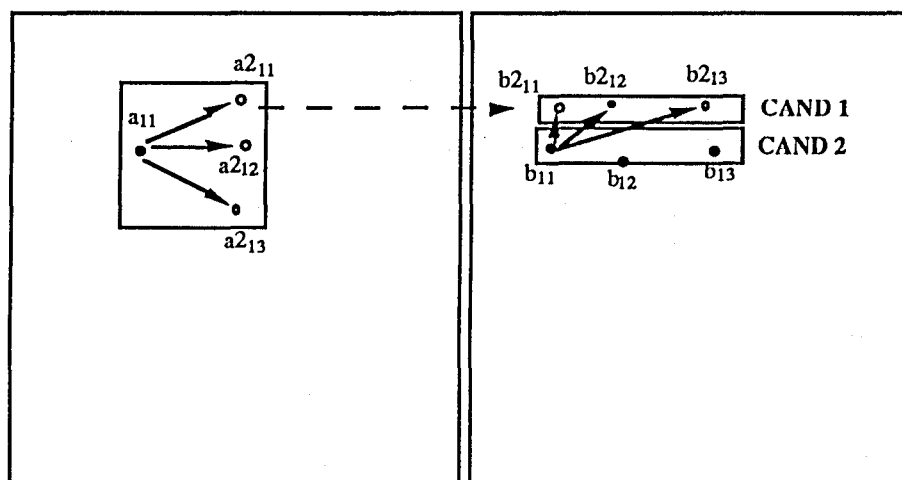


Image A time step 1 super imposed on
Image A time step 2

Image B time step 1 super imposed on
Image B time step 2

Fig. 3.9. Comparison of particle movement in Stereo View.

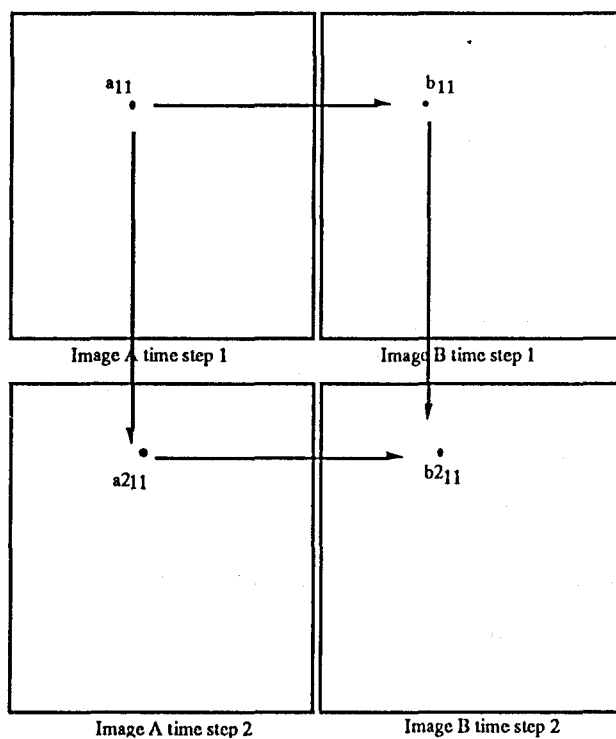


Fig. 3.10. One-to-one correspondence in particles.

(iv) A particle in image B at time step 1 has one and only one track in image B at time step 2. To apply the above mentioned conditions (i) to (iv), uniquely matched and tracked particle images obtained from the previous step should be kept aside and the same are not allowed to be associated with any other particle images. All repetitions can be eliminated from the multiple choices in this manner (see Fig. 3.10). The resultant is put through the last criterion as follows.

After eliminating the repetitions in the particle positions which have multiple matches and tracks, still some of the particles may have more than one set of possible matches and tracks, namely, $(x_a(i), y_a(i); x_b(i, k), y_b(i, k); x_{a2}(i, j, l), y_{a2}(i, j, l); x_{b2}(i, j, l), y_{b2}(i, j, l))$. To determine the most probable match and track, a comparison is made between $\overline{y_a(i).y_{a2}(i, j)}$ and their corresponding $\overline{y_b(i, k).y_{b2}(i, j, l)}$. As a result of this operation one single set of $\{[x_b(i), y_b(i)], [x_{a2}(i), y_{a2}(i)], [y_b(i), y_{b2}(i)]\}$ can be assigned to $x_a(i), y_a(i)$ in most cases.

Thus we have only one set consisting of four positions for every particle position in space, namely

- (i) position of the particle image in image A at time step 1,
- (ii) position of the particle image in image B at time step 1,
- (iii) position of the particle image in image A at time step 2, and
- (iv) position of the particle image in image B at time step 2.

It should be mentioned that the automatic matching and tracking procedure is not fool-proof, since wrong matches and tracks may occur. Also there will be some particles which will not have any matches or tracks and which will have more than one match or track. In the present case, non-uniform matches/tracks were not considered as valid data.

To check these it was decided to simulate the flow situation and test the algorithm to estimate its reliability.

3.4.3 Testing of the algorithm

As a preliminary check it was decided that the simulation be performed on a relatively simple flow. A 2-D flow with maximum velocity at the center and minimum velocities at the boundaries was conceived. In the real world this would be similar to a 2-D open channel flow. Screen (pixel) coordinates of artificial particle images in images A and B were needed to apply the matching and tracking algorithm. For this purpose any set of artificial camera parameters can be assumed. However a set of camera parameters that were taken from an actual experiment were utilized. This was to approximate the real world conditions more closely. Moreover, least-squares adjusted camera parameters are inherently stable in predicting the location (X, Y, Z) of a particle given its image coordinates in left and right images. The cameras were situated at an angle of about 30° with respect to each other, symmetrically viewing the test volume of size 18mm x 18mm x 10mm (depth). This was the experimental setup used for investigating a flow from a submerged tube issuing into the still water in a larger tank (Rajendran et al., 1993).

The particles (120 in number) were assumed to be situated in a regular pattern covering the entire test region in the first time step. Next, it was assumed that the particles moved as if they were flowing in a 2-D channel flow, thus having maximum displacement in the axis of the flow and minimum displacement at the boundaries. Spatial positions (X, Y and Z) of the particle positions were assumed and they were combined with the camera parameters to get the particle image coordinates. These positions were converted to screen (pixel) coordinates. Then the matching and tracking

criteria were specified. The maximum displacement a particle could undergo in the axis of the flow was specified as the limit for the tracking criterion. Both matching and tracking algorithms performed very well. The matching algorithm picked up all (100%) corresponding particles, though multiple matches occurred. The tracking algorithm had tracked all the corresponding tracks into the next time step. Since the flow was uniform, it was possible to match and track all particles between two consecutive time steps.

Then it was decided to simulate the turbulent flow for which the algorithms were developed. Particles were assumed to be situated in random X, Y and Z positions in the test volume at time step 1. This was accomplished by creating a random number set for X, Y and Z positions within the test volume. At the next time step, the particles were assumed to have moved randomly. These positions were also obtained by generating a random number set for the displacements in the X, Y and Z directions. This simulation approximated the real flow very well. The automatic matching and tracking algorithm was tested for this case. The matching algorithm detected corresponding matches for 95% of the particles at time step 1. About 50% of those had more than one corresponding match. As in the real flow, the particles in the borders were not matched. The tracking algorithm tracked about 85% of the same particles into the next time step. About 70% of these were found to have multiple correspondences. However, when subsequent criteria were applied to eliminate the ambiguities and to find out the most probable correspondences in matching and tracking, it was found that only 63% of all the particles were matched and tracked. Since the criterion for the vertical movement of the particles was specified as ± 0.75 pixels, some of the correct matching and tracking correspondences were lost. This close tolerance was needed to eliminate any chances of picking incorrect correspondences. Because of the random displacements which the

particles were subjected to, the particle occlusion problem contributed to the loss of some of the correspondences. The particles matched and tracked into the next time step uniquely numbered 75 out of the total 120 particles available for matching and tracking. Out of these, about 15% of particles were selected randomly. The matching and tracking processes were manually verified. No incorrect correspondences were found. Therefore the algorithm was assumed to perform satisfactorily.

Chapter 4

OVERVIEW OF TURBULENCE IN A SUBMERGED JET

4.1 INTRODUCTION

The stereoscopic particle tracking velocimetry (SPTV) technique was used to measure instantaneous velocities both spatially and temporally, in an axisymmetric submerged water jet. The submerged jet flow was selected since it is a relatively simple shear flow with a wide range of practical applications. It has been well documented over several years, and comparisons could be made with previous measurements and observations. Since it is important to have a basic knowledge of the flow being studied, the following section outlines the theory and some of the phenomena observed in the submerged jet as a result of previous investigations.

4.2 SUBMERGED JET

Figure 4.1 shows the conceptual sketch of a turbulent jet. The type of turbulent jet most studied is one spreading through a uniform medium at rest. A jet of this kind is said to be submerged. The velocity field in the initial cross section of the submerged jet is assumed to be uniform. Mixing layers are formed due to the extremely large local velocity gradients resulting from the difference in velocities of the jet and the surrounding quiescent fluid. The mixing layers originate from the edges of the nozzle. The inner boundaries of the mixing layers meet on the center-line of the jet. The outer boundaries of the mixing layers diverge into the quiescent fluid. The region between the nozzle exit

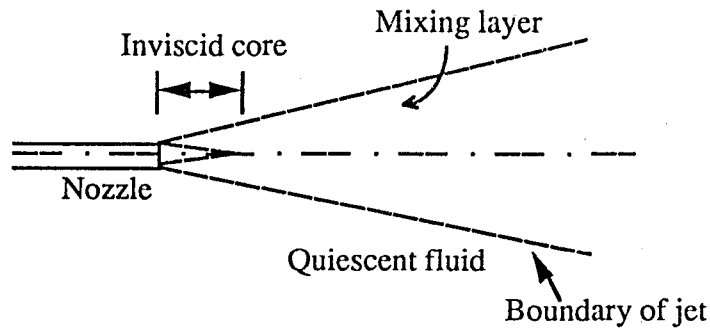


Fig. 4.1. Sketch of a turbulent jet.

and the point where the mixing layers meet is an inviscid core. This inviscid core lasts few diameters from the nozzle exit. The region downstream of the point where the mixing layers meet is a fully developed self similar region (Abramovich, 1963).

As shown by numerous experiments and theory, the mean transverse velocity components in any section of the jet is an order of magnitude smaller than the longitudinal velocity. The same had been verified by the experimental results from the previous investigations. The experiments show a continuous broadening of the velocity profile of the jet. The velocity profile becomes "lower" and "wider" with increasing distance from the nozzle exit. However the velocity profiles coincide with one another when they are plotted in the dimensionless form.

Several parameters can be used to non-dimensionalize the axial velocity and the transverse distance. The center-line velocity u_m , and y_c (the distance between the axis and the point at which the velocity is equal to half that of the center-line velocity) are commonly used for this purpose. Other distances, such as the jet diameter are also used.

The equality of the dimensionless velocities for corresponding points in the jet is then expressed in the following way

$$u_1/u_{1m} = u_2/u_{2m} \quad (4.1)$$

where u_1 and u_2 are the velocities at corresponding points of two cross sections of the jet; u_{1m} and u_{2m} are the appropriate velocities at the center-lines of these cross sections. Based on Prandtl's mixing length theory, a simple relationship can be derived for the jet growth rate along its axis. By establishing a relationship between the increase in the thickness of the submerged jet and the mixing length in the direction of the flow

$$db/dx = \text{const}, \quad b = C_1 x \quad (4.2)$$

where db/dx is the growth rate of the jet, x is the axial distance from the jet exit and C_1 is a constant determined empirically. The total momentum of the fluid per unit time should be the same in all cross sections of the jet. Based on this the decrease in the axial velocity of the jet as a function of distance from the jet exit can be arrived at

$$u_m = Cx^k. \quad (4.3)$$

The value of k depends on the type of the jet. For example round submerged jets have k of -1 and plane-parallel jets have a k of $-1/2$. Görtler (1942) theory for round submerged jets gives the velocity profile (White, 1975, Schlichting, 1979)) as

$$\frac{\bar{u}}{U_{\max}} \approx \left(1 + \frac{\zeta^2}{4}\right)^{-2}, \quad (4.4)$$

where

$$\zeta \approx 15.2 \frac{y}{x}, \quad (4.5)$$

and

$$U_{\max} \approx 7.4 \frac{\left(\frac{J}{\rho}\right)^{\frac{1}{2}}}{x}, \quad (4.6)$$

where J is the jet momentum, ζ is the similarity variable, ρ is the density of the fluid, U_{\max} is the maximum velocity at the center-line of the jet and x is the distance from the nozzle exit. Excellent agreement had been found between theory and experiments by Corrsin and Kistler (1955), Wygnanski and Fiedler (1969) and by many other researchers. Some discrepancies in the measurements at the boundaries of the jet were found due to intermittency.

4.2.1 Turbulence in Submerged Jet Flow

The pattern of mean quantities for shear flows like jets and wakes are well understood. However, the small-scale turbulent fluctuations are yet to be fully understood. As a result of this, several acoustic phenomena associated with jets pose serious challenges to scientists and engineers. One such phenomenon is the acoustic re-excitation of bubbles in the jet (Kolaini, 1993). Experimental data presented by several researchers (Davies et al., 1963; Sami et al., 1967) gave strong support that fluctuating velocity in the longitudinal direction (u') is one order of magnitude higher than those in the transversal directions (v' , w'). Evidence is available that in the zone of flow

establishment, maximum turbulent intensities occur halfway between the center-line and the boundary. The parameter $\sqrt{u'^2}$ is called the turbulent intensity in the longitudinal direction. Similarly turbulent intensities in other directions are also defined. The longitudinal and transversal turbulent intensities at the center-line are very low compared to their respective maximum values which occur midway between the center-line and the boundary. But these center-line intensities continue to increase to about 90% of their maximum values at that cross section as the distance from the nozzle exit increases; thus approaching self-similarity. The average size of the eddies in the center-line increases as the distance from the nozzle exit increases. Sami et al.(1967), Wygnanski and Fiedler (1969) and other researchers have estimated turbulent integral length scales and microscales by spectral analyses of the velocity fluctuations. The discrepancies between different experimental results have not been sufficiently explained.

Townsend (1948), Corrsin (1949) and Laufer (1954) have obtained data that gave credence to statistical isotropy of the small scale turbulence. Verification of the Kolmogorov universal equilibrium theory had been done by Gibson (1963) by analyzing stream-wise and cross-stream-wise turbulent spectrum functions (velocity fluctuations). The order in which self-preservation of various flow parameters occur and the exact mechanisms involved in the self-preservation process have not yet been fully understood.

Chapter 5

CALIBRATION

The experimental facility and techniques used have been described in Chapter 2. This chapter describes the conditions under which the actual experiments were performed, and the data obtained. The calibration and measurements were conducted in the jet at $x/d \cong 10$ and $x/d \cong 20$ locations from the nozzle exit, where d is the diameter of the nozzle. A nozzle of 3.183 mm exit diameter was used for the present study. The symbol " \cong " is used where a volume or a region is implied. The symbol "=" is used where an exact location is implied. Table 5.1 gives details about the grid points used for the calibration process.

TABLE 5.1 Reference grid points used for calibration

	$x/d \cong 10$	$x/d \cong 20$
Grid points / plane	80	162
Number of planes	9	7
Total grid points	720	1134
Test volume (XxYxZ) mm³	14 x 13 x 13	19 x 27 x 19
Spacing of grid points (X, Y, Z) mm	1.573, 1.594, 1.590	1.573, 1.594, 3.175

The data reduction equations (Eqs. (2.1)-(2.4)) relating the world coordinates of the grid points to their image coordinates were solved by the least-squares optimization process. "Modified" camera parameters as explained in Chapter 2, section 2.2, were obtained. Since two equations arise for every point in space in each camera, there are a total of four equations for each point in space (here the reference grid points). Since 720 points were used in the $x/d \cong 10$ case, there were 2880 equations to be solved for the 18 camera parameters, 9 for each camera. Similarly there were 4536 equations to solve for 18 camera parameters in $x/d \cong 20$ location. It should be kept in mind that for each test volume being viewed, the cameras had to be calibrated in this manner. As mentioned in Chapter 2, IMSL subroutine DUNLSJ was used to solve the data reduction equations on

TABLE 5.2 Initial guess and converged ("modified") camera parameters for camera A

S.no	Variables	Guess values	Modified values
1	X_{OA}	187.54 mm	116.74 mm
2	Y_{OA}	15.25 mm	11.41 mm
3	Z_{OA}	-620 mm	-666.74 mm
4	ω_A	0	0.44×10^{-2} radians
5	ϕ_A	-0.294 radians	-0.2354 radians
6	ψ_A	0	-0.022 radians
7	f_a	350 mm	340.56 mm
8	x_{app}	0	-21.32 mm
9	y_{app}	0	3.68 mm

the basis of unconstrained optimization. Table 5.2 shows the values of the initial guesses provided (measured camera parameters) for calibration at $x/d \cong 10$ location, and the solutions to the equations ("modified" camera parameters) for camera A. Table 5.3 shows the values for camera B.

As explained in Chapter 2, section 2.2, the "error file" containing the predicted world coordinates of the grid points and their bias errors due to refraction and other effects were obtained. Particle positions as predicted by the "modified" camera parameters were also obtained. As mentioned in Chapter 2, an interpolation scheme was used to interpolate the bias errors from the grid points on to the particle positions to get their world coordinates (actual X, Y, Z positions in space).

TABLE 5.3 Initial guess and converged ("modified") camera parameters for camera B

S.no	Variables	Guess values	Modified values
1	X_{OB}	-242.55 mm	-170.25 mm
2	Y_{OB}	-7.62 mm	-7.39mm
3	Z_{OB}	-625 mm	-693.34 mm
4	ω_B	0	-0.94×10^{-2} radians
5	ϕ_B	0.37 radians	0.3063 radians
6	ψ_B	0	0.0188 radians
7	f_b	350 mm	362.17 mm
8	$x_{b_{pp}}$	0	23.72 mm
9	$y_{b_{pp}}$	0	-0.904 mm

TABLE 5.4 RMS errors in calibration

Coordinate	Root Mean Square Errors mm	
	Multiquadric Interpolator	Cubic Spline
X	0.016	6.81×10^{-5}
Y	0.013	5.84×10^{-5}
Z	0.071	1.73×10^{-4}

Two interpolators were tested for this purpose. Alternate grid points with their bias errors were kept as the source file; the interpolators were used to interpolate on to the predicted positions of the other grid points (referred to as "check points"). The results of this interpolation were compared with the measured world (space) coordinates of the "check" points. The root mean square (RMS) of the deviations between these points were found out for X, Y and Z positions. The interpolator which yielded the least RMS errors was selected.

The multiquadric interpolator and cubic spline interpolation scheme using Akima's method were the two interpolation schemes tried. The multiquadric technique was considered because of its highly satisfactory performance in the 2-D rotating flows (Kuhlman, 1990; Abrahamson et. al., 1988). The Cubic spline interpolator was considered because it creates a smoother interpolant in univariate problems. The description of multiquadric interpolator is given in Chapter 6. The results tabulated in Table 5.4 show the relative performances of the two interpolators; these values were taken from the $x/d \cong 20$ case.

As shown above, the cubic spline interpolation scheme gave better results than the multiquadric interpolator and was chosen for the bias error interpolation on to the particle positions. These RMS errors are estimates of uncertainties involved in determining the positions of particles/grid points by the calibration procedure.

Chapter 6

RESULTS AND DISCUSSIONS

6.1 INTRODUCTION

As described in Chapter 3, the particles were matched and tracked automatically and particle positions at 100 consecutive time steps were obtained. The images were taken at 2000 frames per second for the $x/d \cong 10$ case and at 1000 frames per second for the $x/d \cong 20$ case. Hence the total interval times corresponding to 100 time steps were 50 and 100 milliseconds respectively. Instantaneous velocities in all three directions were calculated based on the particle positions in pairs of consecutive data sets representing consecutive time steps. Turbulent parameters, such as the Reynolds stresses were calculated based on the fluctuating components of velocities. Vorticities were calculated in all three directions based on the velocity gradients. Turbulent length scales were calculated. All these quantities were compared with the existing experimental results for submerged jets.

6.2 VELOCITIES AND TURBULENT PARAMETERS

The coordinate system and the jet are shown in Fig. 6.1. The notations as defined in Chapter 3 are again briefly mentioned here.

The parameters $x_a(i)$, $y_a(i)$ are the coordinates of the particle position in image A at time step 1; $x_b(i)$, $y_b(i)$ are the coordinates of the matching particle position in image B at time step 1; $x_{a2}(i)$, $y_{a2}(i)$ are the coordinates of the corresponding particle position in image A

at time step 2; and $x_{b2(i)}$, $y_{b2(i)}$ are the coordinates of the corresponding particle position in image B at time step 2. As described in Chapter 3, these four quantities were obtained from automatic particle matching and tracking routines.

The image coordinates $x_{a(i)}$, $y_{a(i)}$ combined with $x_{b(i)}$, $y_{b(i)}$ were used to calculate the world coordinates (say, x_1 , y_1 , z_1) of the point in space by means of data reduction equations (Eqs. (2.1)-(2.4)). Similarly, $x_{a2(i)}$, $y_{a2(i)}$ combined with $x_{b2(i)}$, $y_{b2(i)}$ were used to find the world coordinates of the same particle at the next time step (say, x_2 , y_2 , z_2). The velocities in three directions were then calculated as follows

$$u = \frac{x_2 - x_1}{\Delta t}; \quad v = \frac{y_2 - y_1}{\Delta t}; \quad w = \frac{z_2 - z_1}{\Delta t}. \quad (6.1)$$

The velocity vector at any instant is given by

$$\tilde{V} = u\hat{i} + v\hat{j} + w\hat{k} \quad \text{where} \quad \tilde{V}(x, y, z, t) = \bar{V}(x, y, z) + V'(x, y, z, t), \quad (6.2)$$

where $x = (x_1 + x_2)/2$, $y = (y_1 + y_2)/2$, $z = (z_1 + z_2)/2$,

$$\text{and } \bar{V} = \frac{1}{T} \int_0^T \tilde{V} dt = \frac{1}{n\Delta t} \sum_{i=1}^n \tilde{V} \Delta t, \quad (6.3)$$

where n is the number of time steps, T is the averaging time.

6.2.1 Mean Velocities

As mentioned earlier, velocity data for 100 time steps (n) were averaged and the averaging time (T) is 50 ms for the $x/d \cong 10$ case and 100 ms for the $x/d \cong 20$ case. As mentioned in Chapter 5, The symbol " \cong " is used where a volume or a region is implied.

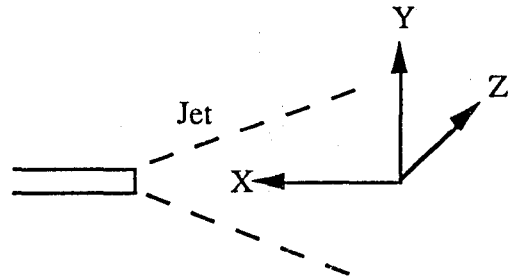


Fig. 6.1. Coordinate system and the jet.

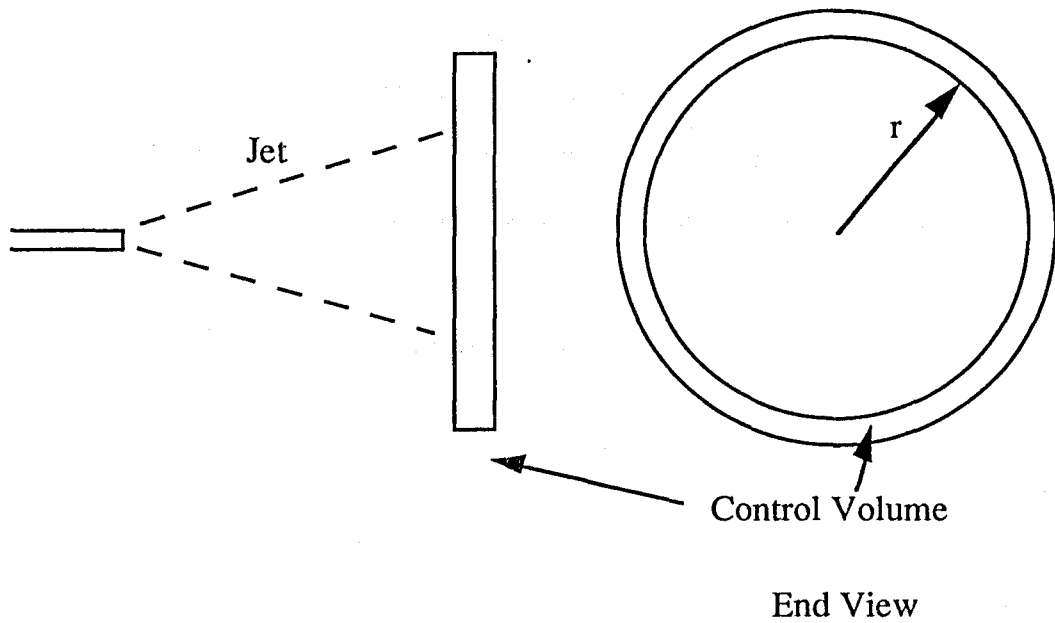


Fig. 6.2. Control volume for velocity vector averaging.

The symbol "=" is used where an exact location is implied. A problem faced in evaluating the summation in Eq. (6.3) is that the velocities \tilde{V} are not available at the same location (X, Y, Z position) at different times. This is because the data are available only where the seeding particles happen to be, and the particles tend to be randomly distributed. One method of dealing with this situation is to interpolate the velocities at each time step on to a set of fixed grid points. The summation in Eq. (6.3) can then be performed at each grid point.

This procedure was attempted at first, using the multiquadric interpolator. However, the density of the data at each time step was not high enough to resolve the smaller eddies present in the flow. Around 50 to 70 unevenly spaced velocity vectors were obtained each time. Therefore, the interpolator tended to smooth out spatial features which it could not resolve. While the magnitude of the resolution could not be estimated correctly, it was clear that the spatial resolution of the data at each time step was significantly lower than the temporal resolution of 0.5 to 1 ms. Hence a pooling method was adopted which improved the spatial resolution at the expense of worsening the temporal resolution. Also it was believed that the use of an interpolator would lead to misinterpreting the data.

The pooling procedure followed involved dividing the measurement volume into a number of smaller control volumes such as the annular control volume shown in Fig. 6.2. Both rectangular and annular control volumes were used. A control volume of 2 mm^3 was "traversed" across the jet. This was to simulate measurements with a hot-wire probe. Also, as shown in Fig. 6.2, annular control volumes were used to obtain the data at axisymmetric points across the jet. This method facilitated comparison of the present results with those obtained from previous investigations with hot-wires. Equation (6.3)

was used to average velocity vectors for each control volume. This procedure involved implicit spatial interpolation, since the mean and fluctuating velocity values (\bar{u} , u' , etc.) were assigned to the centroids of rectangular volumes or the average radius of the rings. Plots of mean velocity profiles across the jet at $x/d=12$ are shown in Fig. 6.3. As seen in Fig. 6.3, \bar{u} is much higher than \bar{v} and \bar{w} . The same was observed in the previous experiments with submerged jets (Sami et. al., 1967; Wygnanski and Fiedler, 1969). However the gradient of \bar{u} is not smooth. This can be attributed to the flow establishment in this region and a relatively short averaging time (50 millisecond) of velocity data. Typical hot-film data tend to be averaged over longer time periods so as to smooth out the slowest fluctuations. Similar trends were observed in the mean velocity profiles at $x/d=22$. These are shown in the Fig. 6.4, along with the Görtler type analytical solution for the mean axial velocities. The agreement was found to be satisfactory in the inner region. Some discrepancy is seen in the other regions. The gradients of \bar{u} are lower, which indicate that the flow has proceeded further towards self preservation. All mean velocities are non-dimensionalized with U_m , the velocity at the jet center-line at the respective x location. The magnitudes of the velocities at the jet center-line was compared with the ones calculated based on an empirical relation. Wygnanski and Fiedler (1969) used the empirical relation $U_m/U_o = 5.4/(x/d)$ to calculate the center-line velocity where U_m is the center-line velocity; U_o is the mean exit velocity of the jet; x is the distance from the nozzle exit, and d is the diameter of the jet orifice. Based on this relationship, the maximum velocities at the jet center-line were found to be 1127 mm/sec and 614 mm/sec at $x/d=12$ and 22 respectively. The experimental values for the same locations were found to be 1124 mm/sec and 575 mm/sec respectively. Thus the center-line velocities were found to be in good agreement with the existing experimental results.

6.2.2 Fluctuating Velocity Components

After calculating the mean velocity via Eq. (6.3), the fluctuating components of velocities were obtained from

$$V'(x, y, z, t) = \tilde{V}(x, y, z, t) - \bar{V}(x, y, z). \quad (6.4)$$

The non-dimensionalized fluctuating components of velocities $\sqrt{u'^2}/U_m$, $\sqrt{v'^2}/U_m$ and $\sqrt{w'^2}/U_m$ at $x/d=12$ are shown in Fig. 6.5. The velocity data distribution across the flow where these parameters were measured is shown in Fig. 6.6. Since the fraction of time the velocity vectors are available near the center-line of the jet and at the boundaries is very low, the values of the fluctuating velocities in those locations were found to be unreliable; therefore they were dropped. Fluctuating velocities in the longitudinal direction steadily increase away from the boundary and decrease slightly near the axis of the jet.

The transversal fluctuating velocity v' is a maximum at about 1/2 diameter from the axis of the jet and a minimum at the boundaries. The other transversal component w' does not seem to have a discernible trend but seems to have magnitudes higher than u' and v' . Since the jet was axisymmetric, v' and w' values should have been similar. The large w' values can be attributed to the errors associated in finding the positions of particles in the depth direction. The causes of these errors are discussed in detail in the next chapter. Nonetheless, it has to be borne in mind that an incorporation of w' in the measurement scheme helps reduce the errors in u' and v' (i.e. if a 2-D method was employed, errors in u' and v' would have been higher). Since particle movements as recorded in the images consisted of combinations of in-plane (X and Y) and out-of-plane

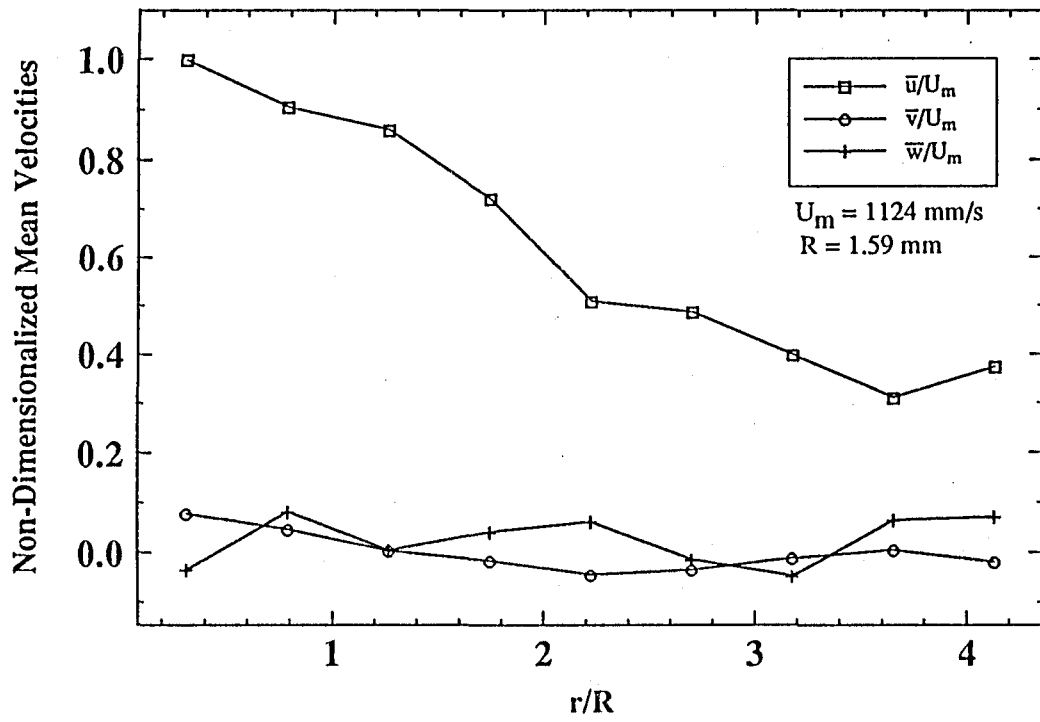


Fig. 6.3. Plot of mean velocities at $x/d=12$.

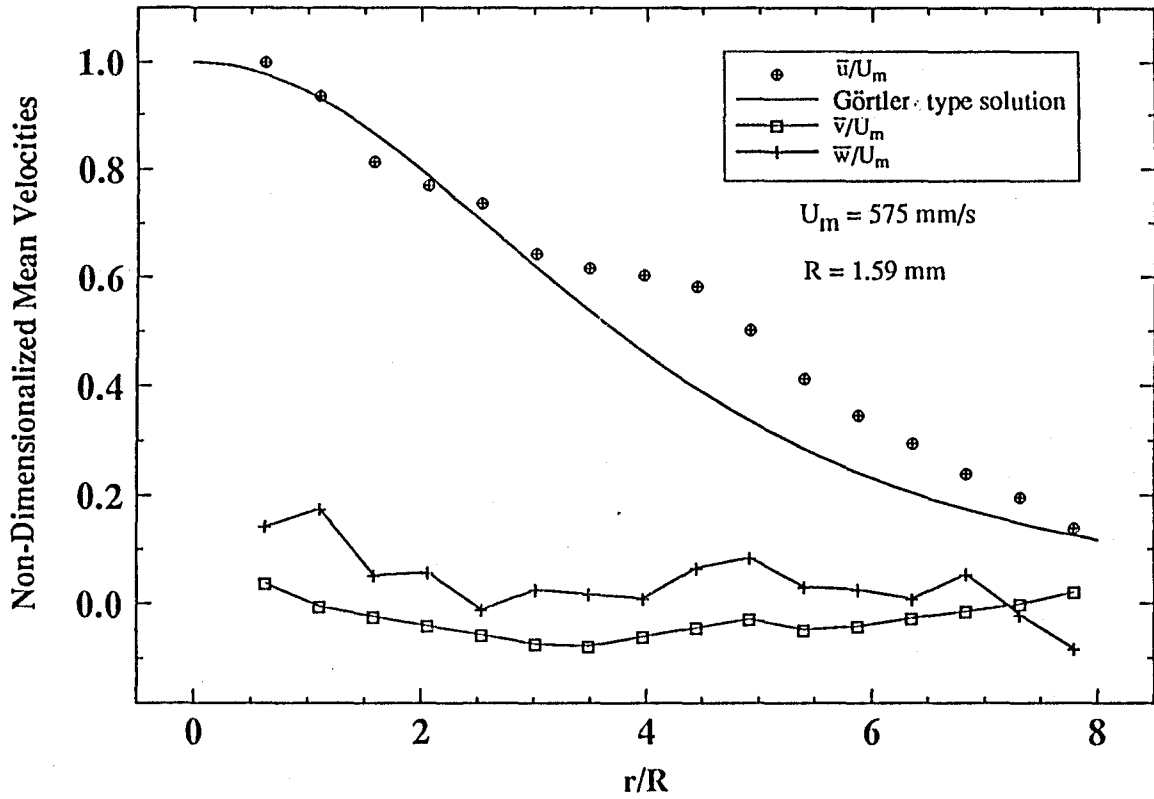


Fig. 6.4. Plot of mean velocities at $x/d=22$.

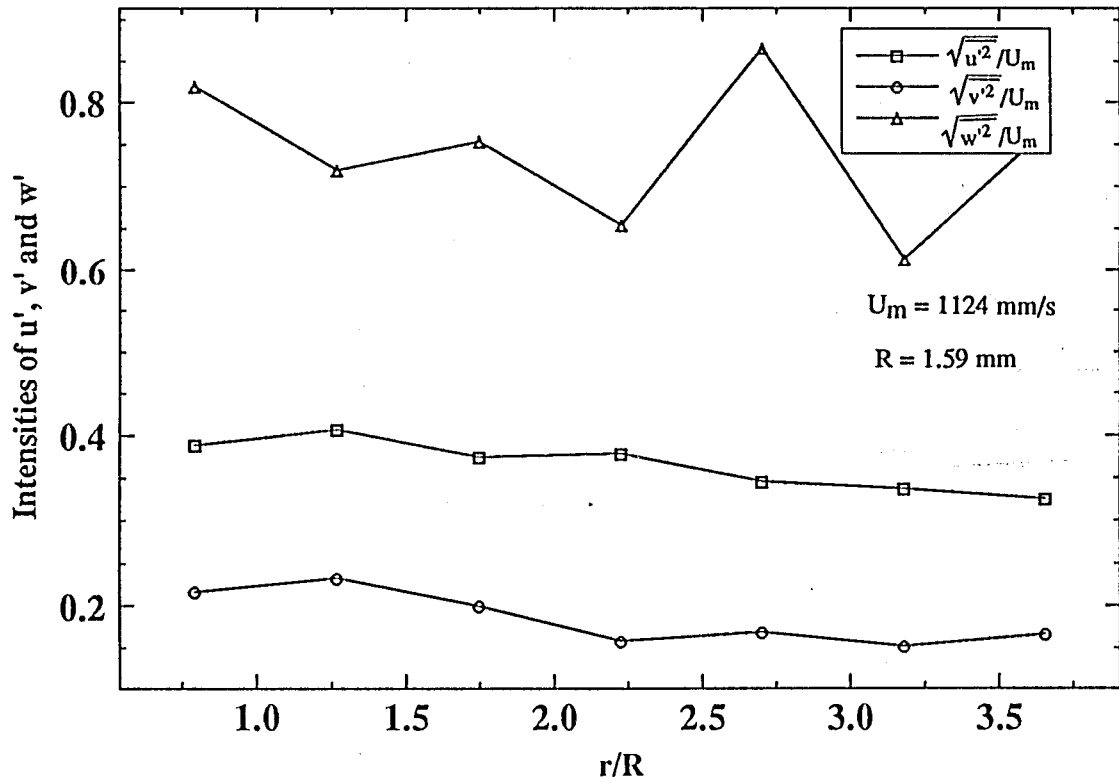


Fig. 6.5. Plot of fluctuating velocities at $x/d=12$.

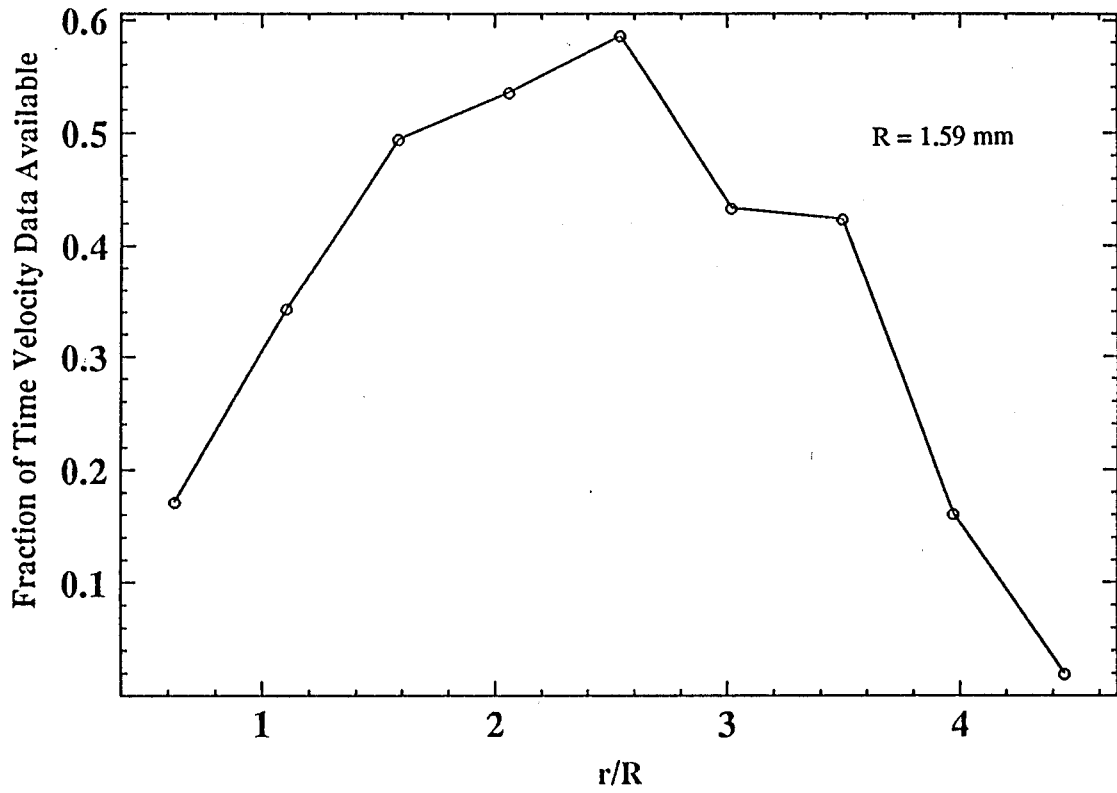


Fig. 6.6. Plot of velocity data distribution across the jet at $x/d=12$.

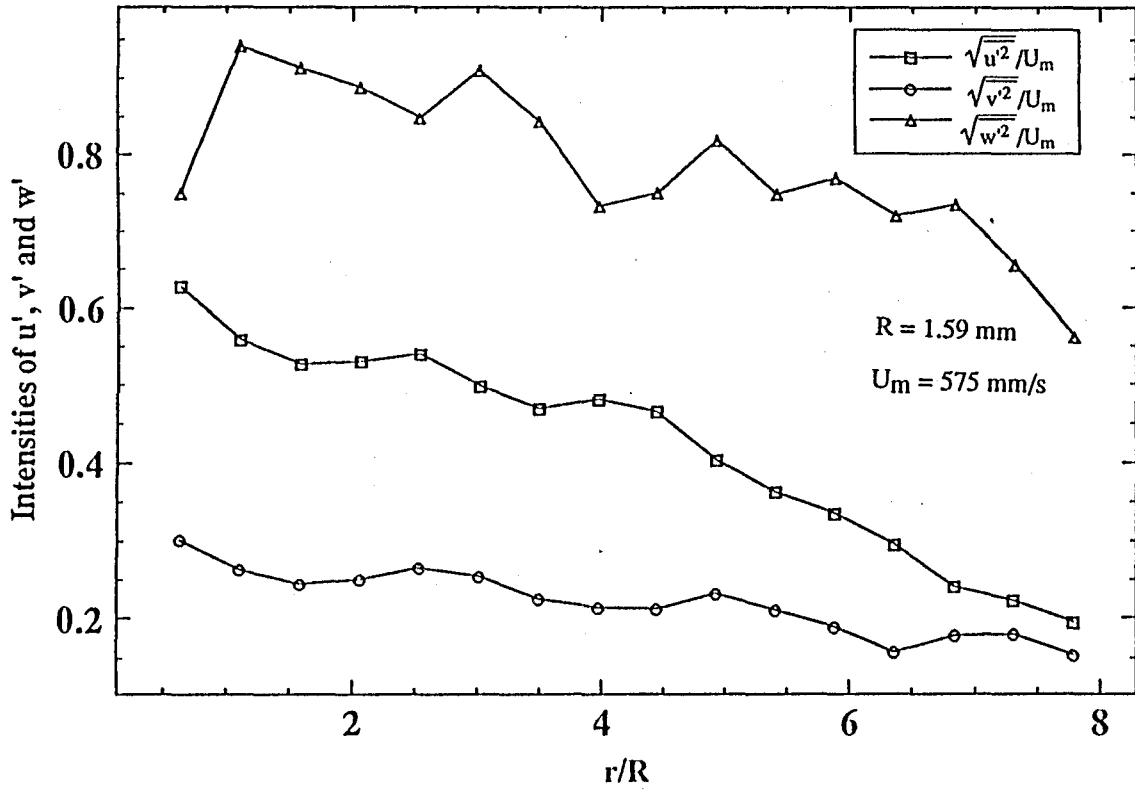


Fig. 6.7. Plot of fluctuating velocities at $x/d=22$.

or depth (Z) movements, the separation of Z movement for the purpose of calculating w' has reduced the errors in X and Y movements. The fluctuating components of velocities for $x/d=22$ are shown in Fig. 6.7. The quantity $\sqrt{u'^2}$ increases from a minimum at the boundary to a maximum at the jet center-line. A similar trend is observed for $\sqrt{v'^2}$ as well. This showed that the jet attained self-similar conditions with respect to the velocity fluctuations at this axial location. Once again, $\sqrt{w'^2}$ appeared to have higher magnitudes than $\sqrt{u'^2}$ and $\sqrt{v'^2}$.

6.2.3 Reynolds Stresses

Denoting the fluctuating velocity vector as $V'(x, y, z, t) = \tilde{V}' = u'\hat{i} + v'\hat{j} + w'\hat{k}$ the Reynolds stress tensor component $\overline{u'v'}$ was calculated as

$$\overline{u'v'} = \frac{1}{n} \sum_{i=1}^n u'_i(x, y, z, i\Delta t) v'_i(x, y, z, i\Delta t) \quad (6.5)$$

Similarly other components of the Reynolds stress tensor $\overline{u'^2}$, $\overline{v'^2}$, $\overline{w'^2}$, $\overline{v'w'}$, $\overline{w'u'}$ were determined. Values of these are shown in Figs. 6.8 and 6.9. It is difficult to deduce a clear trend in these quantities. However they can be seen to have the same order of magnitude. This is true at both $x/d=12$ and 22 locations. A thin plane-strip covering the entire YZ plane (perpendicular to the axis of the jet) in the center of the jet and having a thickness of 4 mm in X (axial direction) was selected. Instantaneous velocity vectors for 100 time steps within this strip were pooled. Rectangular control volumes of 2mm x 2mm x 2mm were used to determine the values of \bar{u} , u' and $u'v'$. These values were interpolated onto a finer grid using the multiquadric interpolator. The use of a

multiquadric interpolator is explained in the following section. The 3-D plot of the axial mean velocity \bar{u} is shown in Fig. 6.10. Figures 6.11 and 6.12 depict 3-D plots of the quantities u' and $u'v'$ in dimensionless form at $x/d=22$ location.

6.3 VORTICITY

A thin plane-strip covering the entire XY plane (parallel to the axis of the jet) in the center of the jet and having a thickness of 4 mm in Z (depth) was selected for vorticity estimates. Although the entire measurement volume could have been used, errors in the velocity data (as seen in the w' estimates) would result in large errors in the vorticities. A thin central plane on the other hand would provide an insight into interesting vortical structures without obscuring the results. Instantaneous velocity vectors at 100 time steps within the control volume were pooled for this purpose. Using the unevenly spaced instantaneous vectors found in the thin strip, spatial derivatives $\frac{\partial u}{\partial z}$, $\frac{\partial u}{\partial y}$, $\frac{\partial v}{\partial x}$, $\frac{\partial v}{\partial z}$, $\frac{\partial w}{\partial y}$ and $\frac{\partial w}{\partial x}$ were computed at regular grid nodes using the multiquadric interpolator. All velocity

vectors are assumed to be at the same time instant. The multiquadric interpolator was used to interpolate the velocities one component at a time. These interpolated velocity components u , v , w were calculated as follows:

$$u = C_{i,u}[(x_i - x_j)^2 + (y_i - y_j)^2 + (z_i - z_j)^2 + R^2]^{-\left(\frac{m}{2}\right)}, \quad (6.6)$$

$$v = C_{i,v}[(x_i - x_j)^2 + (y_i - y_j)^2 + (z_i - z_j)^2 + R^2]^{-\left(\frac{m}{2}\right)}, \text{ and} \quad (6.7)$$

$$w = C_{i,w}[(x_i - x_j)^2 + (y_i - y_j)^2 + (z_i - z_j)^2 + R^2]^{-\left(\frac{m}{2}\right)}, \quad (6.8)$$

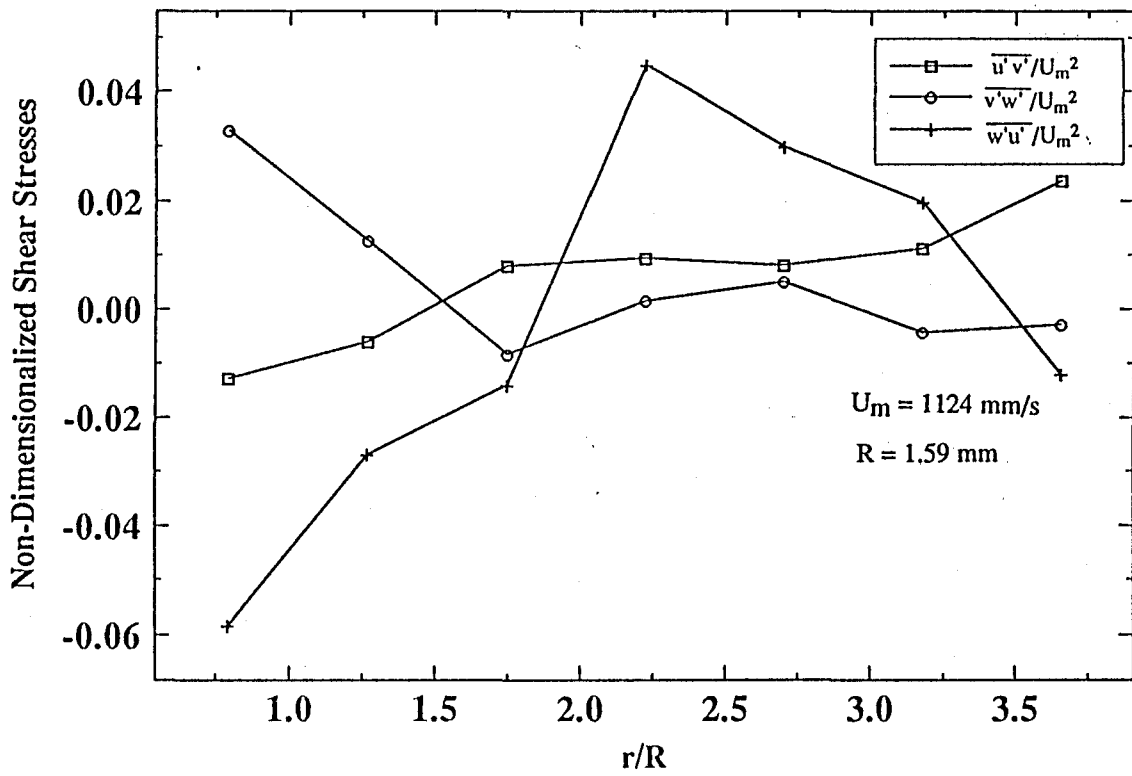


Fig. 6.8. Plot of turbulent shear stresses at $x/d=12$.

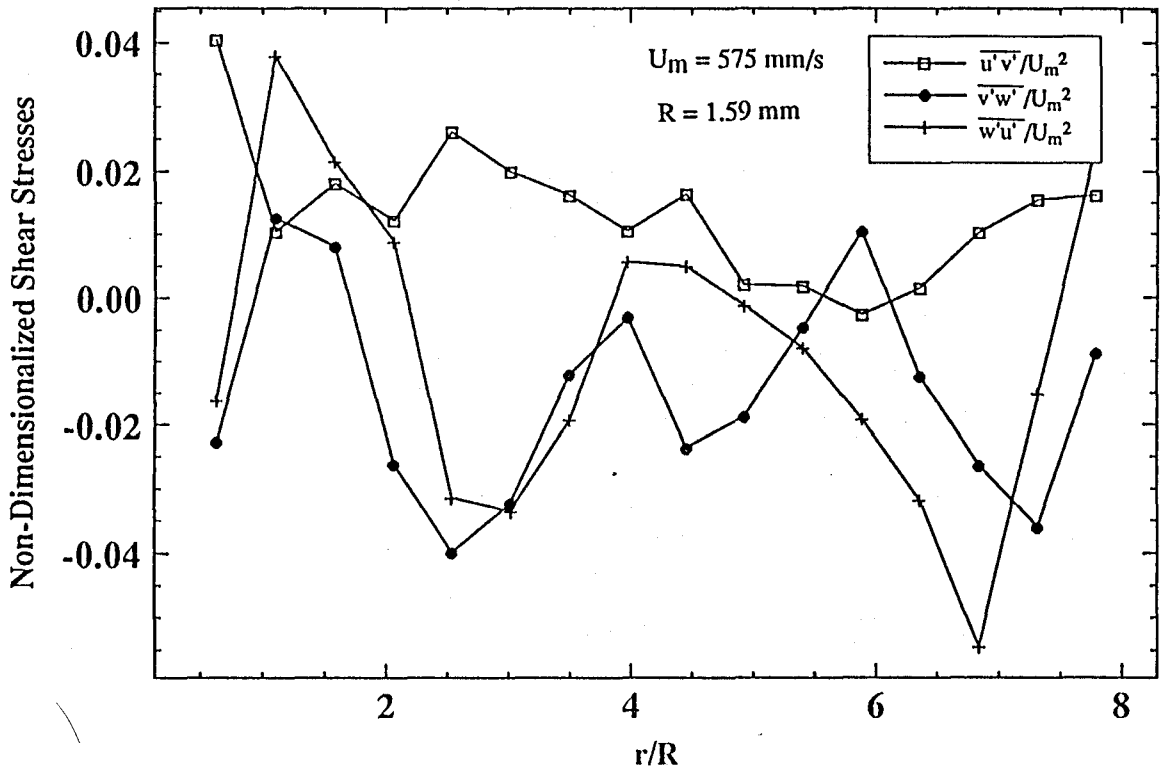


Fig. 6.9. Plot of turbulent shear stresses at $x/d=22$.

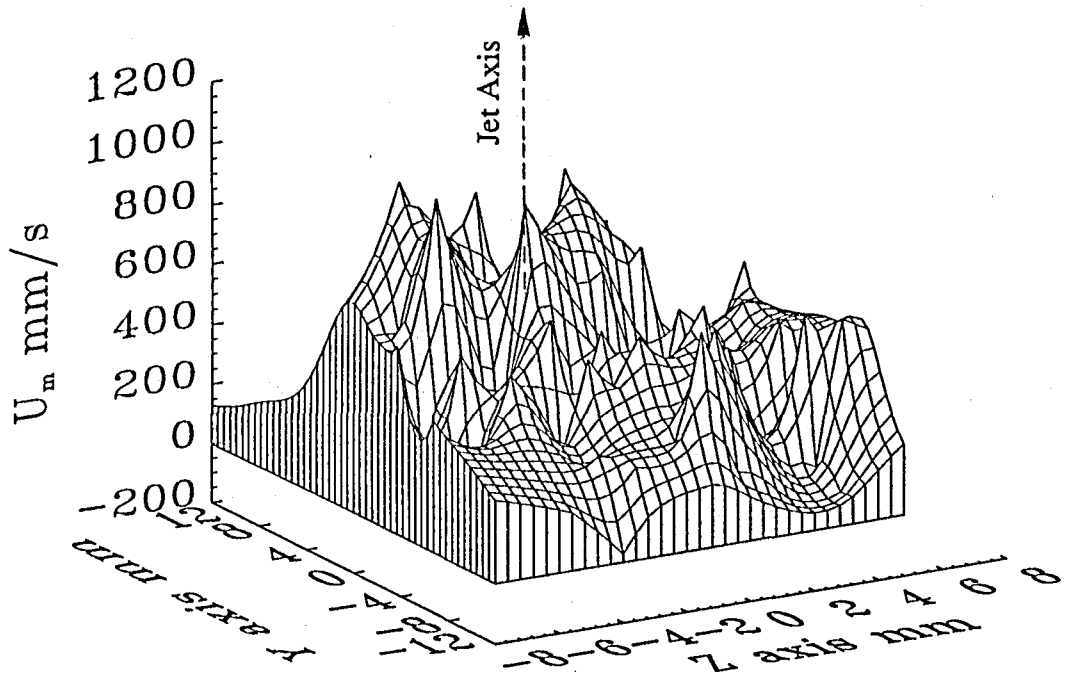


Fig. 6.10. 3-D plot of axial velocity at $x/d=22$.

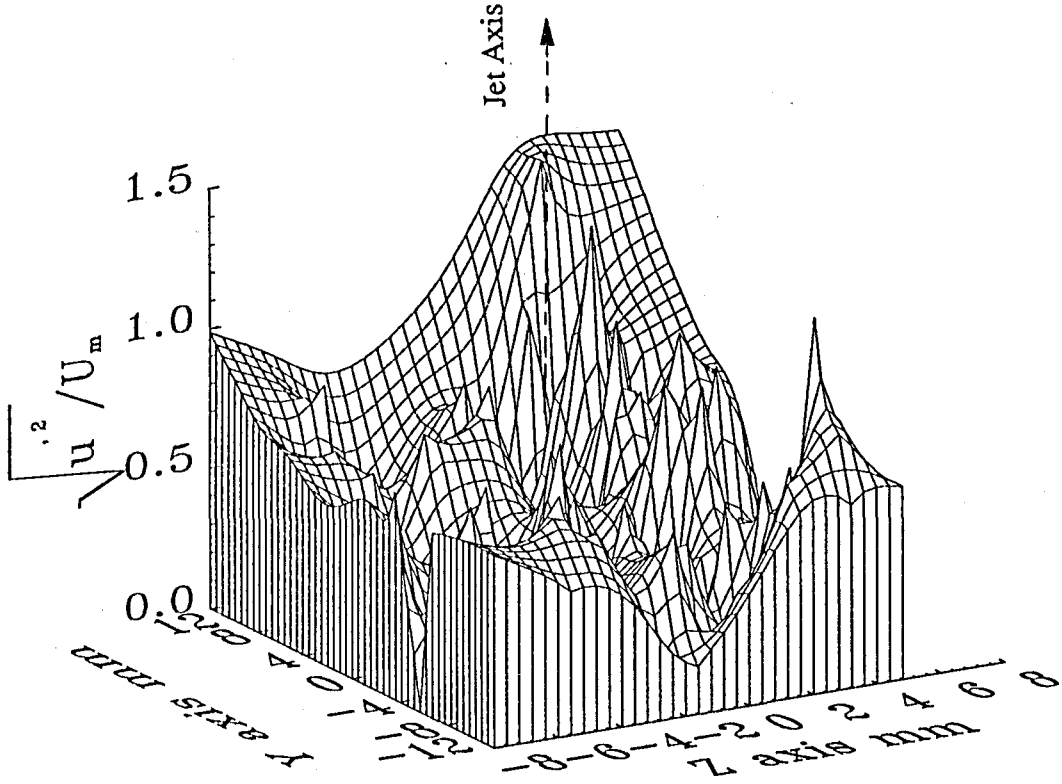
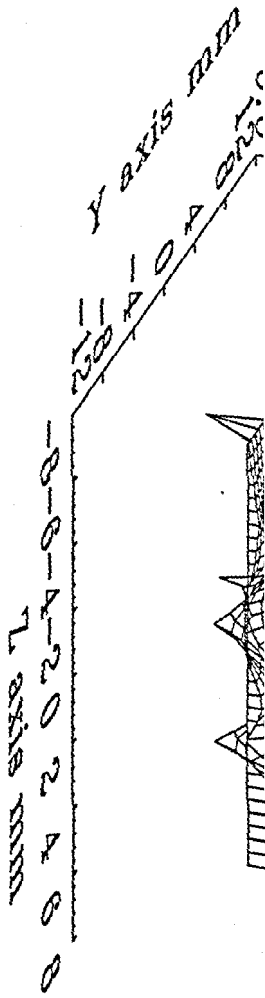
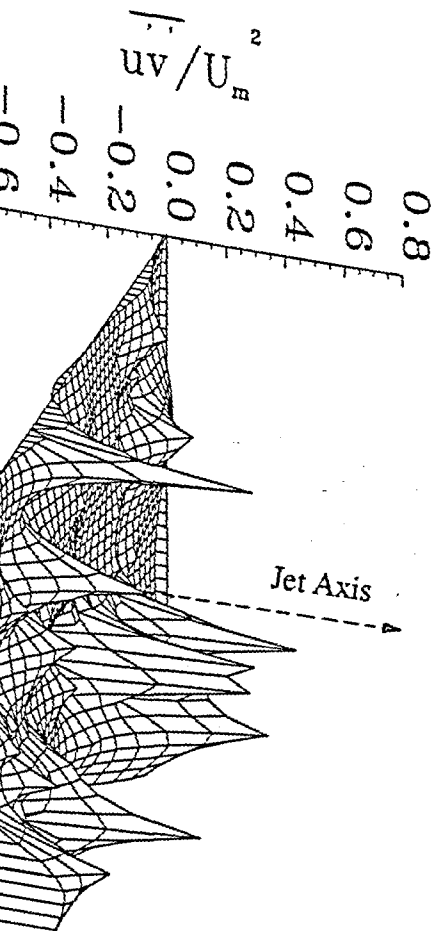


Fig. 6.11. 3-D plot of tangential fluctuating velocity at $x/d=22$.

Fig. 6.12. 3-D plot of shear stresses in X-Y plane at $x/d=22$.





where R is known as the spatial averaging parameter and m is the filter shape factor. Parameters R and m are variable parameters of the interpolation scheme which can be set by the user. The positions (x_i, y_i, z_i) are the locations of data points and (x_j, y_j, z_j) are the locations of grid nodes; C_i is the vector of reconstruction coefficients for the scalar field being interpolated. Spatial derivatives of the velocities were computed by differentiating Eqs. (6.6), (6.7) and (6.8) with respect to x , y and z to obtain relevant terms for vorticity calculations. For example

$$\frac{\partial u}{\partial y} = C_{i,u} m (y_i - y_j) [(x_i - x_j)^2 + (y_i - y_j)^2 + (z_i - z_j)^2 + R^2]^{-\frac{(m+1)}{2}}, \quad (6.9)$$

$$\frac{\partial v}{\partial x} = C_{i,v} m (x_i - x_j) [(x_i - x_j)^2 + (y_i - y_j)^2 + (z_i - z_j)^2 + R^2]^{-\frac{(m+1)}{2}}, \quad (6.10)$$

and so on. Vorticities in X , Y , and Z directions were calculated as:

$$\Omega_x = \frac{\partial w}{\partial y} - \frac{\partial v}{\partial z}; \quad \Omega_y = \frac{\partial u}{\partial z} - \frac{\partial w}{\partial x}; \quad \Omega_z = \frac{\partial v}{\partial x} - \frac{\partial u}{\partial y}. \quad (6.11)$$

A complete description of the use of multiquadric interpolator for calculating the vorticity field can be found in the M.S thesis by Kuhlman (1990) and in the paper by Sinha and Kuhlman (1992).

Contour plots of the vorticity components Ω_x , Ω_y , and Ω_z are shown in Figs. 6.13, 6.14 and 6.15 ($x/d \cong 12$ location). Figures 6.16a and 6.16b show vorticity contour plots of Ω_z showing iso-vorticity lines at levels ranging from $-750s^{-1}$ to $1000s^{-1}$. The jet flow

being investigated here is a shear flow hence $\bar{u} \gg \bar{v}$ and \bar{w} , as was shown earlier in the chapter. Performing an order of magnitude analysis (Tennekes and Lumley, 1972), it can be deduced that $\frac{\partial w}{\partial y} \approx \frac{\partial v}{\partial z}$. This indicates the magnitude of Ω_x should be significantly

lower compared to the vorticity components in the other two directions. This can be seen from Figs. 6.13, 6.14, and 6.15. It can also be deduced that due to axisymmetry $\frac{\partial u}{\partial z} \approx \frac{\partial u}{\partial y}$ and $\frac{\partial w}{\partial x} \ll \frac{\partial u}{\partial z}, \frac{\partial v}{\partial x} \ll \frac{\partial u}{\partial y}$. These indicate Ω_y and Ω_z must be of the same order of

magnitude which is verified by Figs. 6.14 and 6.15. These (Ω_y, Ω_z) are also seen to be one order of magnitude higher than that of Ω_x .

In Figs. 6.16a and 6.16b, different sizes of vortical structures of vorticities ranging from $-750s^{-1}$ to $1000s^{-1}$ can be seen. The limits were chosen to encompass all levels of vorticities that occur in the flow within the integration time considered. Figures 6.17, 6.18 and 6.19 show the vorticity contours at $x/d \cong 20$ location. These plots also verify the conclusions of the order of magnitude analysis explained earlier. The contours of Ω_z vorticity plotted in levels ranging from $-750s^{-1}$ to $1000s^{-1}$ are shown in Figs. 6.20a and 6.20b. The vortices seem to have uniform shapes and sizes compared to the vortices of irregular shapes and sizes at $x/d \cong 10$ location. The mean spacing between the vortices (λ) for different vorticity values were estimated from the vorticity contour plots and are tabulated in Table 6.1.

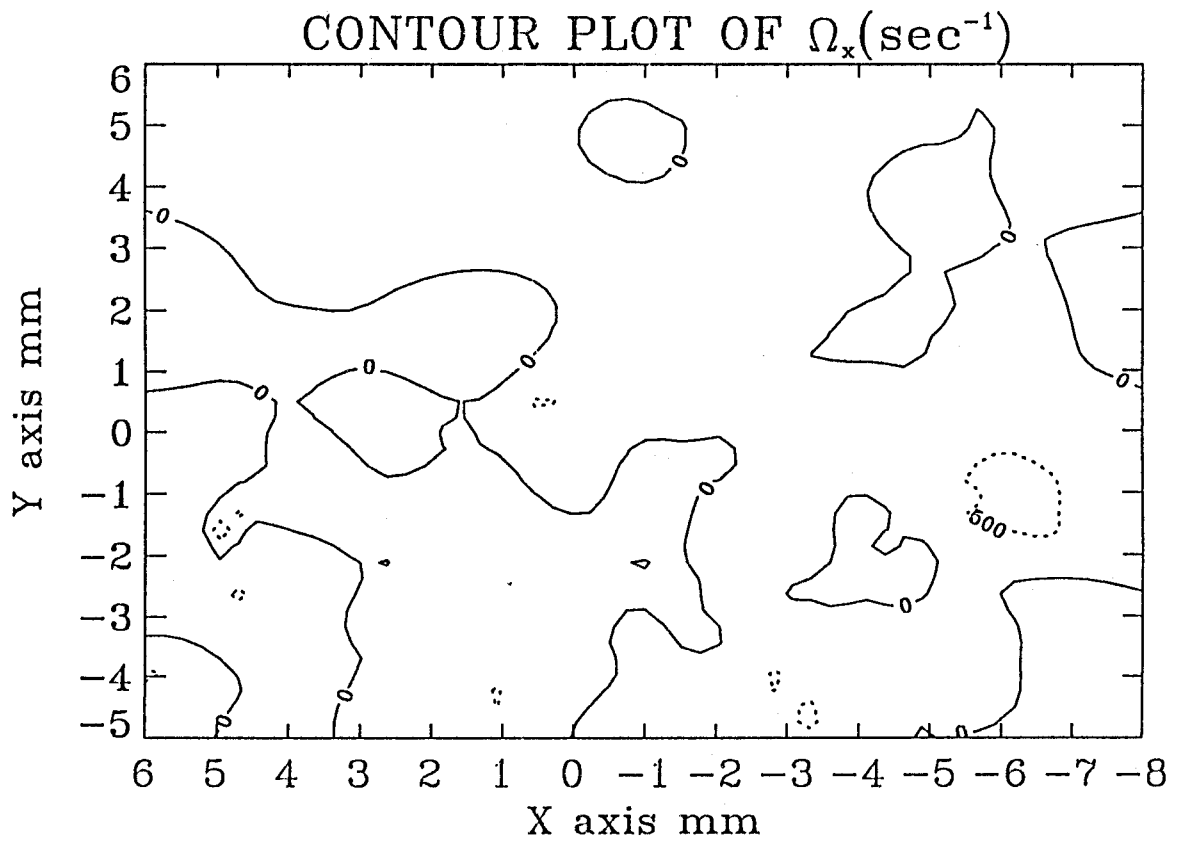


Fig. 6.13. Contour plot of vorticities in X-direction at $x/d \cong 10$.

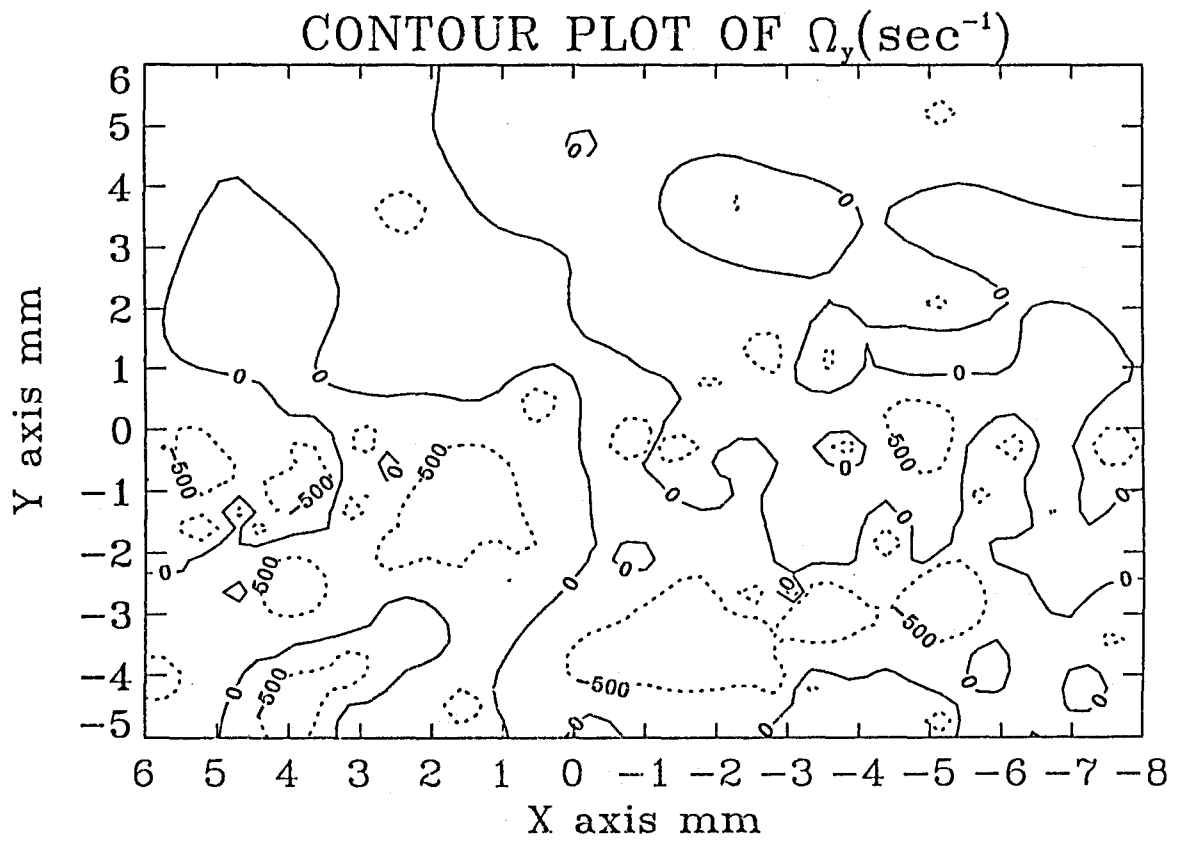


Fig. 6.14. Contour plot of vorticities in Y-direction at $x/d \cong 10$.

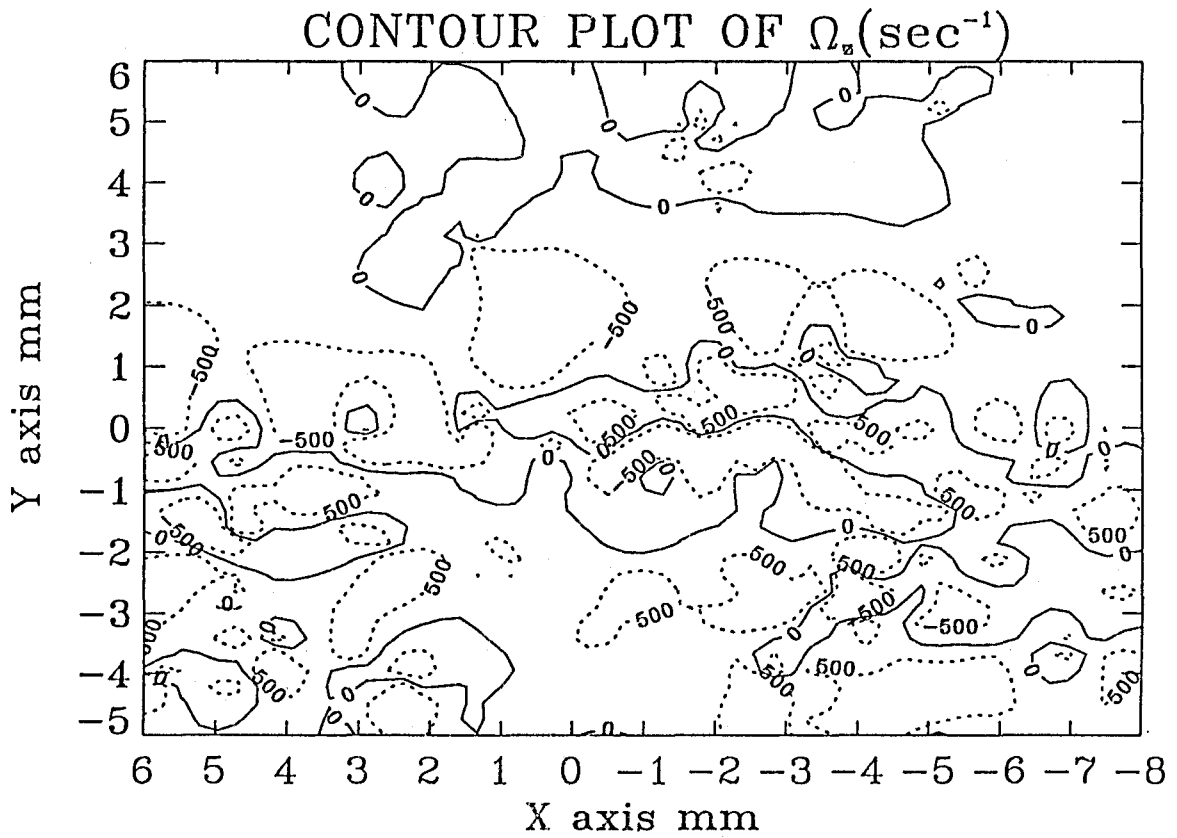


Fig. 6.15. Contour plots of vorticities in Z-direction at $x/d \cong 10$.

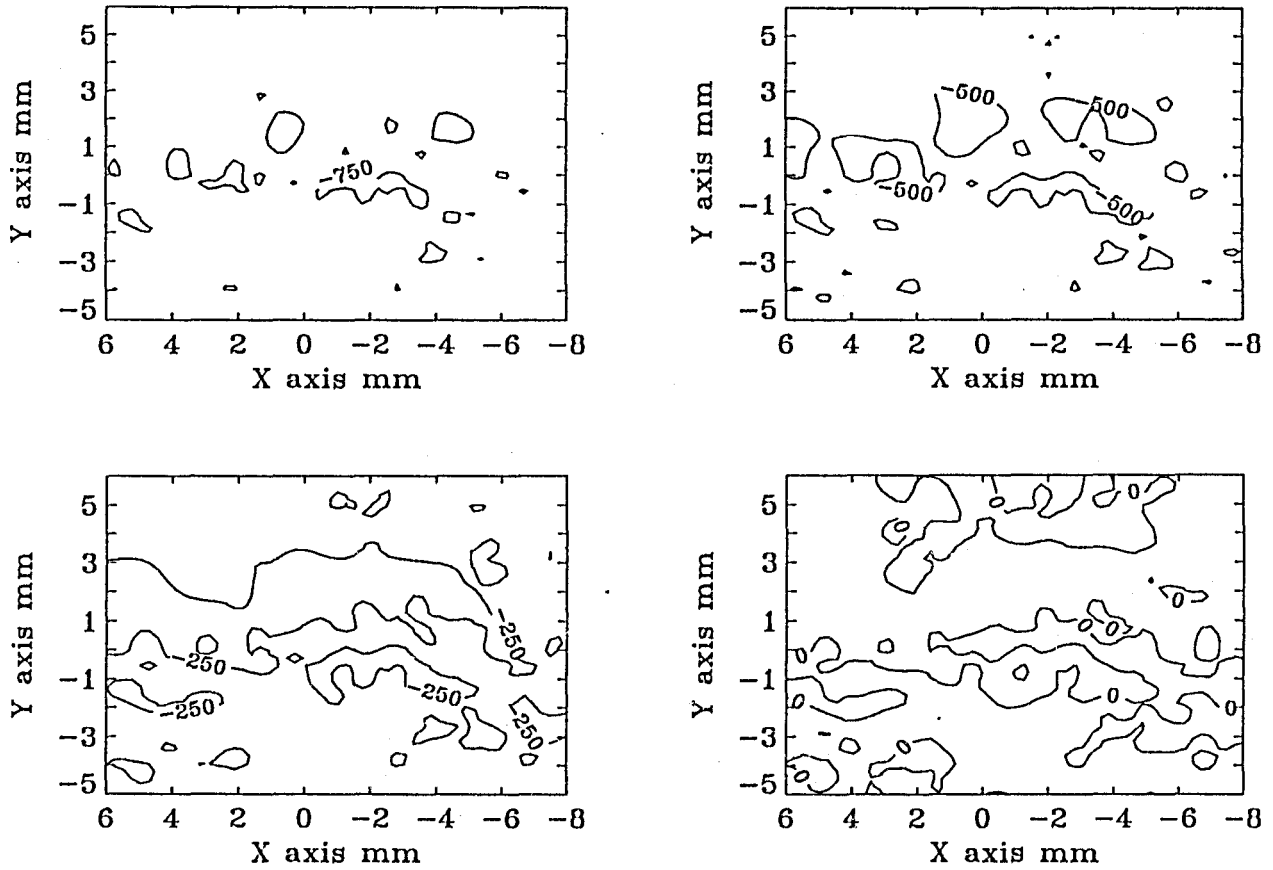


Fig. 6.16a. Contour plot of vorticities in Z-direction in levels -750s^{-1} , -500s^{-1} , -250s^{-1} , and 0s^{-1} at $x/d=10$.

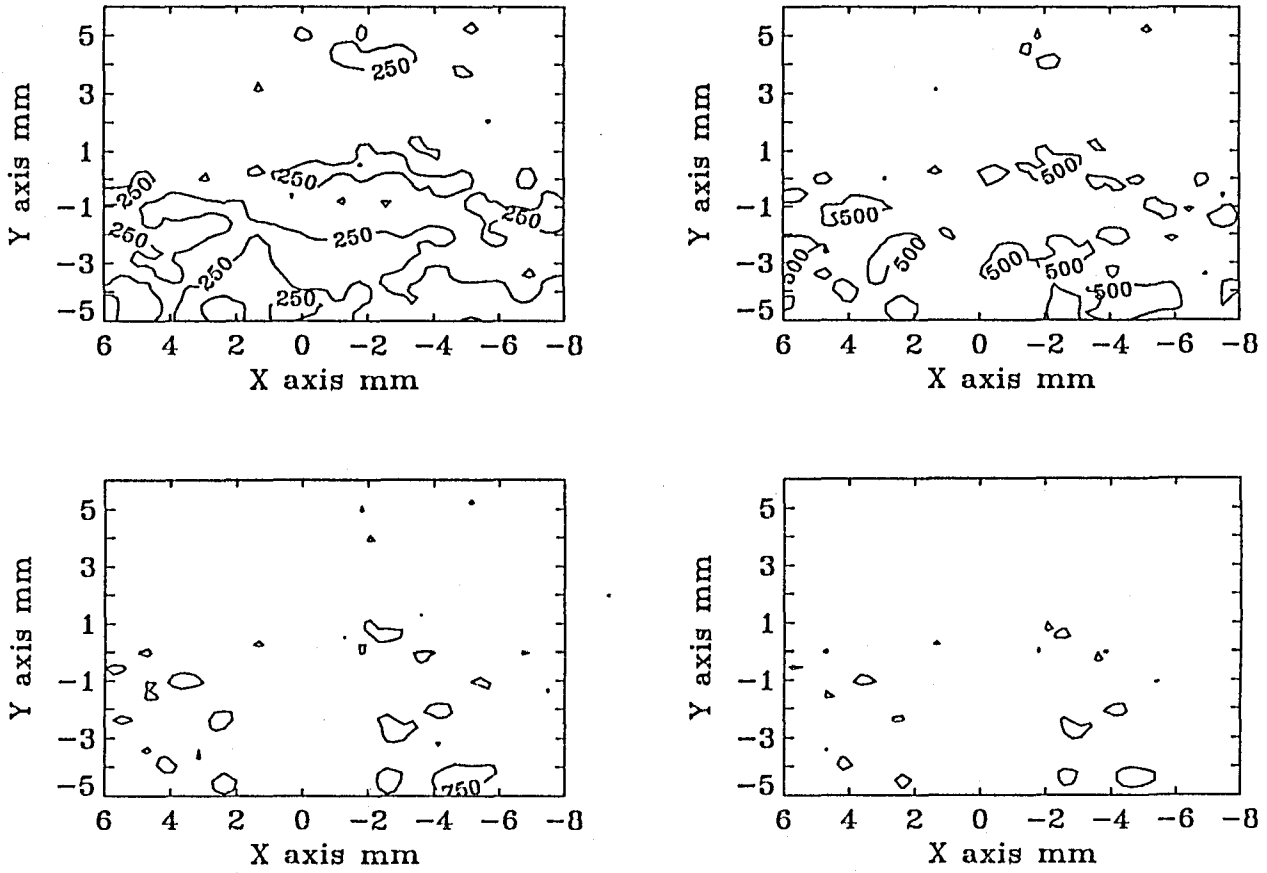


Fig. 6.16b. Contour plot of vorticities in Z-direction in levels 250s^{-1} , 500s^{-1} , 750s^{-1} , and 1000s^{-1} at $x/d=10$.

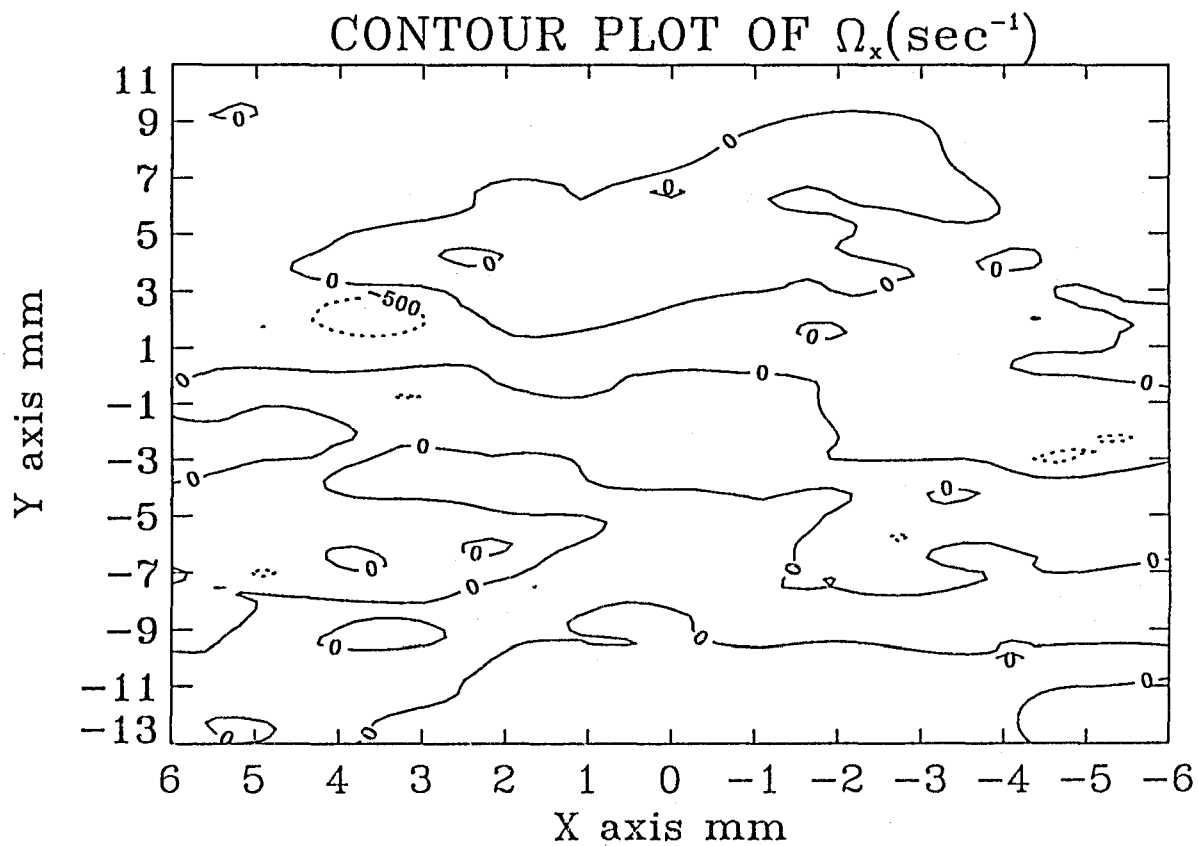


Fig. 6.17. Contour plot of vorticities in X-direction at $x/d \cong 20$.

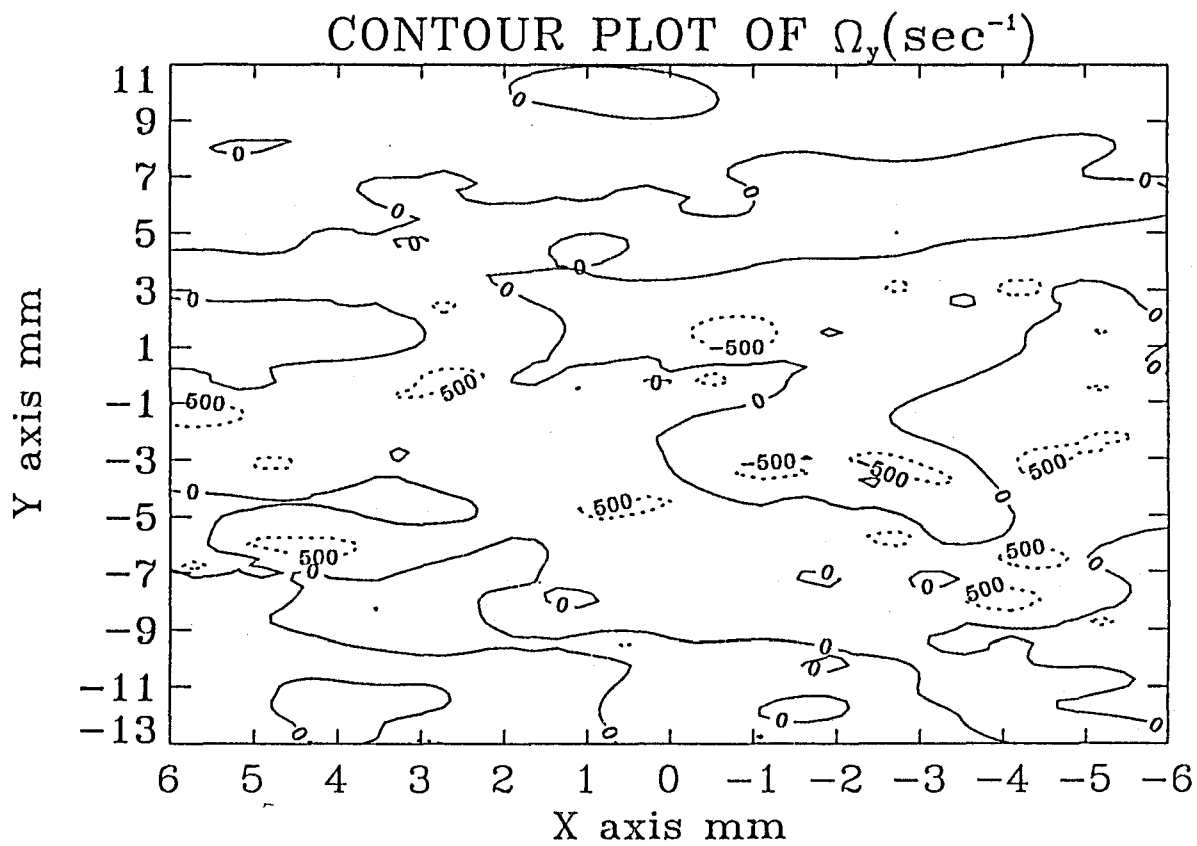


Fig. 6.18. Contour plot of vorticities in Y-direction at $x/d \approx 20$.

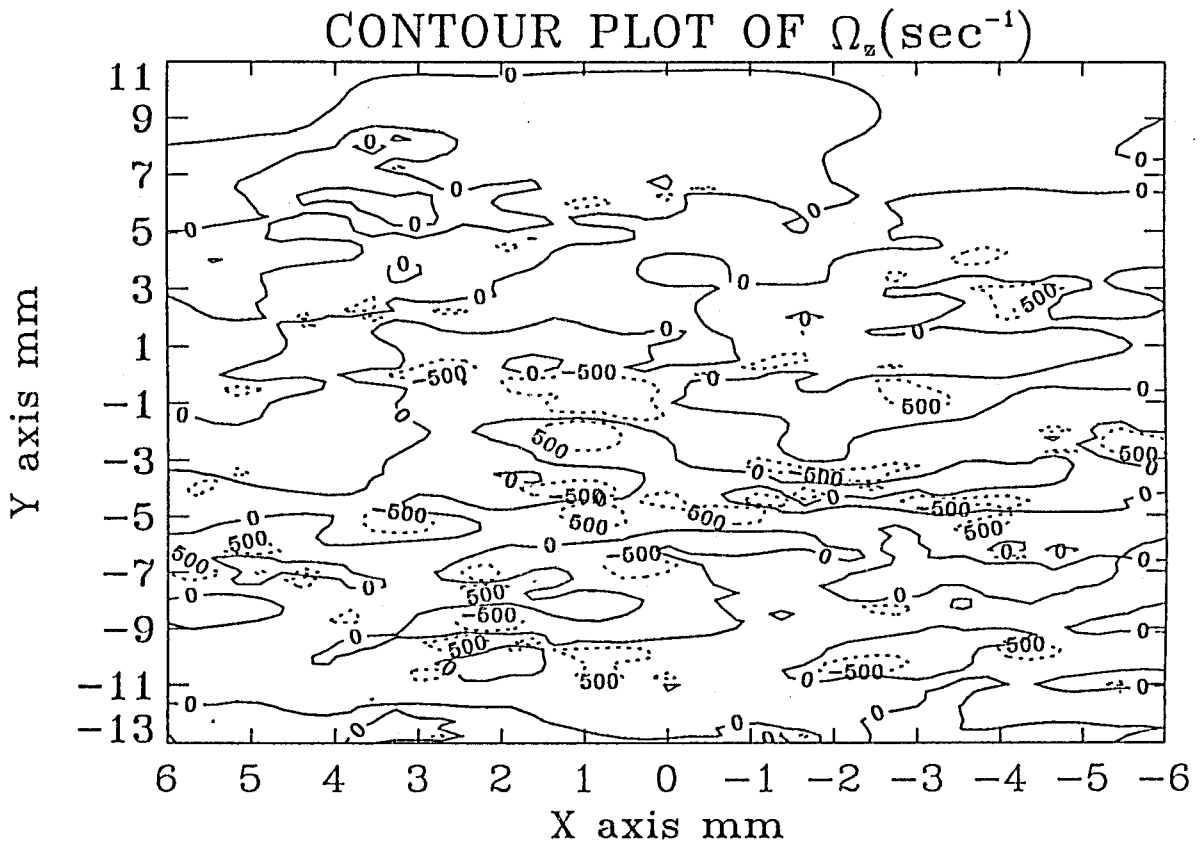


Fig. 6.19. Contour plot of vorticities in Z-direction at $x/d \cong 20$.

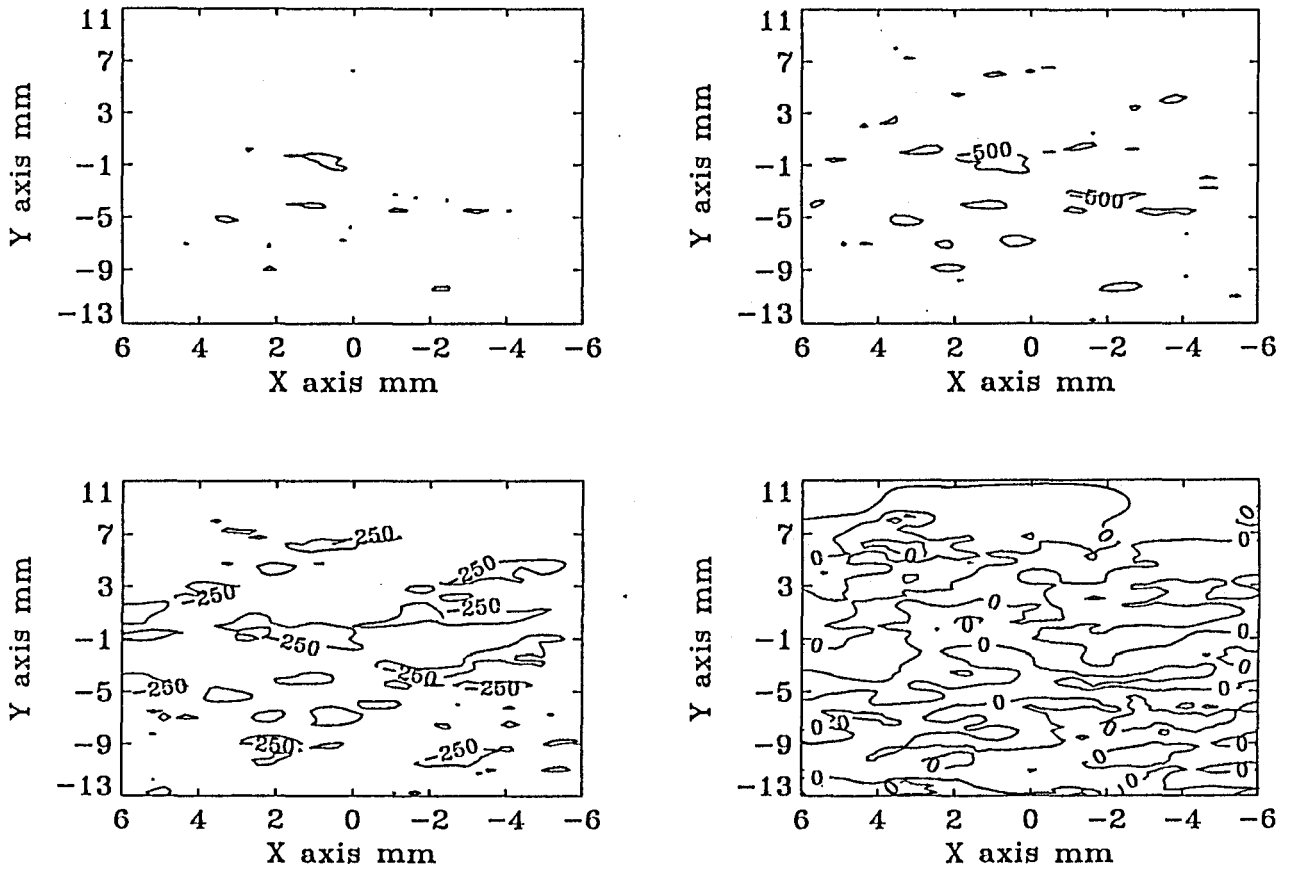


Fig. 6.20a. Contour plot of vorticities in Z-direction in levels $-750s^{-1}$, $-500s^{-1}$, $-250s^{-1}$ and $0s^{-1}$ at $x/d \cong 20$.

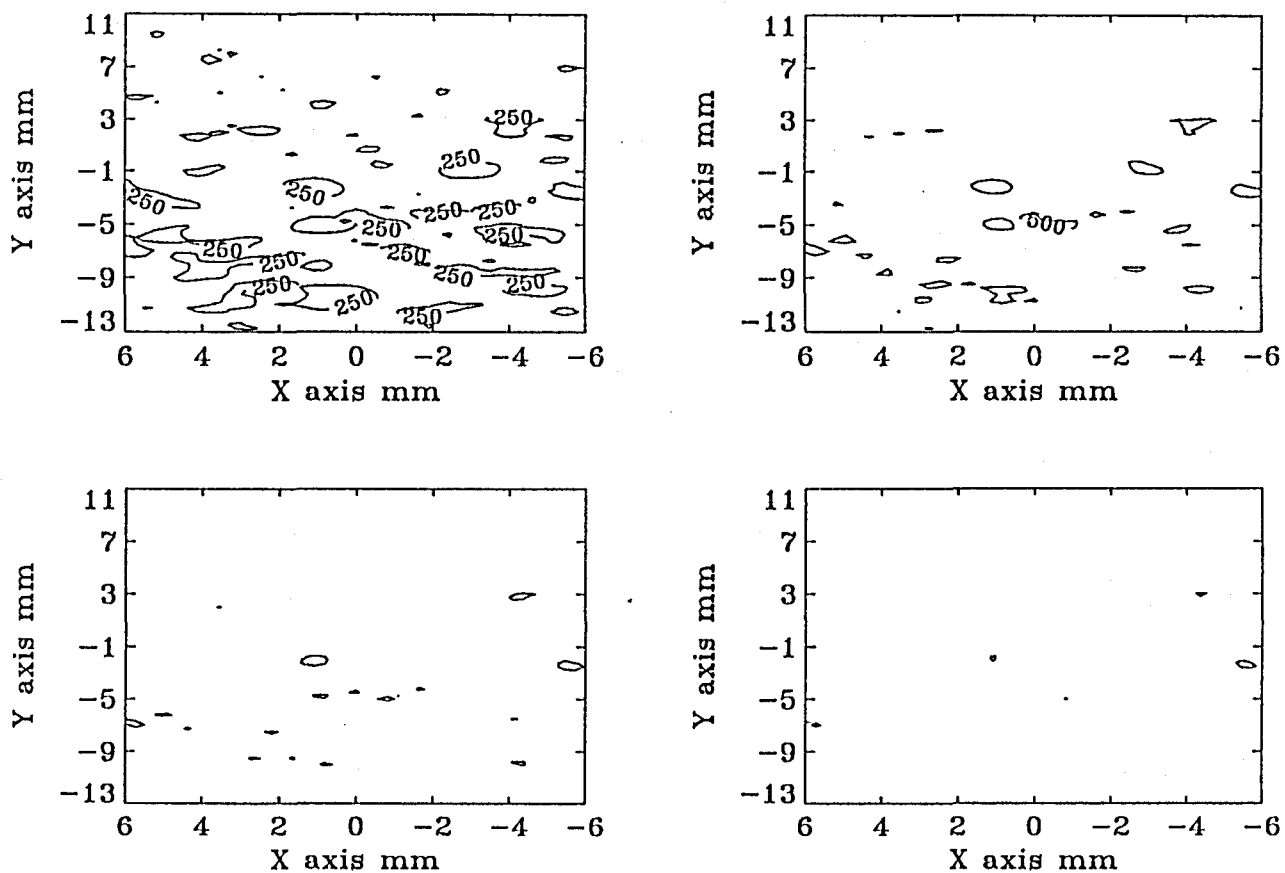


Fig. 6.20b. Contour plot of vorticities in Z-direction in levels 250s⁻¹, 500s⁻¹, 750s⁻¹ and 1000s⁻¹ at x/d=20.

6.4 ESTIMATION OF TURBULENT SCALES

Since pointwise measurement techniques such as hot-wire anemometry have traditionally been used to measure turbulent parameters, features such as the 'eddy size' have been estimated in a different way. Therefore the present data were also interpreted in a classical fashion. The 'average eddy scale' is defined as $\Lambda = \bar{u} \int_0^T R_t d(\delta t)$ (Sami et. al., 1967) where the auto-correlation coefficient R_t is given by $R_t = \frac{[u'(t).u'(t+\delta t)]}{u'(t)^2}$, δt is the delay time and T is the total interval time. The values of R_t for different values of δt ranging from 1 to 15 ms were calculated. The value of the integration is the area under the auto-correlation curve. This was computed numerically by using the trapezoidal rule. Figure 6.21 shows the plot of Λ/d versus r/R . The 'average eddy scale' increases steadily from a minimum in the boundary to a maximum at the center-line. The same trend was observed from the measurements of Sami et. al., (1967) measured at the $x/d \cong 10$ location in a jet of $Re = 2.2 \times 10^4$.

Longitudinal and lateral microscales λ_f and λ_g (Hinze, 1975) are given by

$$\frac{1}{\lambda_f^2} = \frac{1}{2\bar{u}'^2} \overline{\left(\frac{\partial u'}{\partial x}\right)^2} ; \quad \frac{1}{\lambda_g^2} = \frac{1}{2\bar{u}'^2} \overline{\left(\frac{\partial u'}{\partial y}\right)^2}. \quad (6.12)$$

These microscales were calculated for the flow at both x/d locations and are tabulated in Table 6.2. The Kolmogorov microscale (η) is the smallest scale that occurs in the flow before the turbulent energy is directly dissipated by viscosity. The Kolmogorov microscale can be estimated using,

TABLE 6.1 Mean Spacing Between Vortex Centers Measured from the Contour Plots

S.no	Vorticity s ⁻¹	Mean Spacing mm	
		x/d≅10	x/d≅20
1	-750	4.17	3.82
2	-500	3.72	3.43
3	-250	7	4.09
4	250	6.5	2.86
5	500	3.22	4.07
6	750	4.28	3.79

TABLE 6.2 Turbulent Microscales

Microscale	Axial Location	
	x/d = 12	x/d = 22
λ_f mm	0.546	0.222
λ_g mm	0.498	0.431

Table 6.3 Kolmogorov Microscales

Kolmogorov Microscale	Axial Location	
	x/d = 12	x/d = 22
η_f mm	0.017	0.019
η_g mm	0.018	0.014

$\eta = \lambda / (15^{0.25} Re_\lambda^{0.5})$; where $Re_\lambda = \sqrt{u'^2} \lambda / \nu$ where u' is the fluctuating velocity in the longitudinal direction, λ is the turbulent microscale and ν is the kinematic viscosity (Tennekes and Lumley, 1972). The values of η estimated at $x/d=12$ and 22 locations are tabulated in Table 6.3.

One of the primary objectives of the present study is to calculate turbulent scales. There are many circumstances where liquid turbulence leads to deformation and break-up of bubbles. Preliminary experiments (Kolaini, 1993) showed that in some cases bubbles around 2-mm diameter were re-excited by the jet flow. The bubbles then emitted sound at about 3 kHz. The mechanisms coupling the bubble deformation to the turbulent flow were to be uniquely identified. When bubbles are introduced into the turbulent flow field, vortical structures of different sizes and turbulent fluctuations contribute to deforming and oscillating the bubbles. A bubble may be subjected to surface and volume modes of oscillation. Also re-excitation of the bubble can occur due to the non-linear coupling between the surface and volume modes of oscillation. Surface mode oscillations are thought to be the primary cause of bubble deformation which may lead to break-up.

Knowledge of the vortical structures is required to characterize these bubble oscillations. In the present measurement, large coherent structures were probably not detected due to the limited size of the measurement volume, and the lower integration time (less than 0.5 second) (see Figs. 6.16a, 6.16b; Figs. 6.20a, 6.20b). Due to the limitations in seeding the flow densely with tracer particles, vortical structures smaller than the average distance between the particles were also not detected.

Assuming that the bubble is convected with a velocity (V_c) equal to the mean velocity, the bubble encounters the vortices at a frequency f equal to V_c/L where V_c is the convection velocity and L is the mean spacing between successive vortices. As seen from Table 6.1 the mean spacing between vortical structures is too large to excite surface modes on a bubble of say, 2 mm in diameter. Even the turbulent microscales as shown in Table 6.2 are comparable in size with the bubble radius; hence they will not induce any appreciable surface modes on the bubble. In order to set the surface mode into oscillation, smaller (one order of magnitude smaller than the bubble diameter) and energetic vortices are required at the surface of the bubble. However, it seems that smaller vortical structures which could not be reliably detected with the present measurements, were responsible for the surface modes detected by Kolaini (1993). Vortical structures of sizes between the turbulent microscale and the Kolmogorov microscale may be responsible for the re-excitation of the bubble with its natural frequency of 3 kHz through the coupling between surface mode and volume mode oscillations.

A plot of the instantaneous velocity vectors for the duration of 0.1 second is shown in Fig. 6.22 for the $x/d \cong 10$ location. The velocities were interpolated using the multiquadric interpolator from the instantaneous vectors on to a uniform grid on the XY

(in-plane) plane. The same is shown for $x/d \cong 20$ location in Fig. 6.23. Some overall features of the flow can be seen from these figures (e.g. recirculation zones near the jet boundaries).

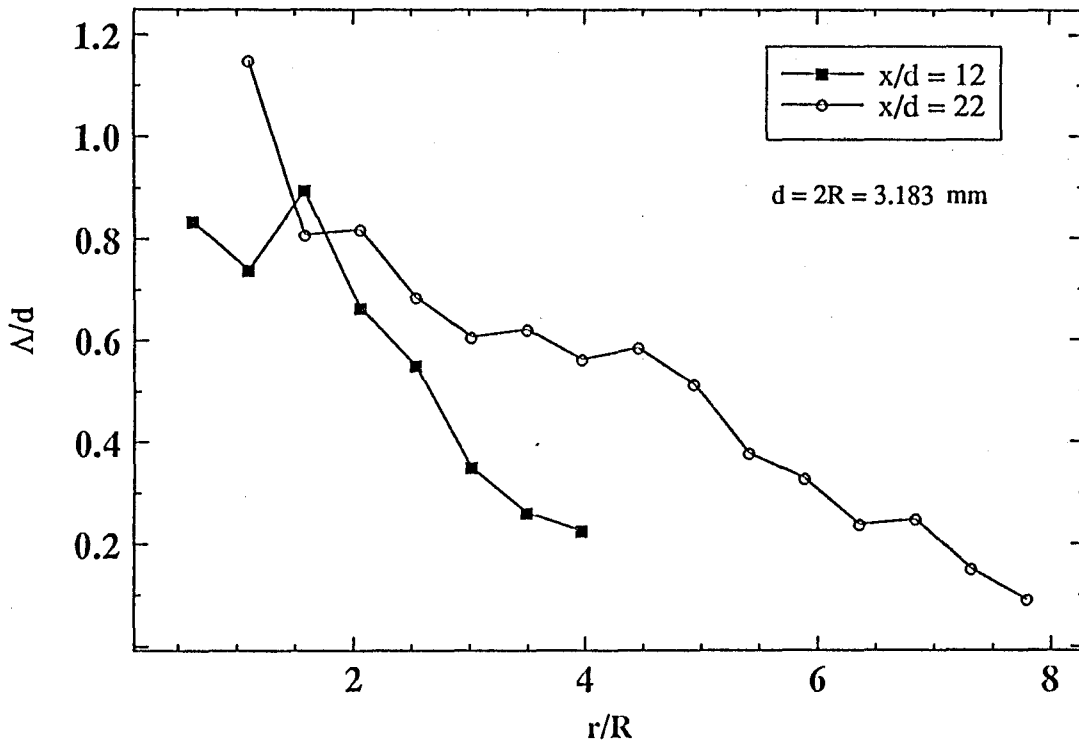


Fig. 6.21. Plot of 'average eddy scale' across the jet.

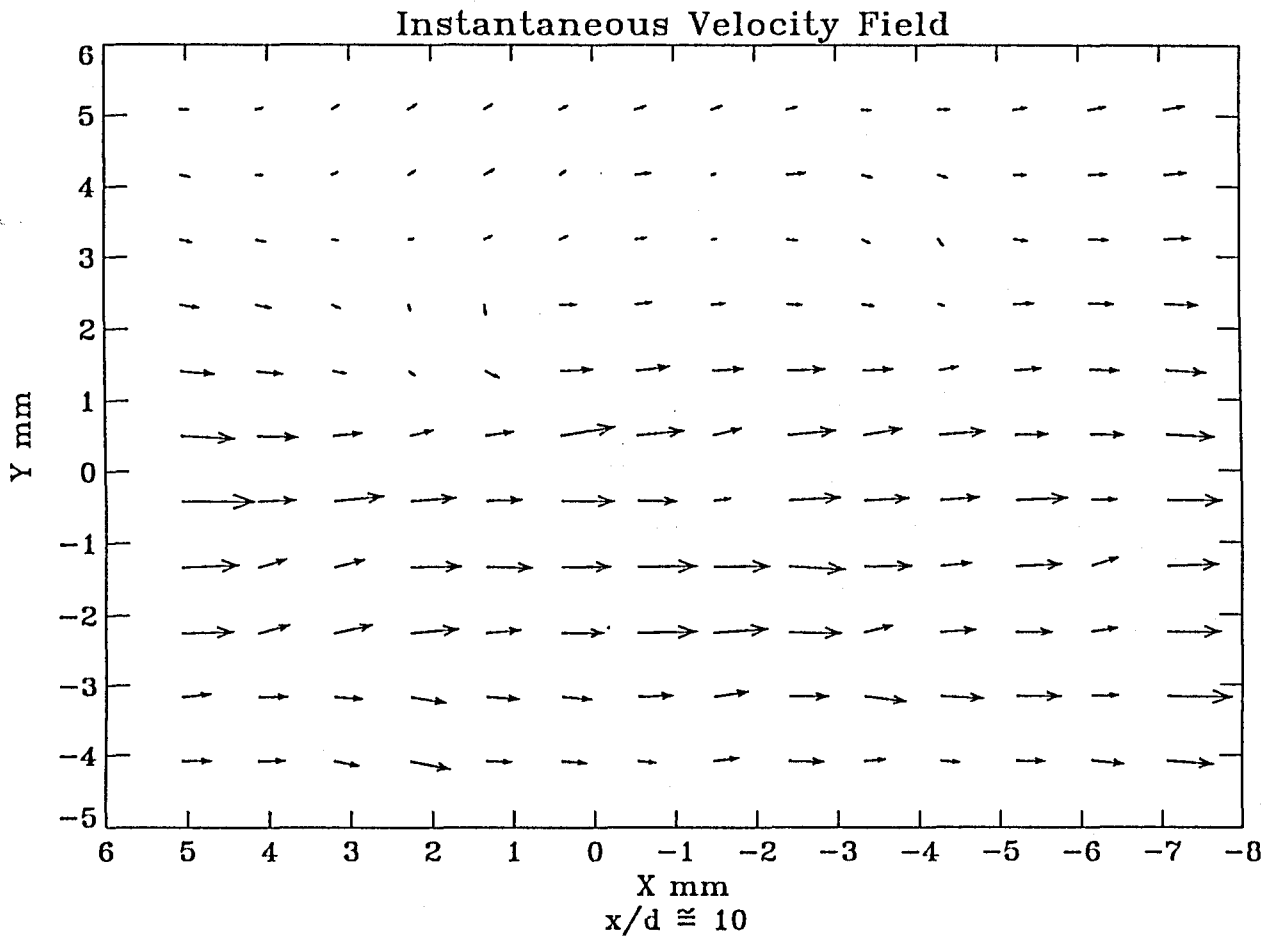


Fig. 6.22. Instantaneous velocity vector plot for the duration of 50 ms at $x/d \cong 10$.

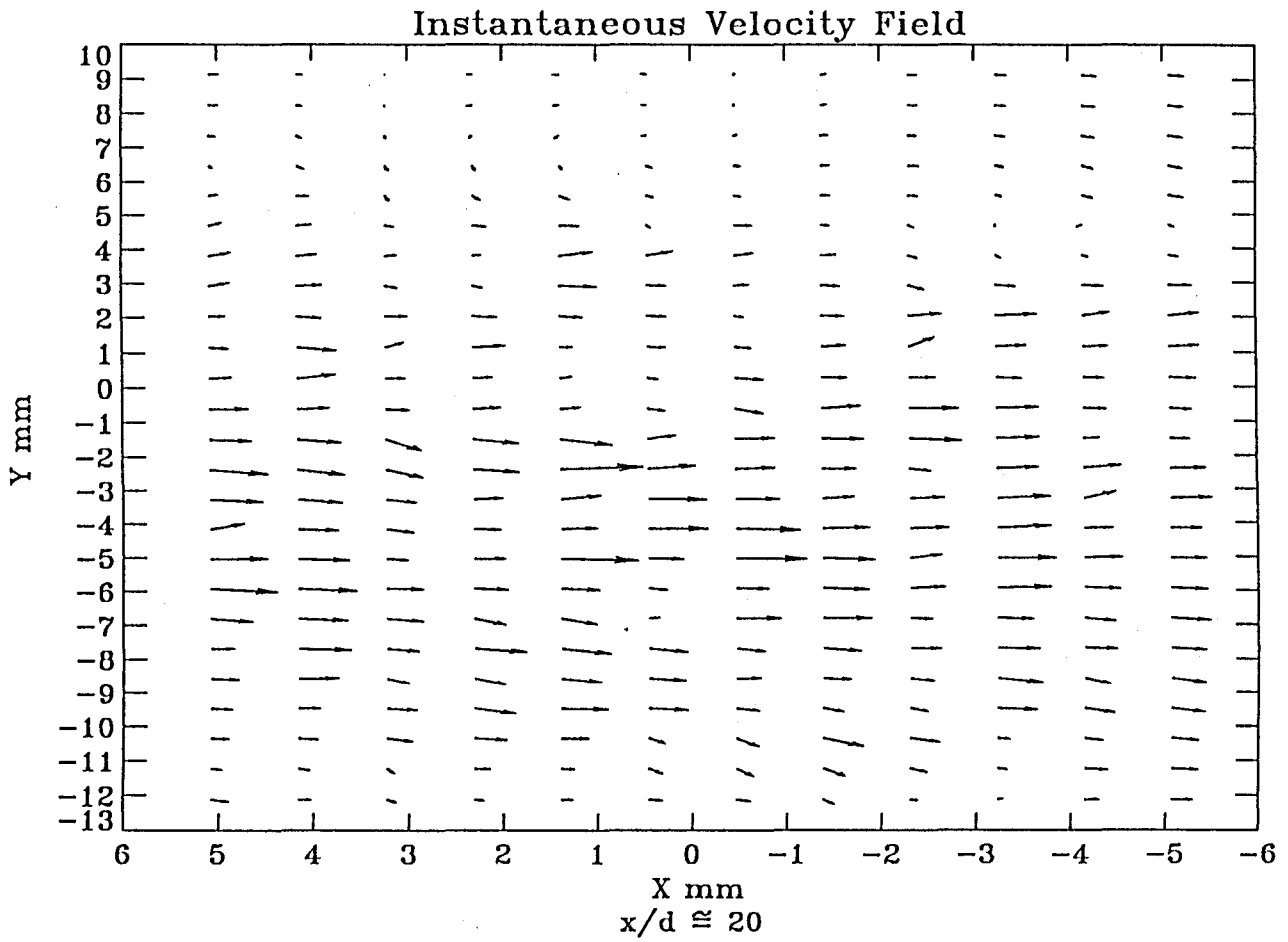


Fig. 6.23. Instantaneous velocity vector plot for the duration of 100 ms at $x/d \approx 20$.

Chapter 7

CONCLUSIONS AND RECOMMENDATIONS

7.1 INTRODUCTION

Particle tracking velocimetry is a technique where several variables need to be optimized. Particle seeding density, threshold for light intensity, threshold for valid particle size, criteria for matching and tracking and parameters in the interpolation scheme are some of the important parameters that need to be optimized to get meaningful data using this technique. Many times, the optimized values for the parameters mentioned above are specific to the particular flow situation and may be quite unsuitable for application to other situations. Due to this, many sources of error exist in applying this technique. Here the primary sources of errors are discussed and the experimental results are summarized.

7.2 MEASUREMENT ERRORS

A problem inherent in particle tracking velocimetry is the propagation of errors through the various steps involved in finding the X, Y and Z positions of the points in space from their images. The errors in Z (depth) direction are one order of magnitude higher than those in X and Y directions. Although a full uncertainty analysis was not performed, possible errors their causes and effects are discussed here. Methods of eliminating or reducing the errors are also discussed. The primary causes of errors in the present case were: (i) errors involved in determining the depth positions of particles

accurately; (ii) ambiguities in finding correct correspondences in matching and tracking; and (iii) errors involved in finding centroids of particle images due to the limited picture resolution and particle occlusion. The error involved in finding the centroids of the particle images is considered to be the major source of error in the present study.

7.2.1 Errors in Finding Depth Positions

As shown in the Figs. 3.4 a, 3.4 b and 3.4 c, the camera sees the movement of the particle on the X axis (say, left to right) and along the Z axis (say, front to back) as a horizontal movement, whereas the movement in Y axis is seen as a vertical movement. Since particles move randomly in a turbulent flow, combinations of X, Y, and Z movements occur. For example, a translatory displacement of particle as recorded by the camera may be composed of movements in X, Y and Z. The movement in the X-Y plane (in-plane) is detected very well by the camera since the X movement is a horizontal translation and Y movement is a vertical translation in the image plane. But movements in the Y-Z and Z-X planes are more difficult to detect. Hence it is imperative that the modified camera parameters, when combined with particle positions, should be able to decompose the movements of particles into their respective directions. It should be recalled that in order to reduce the errors in Z the reference grid points were made to have a depth spacing close enough to approximate the average spacing between the particles. However, it is difficult to ascertain the adequacy of the number of depth planes to be used and the optimum spacing to be kept between them. Increasing the number of grid points used for calibration may increase the resolution in the Z direction. However, the computational difficulties involved in solving very large number of nonlinear equations make this impractical.

7.2.2 Errors in Matching and Tracking of Particles

The errors associated with the matching and tracking of the particles rests solely on the algorithm developed to match and track the particles. As mentioned in Chapter 3, since the viewing is done from two different directions, the average distance between the particles in image A and that of image B are different. For this reason, two distinctly visible particles in one of the images may have corresponding particles which may hide one another in the other image. Therefore all particles in image A may not have unique matches in image B. Moreover, a size thresholding is specified to eliminate the pixel blocks (created by particles hiding one another) bigger than the typical size of a single particle. It is possible such a pixel block is eliminated in one of the images, leaving the corresponding particles in the other view without corresponding matches. Since the criteria for matching and tracking are found empirically ("xtolerance" and "ytolerance") some uncertainty is involved.

7.2.3 Errors in Finding the Centroids of Particle Images

It can be recalled that the stationary points in several depth planes were calibrated to a high degree of accuracy as mentioned in Chapter 5. This implies, within the test volume, given image coordinates of the particles, the world coordinates (X, Y and Z positions) can be computed accurately. One of the problems in doing so, is the movement of the particles. Even though the centroids are found to within sub-pixel accuracy, the errors involved are relatively large compared to those of finding the centroid positions of grid points used for calibration. Since the grid points are stationary, relatively large and of uniform size, their images are well defined compared to the images

of moving particles. For example, a typical grid point image occupied 20 pixels, whereas a typical particle occupied between 3 to 8 pixels. Also these pixel blocks are defined through an image intensity thresholding procedure. This results in distorting the image boundaries. Thus the centroids of larger pixel groups can be estimated more accurately. In the present case the screen pixel to image size ratio was such that, for a selected magnification of 0.5, one pixel error in the centroid position of the particle translates to displacements of 0.198 mm and 0.194 mm in X and Y coordinates respectively. Since velocity = displacement/time step (say, $u = \frac{X_2 - X_1}{\Delta t}$) and time step (Δt) at an imaging speed of 2000 frames per second is 5×10^{-4} sec, an error of 397.5 mm/sec and 316.8 mm/sec will occur in X and Y velocities. This is an estimate only since the movement in Z (depth) direction is not taken into account.

Particle coalescence is another major problem in distorting the particle centroid positions. As mentioned earlier, a special Kodak made Photo-Flo solution was used to prevent the problem of particles coalescing and forming blobs. Because of the small angle stereo viewing, some of the particles were hidden by others. This resulted in centroids being found erroneously, starting the error which propagated downstream. Though a size threshold was specified to eliminate particle images bigger than the typical size of a single particle, it was not always possible to eliminate this error considering that the particles themselves varied in size by $\pm 100 \mu\text{m}$ according to the manufacturer's specifications.

7.3 CONCLUSIONS

The mean velocity profiles were seen to be in good agreement with the results of the earlier experimental investigations. The magnitudes of the center-line velocities were

found to be in good agreement with those calculated by empirical relations. The fluctuating components of velocities, however, did not follow any clear trend. This suggests that if particle data for longer duration are analyzed, the behavior of the fluctuating velocities can be deduced accurately. Alternatively, the data density in each frame needs to be increased.

The errors involved in determining the Z (depth) positions of the particles have propagated into the calculations of the fluctuating component of Z velocity and its cross correlations; thus these parameters were not accurate. However, spatially, the results have shown the turbulent flow structures with good resolution. Their vorticities ranged approximately between -750s^{-1} and 750s^{-1} . It was possible to visualize and calculate the turbulent scales across the jet throughout the entire flow volume. The results and accompanying discussions have given some hints as to how the bubbles get deformed and oscillated when introduced into a turbulent flow field. Some problems were encountered while estimating the range of flow features occurring temporally. Use of the multiquadric interpolator in its present form has been found inadequate to interpolate the instantaneous velocities since these velocities contained high frequency fluctuations and small scale structures. These velocities occur randomly in time and space with random magnitudes. The multiquadric interpolator calculates an interpolant from the known data points by exactly solving the function equations. Hence a combination of multiquadric interpolator with a non-linear least-squares function fit has to be employed to interpolate the instantaneous velocities to the desired locations.

Velocity data were averaged for 100 ms and 50 ms at two downstream locations in the jet. Earlier investigations in the turbulent jet were carried out for longer durations (in the order of minutes) and averaged results of various parameters were reported. It was

apparent from an FFT (fast Fourier transform) of a single point hot-film measurement of the present jet that the averaging time should be increased to about 1 minute to even out the slowest fluctuations. Thus a 100 ms average was probably skewed with respect to the true mean. For this reason, a comparison of all such parameters obtained from earlier investigations with those obtained in the present study could not be made. Efforts are currently underway to use the hot-film probe and measure velocities and turbulent quantities for a comparable period of time as the present technique, to compare all the possible turbulent parameters.

7.4 RECOMMENDATIONS

It can be concluded that the camera calibration and the correction for refraction effects were done with a high level of accuracy. But the errors in the measurements were seen to be much larger. Hence the following recommendations are aimed at reducing these errors. Also these recommendations might be helpful for improving the overall accuracy of the technique:

- (i) Employing wide-angle stereo or orthogonal viewing to improve the depth resolution.
- (ii) Using an additional camera (or cameras) will help in improving the depth resolution. This would enhance the chances of making more particles distinctly visible compared to the small-angle stereo-viewing employed in the present study. Therefore this would reduce the problem of particles in different depth planes hiding one another which was experienced in the present case.
- (iii) Images having a resolution better than the present 256 x 240 pixels, will improve the ratio of pixels on the screen to the image size. Instead of a two-level intensity

LIST OF ABBREVIATIONS

a_{ij}	Coefficients of transformation matrix
c_j	Vector of reconstruction coefficients for multiquadric interpolator
f	Principal distance
d	Exit diameter of the nozzle
L	Mean spacing between vortical structures
m	Filter shape factor for multiquadric interpolator
O	Lens center
P	Particle or point
pp	Principal point
R	Spatial averaging parameter for multiquadric interpolator
R_t	Auto-correlation coefficient
t	Time
Greek	
Δ	Finite change
μm	Micron
ω	Angle of rotation of world coordinate system with respect to its X axis
ϕ	Angle of rotation of world coordinate system with respect to its Y axis
ψ	Angle of rotation of world coordinate system with respect to its Z axis
Ω	Vorticity

Λ	Average eddy scale
λ	Turbulent microscale
ρ	Density
ζ	Similarity variable
η	Kolmogorov microscale

REFERENCES

1. Abramovich, G. N. (1963), *The Theory of Turbulent Jets*, M.I.T Press, Cambridge, Mass.
2. Adamczyk, A., Rimai, L. (1988), "Reconstruction of a 3-Dimensional Flow Field From Orthogonal Views of Seed Track Video Images," *Experiments in Fluids*, 6, pp. 380-386.
3. Adrian, R. (1986), "Multi-Point Optical Measurements of Simultaneous Vectors in Unsteady Flow - a Review," *International Journal of Heat and Fluid Flow*, Vol. 7, No.2., pp. 127-145.
4. Corrsin, S., and Uberoi, M. S. (1949), "Further Experiments on the Flow and Heat Transfer in a Heated Turbulent Jet," *NACA Rept..no.1865*.
5. Corrsin, S., and Kistler, A. L. (1955), "Free-stream Boundaries of Turbulent Flows," *NACA Rept. no.1244*.
6. Davies, P. O. A. L., Fisher, M. J., and Barratt, M. J. (1963), "The Characteristics of the Turbulence in the Mixing Region of a Round Jet," *Journal of Fluid Mechanics*, Vol. 15., pp. 337-367.
7. Fu, K. S., Gonzalez, R. C., and Lee, C. S. G: *Robotics - Control, Sensing, Vision, and Intelligence*; McGraw-Hill, 1987.
8. Ganapathy, S. (1975), "Reconstruction of Scenes Containing Polyhedra From Stereo Pair of Views," *Stanford Artificial Intelligence Lab. Memo AIM-272*, December 1975.

9. Gibson, M. M. (1963), "Spectra of Turbulence in a Round Jet," *Journal of Fluid Mechanics*, Vol. 15, pp. 161-173.
10. Görtler, H. (1942), "Berechnung von Aufgaben der Freien Turbulenz auf Grund eines Neuen Näherungsansatzes," *Z. Angew. Math. Mech.*, vol. 22, pp. 244-254.
11. Hinze, J. O.: *Turbulence*, 2nd ed., McGraw-Hill, New York, 1975.
12. Jacobi, O., (1980), "Photogrammetric Tracking of a Moving Particle in Running Water," *International Archives of Photogrammetry*, Vol. XXIII, pp. 369-374.
13. Kolaini, A. R. (1993), "Nonlinear Coupling Between Surface Mode and Volume Mode Pulsations of a Bubble in the Turbulent Flow Field," To be submitted to *J. Acoust. Soc. Am.*
14. Kuhlman, P. S. (1990), *Quantitative Three Dimensional Flow Visualization Using Stereoscopic Particle Streak Velocimetry*, M. S. Thesis, University of Nebraska.
15. Laufer, J. (1954), "The Structure of Turbulence in a Fully Developed Pipe Flow," *NACA Rept. no. 1174*.
16. Maas, H. G. (1991), "A High Resolution Photogrammetric 3-D Particle Tracking Velocimeter," FED-Vol. 128, *Experimental and Numerical Flow Visualization*, ASME 1991, pp. 79-84.
17. Mangla, N. L. (1992), *On Improving the Accuracy of Stereoscopic Particle Imaging Technique Towards Estimating the Three Dimensional Vorticity Field*, M. S. Thesis, University of Mississippi.
18. Nishino, K., Kasagi, N., and Hirata, M. (1989), "Three Dimensional Particle Tracking Velocimetry Measurement," *Journal of Fluids Engineering.*, Vol. 111, pp. 384-391.

19. Praturi, A. K., Brodkey, R. S. (1978), "A Stereoscopic Visual Study of Coherent Structures in Turbulent Shear Flow," *Journal of Fluid Mechanics*, Vol. 89, pp. 251-272.
20. Racca, R. G., Dewey, J. M. (1988), "A Method for Automatic Particle Tracking in a Three-Dimensional Flow Field," *Experiments in Fluids*, 6, pp. 25-32.
21. Rajendran, V. P., Kolaini, A. R., and Sinha, S. K. (1993), "Characterization of an Axisymmetric Turbulent Jet Using 3-D Particle Tracking Velocimetry," FED-Vol. 155 *Forum on Turbulent Flows*, ASME 1993, pp. 7-11.
22. Sami, S., Carmody, T., Rouse, H. (1967), "Jet Diffusion in the Region of Flow Establishment," *Journal of Fluid Mechanics*, Vol. 27, pp. 231-252.
23. Schlichting, H.: *Boundary Layer Theory*, 7th ed., McGraw-Hill, 1979.
24. Sheu Y. H. E., Chang T. P. K. and Tatterson G. B. A. (1982), "Three Dimensional Measurement Technique for Turbulent Flows," *Chem. Eng. Commun.*, 17, pp. 67-83.
25. Sinha, S. K. (1988), "Improving the Accuracy and Resolution of Particle Image or Laser Speckle Velocimetry," *Experiments in Fluids*, 6, pp. 67-68.
26. Sinha, S. K., Kuhlman, P. S., (1992) "Investigating the Use of Stereoscopic Particle Streak Velocimetry for Estimating the Three-Dimensional Vorticity Field," *Experiments in Fluids*, Vol. 12, No.6, pp. 377-384.
27. Sobel, I. (1974), "On Calibrating Computer Controlled Cameras for Perceiving 3-D scenes," *Artificial Intelligence*, Vol. 5, pp. 185-198.
28. Tatterson, G. B., Yuan, H. H. S., Brodkey, R. S., (1980) "Stereoscopic Visualization of the Flows for Pitched Blade Turbines," *Chem. Eng. Sci.*, 35, pp. 1369-1375.
29. Tennekes, H., and Lumley, J. L.: *A First Course in Turbulence*, The M.I.T.-Press, London, 1972.

30. White, F. M.: *Viscous Fluid Flow*; McGraw-Hill, 1975.
31. Wagnanski, I., Fiedler, H. (1969), "Some Measurements in the Self-preserving Jet," *Journal of Fluid Mechanics*, Vol. 38, part 3, pp. 577-612.

APPENDIX A: Derivation of Data Reduction Equations

Figure A1 shows the plan view of the coordinates used to derive the data reduction equations. The following notations are employed

- (i) X, Y, Z - World coordinates of an object point measured with respect to the world coordinate frame;
- (ii) x', y', z' - Image coordinates of the point P , say P' . Coordinates x' and y' can be measured from the 2-D image. Z' is the principal distance f , which is equal to the object distance when the magnification is 1;
- (iii) X_m, Y_m, Z_m - World coordinates measured with respect to the common origin.

The following steps are taken to arrive at a relation between world coordinates of an object point P and the image coordinates of its image P' in camera A

- (i) Rotation of the world coordinate system X, Y, Z with respect to X to get X' (same as X), Y', Z' ;
- (ii) Rotation of the coordinates X', Y', Z' with respect to Y' to get X'', Y'' (same as Y'), Z'' ;
- (iii) Rotation of the coordinates X'', Y'', Z'' with respect to Z'' to get X''', Y''' , Z''' (same as Z'');
- (iv) Translation of the rotated world coordinates X''', Y''', Z''' to the respective camera lens center X_{OA}, Y_{OA}, Z_{OA} .

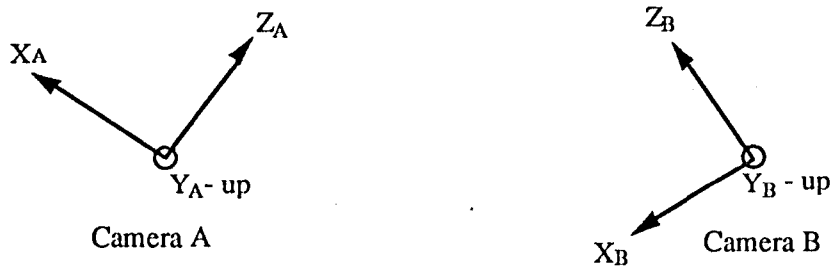
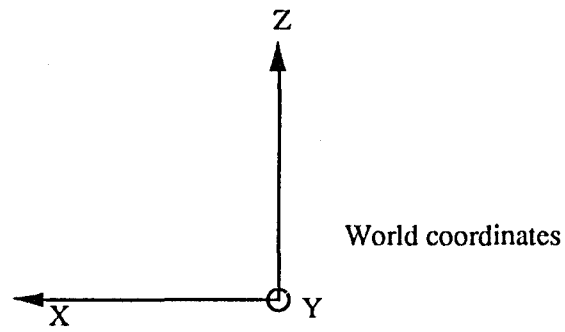


Fig. A1. Plan view of the coordinates used for viewing.

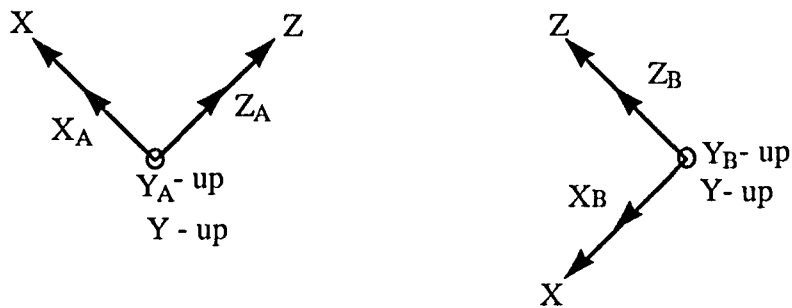


Fig. A2. Plan view of the coordinates after rotations and translation.

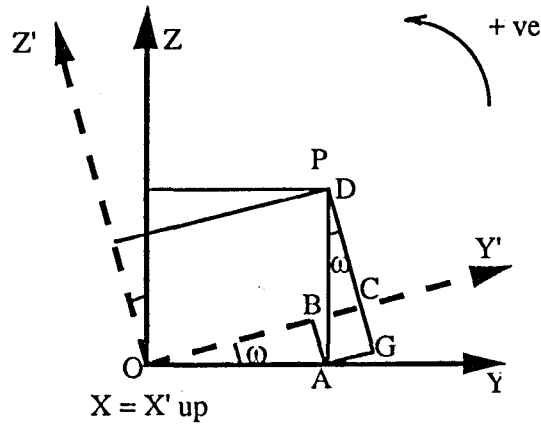


Fig. A3. X-rotation of world coordinates.

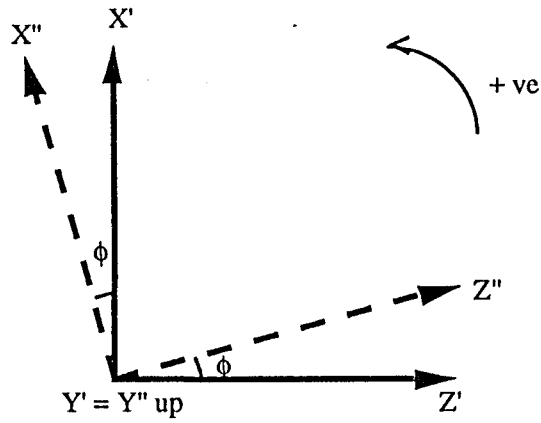


Fig. A4. Y-rotation of world coordinates.

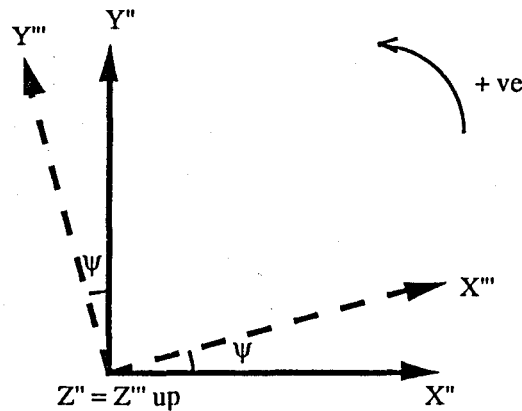


Fig. A5. Z-rotation of world coordinates.

Note: The resultant of rotations and translation is the same regardless of the order in which they are performed.

Now the origins of the world coordinate frame and the image coordinate frame are coincident and point in the same direction. We denote this as common origin. And the notations X_m, Y_m, Z_m are used instead of X''', Y''', Z''' . These are world coordinates of the point measured with respect to the common origin. Figure A2 Shows the common origin along with the object and its image.

Since $P (X_m, Y_m, Z_m), O_A (X_{OA}, Y_{OA}, Z_{OA})$ and $P' (x', y', z')$ should lie in a single line to form the image, the following relations (Fu et. al. 1987) should hold
 Due to similar triangles (see also Fig. 2.4) $\frac{X_m}{x'} = \frac{Z_m}{z'}$ and $\frac{Y_m}{y'} = \frac{Z_m}{z'}$ hence

$$x' = z' \frac{X_m}{Z_m} \quad (\text{A.1})$$

$$y' = z' \frac{Y_m}{Z_m} \quad (A.2)$$

The following section describes the sequence to be followed to arrive at X_m, Y_m, Z_m of a point, given its X, Y, Z coordinates. Rotation of the world coordinate system with respect to its X axis is effected (see Fig. A3).

(i) X, Y, Z rotated with respect to X to get X', Y', Z' .

$$X' = X$$

$$OC = OA \cdot \cos\omega + BC(=AG)$$

$$Y' = Y\cos\omega + Z\sin\omega \text{ and}$$

$$OF = DG - GC(=AB)$$

$$Z' = Z\cos\omega - Y\sin\omega$$

in matrix form

$$\begin{pmatrix} X' \\ Y' \\ Z' \end{pmatrix} = \begin{pmatrix} 1 & 0 & 0 \\ 0 & \cos\omega & \sin\omega \\ 0 & -\sin\omega & \cos\omega \end{pmatrix} \begin{pmatrix} X \\ Y \\ Z \end{pmatrix} \quad (A.3)$$

(ii) Second rotation: X', Y', Z' with respect to Y' to get X'', Y'', Z'' (See Fig. A4).

$$Z'' = Z'\cos\phi + X'\sin\phi$$

$$X'' = X'\cos\phi - Z'\sin\phi$$

$$Y'' = Y'$$

in matrix form

$$\begin{pmatrix} X'' \\ Y'' \\ Z'' \end{pmatrix} = \begin{pmatrix} \cos\phi & 0 & -\sin\phi \\ 0 & 1 & 0 \\ \sin\phi & 0 & \cos\phi \end{pmatrix} \begin{pmatrix} X' \\ Y' \\ Z' \end{pmatrix} \quad (\text{A.4})$$

(iii) Third rotation: X'' , Y'' , Z'' rotated with respect to Z'' to get X''' , Y''' , Z''' (X_m , Y_m , Z_m)

(see Fig. A5).

$$X''' = X''\cos\psi + Y''\sin\psi$$

$$Y''' = Y''\cos\psi - X''\sin\psi$$

$$Z''' = Z''$$

in matrix form

$$\begin{pmatrix} X''' \\ Y''' \\ Z''' \end{pmatrix} = \begin{pmatrix} \cos\psi & \sin\psi & 0 \\ -\sin\psi & \cos\psi & 0 \\ 0 & 0 & 1 \end{pmatrix} \begin{pmatrix} X'' \\ Y'' \\ Z'' \end{pmatrix} \quad (\text{A.5})$$

Substituting Eq. (A.3) in Eq. (A.4) and taking the resultant and substituting in Eq. (A.5),

we get

$$\begin{pmatrix} X''' \\ Y''' \\ Z''' \end{pmatrix} = \begin{pmatrix} \cos\psi & \sin\psi & 0 \\ -\sin\psi & \cos\psi & 0 \\ 0 & 0 & 1 \end{pmatrix} \begin{pmatrix} \cos\phi & 0 & -\sin\phi \\ 0 & 1 & 0 \\ \sin\phi & 0 & \cos\phi \end{pmatrix} \begin{pmatrix} 1 & 0 & 0 \\ 0 & \cos\omega & \sin\omega \\ 0 & -\sin\omega & \cos\omega \end{pmatrix} \begin{pmatrix} X \\ Y \\ Z \end{pmatrix}$$

As mentioned earlier X''' , Y''' , Z''' are called X_m , Y_m , Z_m and they are in the form

$$\begin{pmatrix} X_m \\ Y_m \\ Z_m \end{pmatrix} = \begin{pmatrix} a_{11} & a_{12} & a_{13} \\ a_{21} & a_{22} & a_{23} \\ a_{31} & a_{32} & a_{33} \end{pmatrix} \begin{pmatrix} X \\ Y \\ Z \end{pmatrix} \quad (\text{A.6})$$

After the translation of the world coordinate origin to the camera A lens center is effected, Eq. (A.6) modifies to

$$\begin{pmatrix} X_m \\ Y_m \\ Z_m \end{pmatrix} = \begin{pmatrix} a_{11} & a_{12} & a_{13} \\ a_{21} & a_{22} & a_{23} \\ a_{31} & a_{32} & a_{33} \end{pmatrix} \begin{pmatrix} X-X_{OA} \\ Y-Y_{OA} \\ Z-Z_{OA} \end{pmatrix}$$

Expanding

$$X_m = (X - X_{OA}).a_{11} + (Y - Y_{OA}).a_{12} + (Z - Z_{OA}).a_{13}, \quad (A.7)$$

$$Y_m = (X - X_{OA}).a_{21} + (Y - Y_{OA}).a_{22} + (Z - Z_{OA}).a_{23}, \quad (A.8)$$

$$Z_m = (X - X_{OA}).a_{31} + (Y - Y_{OA}).a_{32} + (Z - Z_{OA}).a_{33}. \quad (A.9)$$

Substituting Eqs. (A.7), (A.8) and (A.9) into Eqs. (A.1) and (A.2), and denoting Z' as f , we obtain the data reduction Eqs. (2.1) and (2.2). To correct for the image coordinates for the location of the principal point, x_{app} and y_{app} are added .

$$x_a = f_a \left(\frac{a_{11}(X-X_{OA}) + a_{12}(Y-Y_{OA}) + a_{13}(Z-Z_{OA})}{a_{31}(X-X_{OA}) + a_{32}(Y-Y_{OA}) + a_{33}(Z-Z_{OA})} \right) + x_{app}, \quad (2.1)$$

$$y_a = f_a \left(\frac{a_{21}(X-X_{OA}) + a_{22}(Y-Y_{OA}) + a_{23}(Z-Z_{OA})}{a_{31}(X-X_{OA}) + a_{32}(Y-Y_{OA}) + a_{33}(Z-Z_{OA})} \right) + y_{app}. \quad (2.2)$$

Similarly the relation between the world coordinates of an object point and its image coordinates in camera B image can be arrived at. They are given below.

$$x_b = f_b \left(\frac{b_{11}(X-X_{OB}) + b_{12}(Y-Y_{OB}) + b_{13}(Z-Z_{OB})}{b_{31}(X-X_{OB}) + b_{32}(Y-Y_{OB}) + b_{33}(Z-Z_{OB})} \right) + x_{b_{pp}}, \quad (2.3)$$

$$y_b = f_b \left(\frac{b_{21}(X-X_{OB}) + b_{22}(Y-Y_{OB}) + b_{23}(Z-Z_{OB})}{b_{31}(X-X_{OB}) + b_{32}(Y-Y_{OB}) + b_{33}(Z-Z_{OB})} \right) + y_{b_{pp}}. \quad (2.4)$$

BIOGRAPHICAL SKETCH OF THE AUTHOR

Name: P. Veera Rajendran

Date of Birth: 15 Sept. 1966

Parents: Mr. R. S. Palanivelu and Mrs. Kalaivani Palanivelu

Primary and Secondary Education: P. R. G. Higher Secondary School, Kattumannar Koil, Tamilnadu State, INDIA, 1971-1983.

College Education: Coimbatore Institute of Technology, Coimbatore, INDIA, 1983-1987.

Degree Earned: Bachelor of Engineering (Mechanical Engineering).

Work Experience: Engineer, Madras Refineries Limited, 1988-1992. Worked in Maintenance of Fractionating Columns, Pressure vessels, Furnaces etc. Worked in Project Engineering Division. Did technical evaluation for pumps, and other machineries. Involved in design of Piping, Columns, etc.

Career Objectives: The author wishes to pursue a career in research and teaching at the University level.

Permanent Address: 5L9, Periyar nagar, Kattumannar Koil, South Arcot District, Tamilnadu State, INDIA, 608301.